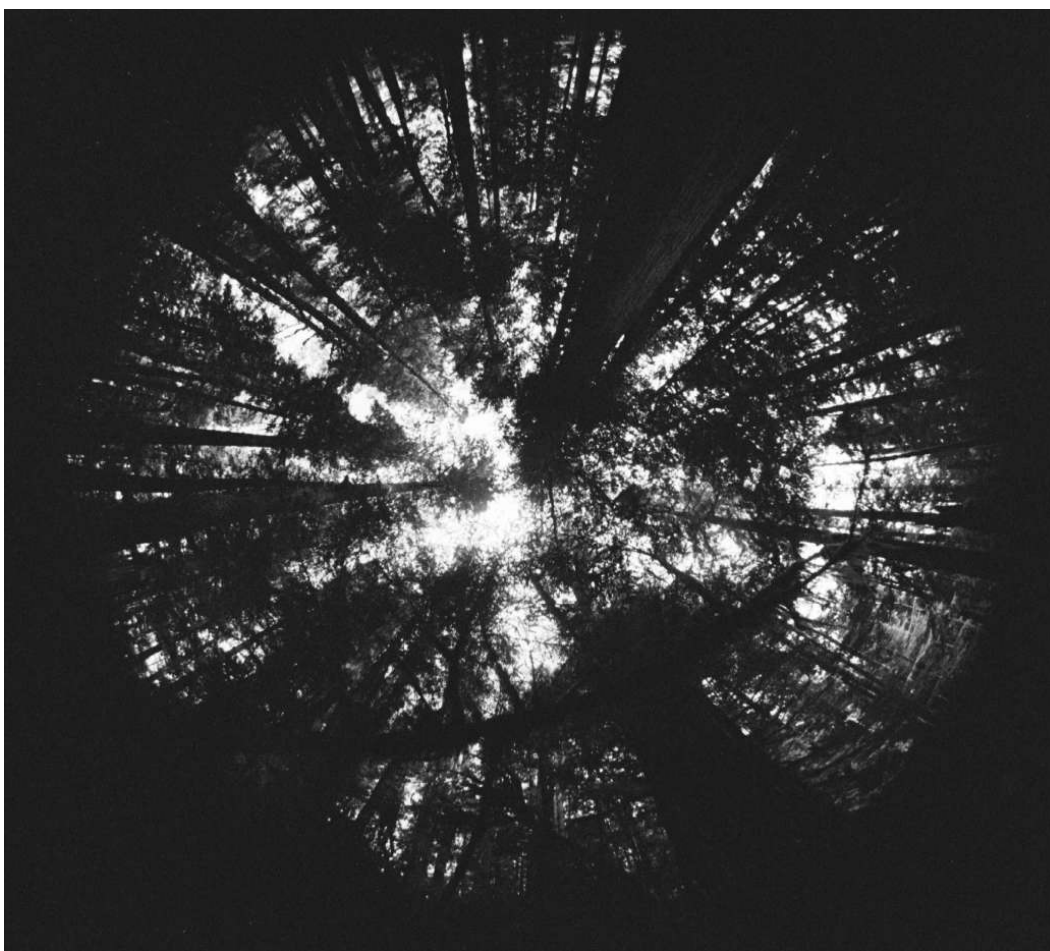




Canadian Forest Service
Forest Ecosystem Processes Network

A method for estimating canopy openness, effective leaf area index, and photosynthetically active photon flux density using hemispherical photography and computerized image analysis techniques



G.W. Frazer, J.A. Trofymow, and K.P. Lertzman

**Information Report BC-X-373
Pacific Forestry Centre, Victoria, B.C.**



Natural Resources
Canada

Canadian Forest
Service

Ressources naturelles
Canada

Service canadien
des forêts

Canada



The Pacific Forestry Centre, Victoria, British Columbia

The Pacific Forestry Centre of the Canadian Forest Service undertakes research as part of a national network system responding to the needs of various forest resource managers. The results of this research are distributed in the form of scientific and technical reports and other publications.

Additional information on Natural Resources Canada, the Canadian Forest Service and the Pacific Forestry Centre research and publications is also available on the World Wide Web at <http://www.pfc.cfs.nrcan.gc.ca/>.

Forest Ecosystem Processes Network

Recent developments and advances by the forest sector in Canada have identified considerable shortfalls in the ecological knowledge base needed for sustainable forest management. This is not surprising when one considers the vastness and diversity of our forests and the complexity of forest ecosystems. However, the ability to forecast the outcomes of management decisions and natural disturbances on the composition and productivity of natural ecosystems is essential.

The Canadian Forest Service (CFS) Forest Ecosystem Process Network (FEPN) will use CFS research centres in Sault Ste. Marie, Ontario and Sainte-Foy, Quebec as lead centres, and will draw upon the talent and expertise of CFS scientists across the country. The network, in collaboration with industry, provinces, and universities, will conduct and coordinate a program of ecological research within forest ecozones of Canada. This program will focus on developing criteria and measurements for sustainable resource utilization and increase our ability to forecast how natural and man-made disturbances will shape the future forest landscape of Canada.

**A method for estimating canopy openness,
effective leaf area index, and photosynthetically
active photon flux density using hemispherical
photography and computerized image
analysis techniques**

G. W. Frazer¹, J. A. Trofymow², and K. P. Lertzman³

¹Research Associate, School of Resource and Environmental Management, Simon Fraser University

²Research Scientist, Canadian Forest Service, Pacific Forestry Centre

³Associate Professor, School of Resource and Environmental Management, Simon Fraser University

Natural Resources Canada
Canadian Forest Service
Forest Ecosystem Processes Network

Pacific Forestry Centre
Information Report BC-X-373

1997

Canadian Forestry Service
Pacific Forestry Centre
506 West Burnside Road
Victoria, British Columbia
V8Z 1M5

Phone (250) 363-0600

Her Majesty the Queen in Right of Canada, 1997

ISBN 0-662-26095-3
Cat. No. Fo46-17/373E

Printed in Canada

An Acrobat version of this report can be downloaded from the Pacific Forestry Centre
World Wide Web site at: <http://www.pfc.cfs.nrcan.gc.ca/>.

Canadian Cataloguing in Publication Data

Frazer, G.W.

A method for estimating canopy cover, vegetation area index, and photosynthetically-active
photon flux density using hemispherical photography and computerized image analysis
techniques

(Information report ; ISSN 0830-0453 ; BC-X-373)

Includes an abstract in French.

Includes bibliographical references.

ISBN 0-662-26095-3

Cat. no. Fo46-17/373E

1. Forest canopy ecology – British Columbia – Vancouver Island.
2. Forest canopies – British Columbia – Vancouver Island.
3. Imaging systems in forestry – British Columbia – Vancouver Island.
- I. Trofymow, J.A. (John Antonio)
- II. Lertzman, Kenneth P. (Kenneth Peter), 1956- .
- III. Pacific Forestry Centre.
- IV. Series: Information report (Pacific Forestry Centre) ;
BC-X-373.

QII541.5.F6F721997 577.3'09711 C97-980406-X

CONTENTS

ABSTRACT	v
RESUMÉ	vi
ACKNOWLEDGEMENTS	vii
1.0 INTRODUCTION	1
2.0 GENERAL THEORY	1
2.1 The Hemispherical Projection	1
2.2 Measurement of Solar Irradiance and Canopy Light Transmission	3
2.3 Indirect Assessment of Canopy Structure	5
3.0	IMAGE ANALYSIS SOFTWARE 7
3.1 HEMIPHOT	7
3.2 GLI/C	11
3.3 PAMAP GIS and Microsoft Excel Application	13
4.0 PHOTOGRAPHY, SCANNING, IMAGE ENHANCEMENT AND ANALYSIS	15
4.1 Hemispherical Photography	15
4.2 Digitization	16
4.3 Media Alignment and Orientation	16
4.4 Image Enhancement	18
4.5 Hemispherical Image Analysis	18
4.5.1 HEMIPHOT	19
4.5.2 GLI/C	20
5.0 HEMISPHERICAL ANALYSIS OF SOUTHERN VANCOUVER ISLAND CHRONOSEQUENCES: A CASE STUDY	22
5.1 Field Methods	24
5.2 Media Preparation, Scanning, and Image Archive	25
5.3 Hemispherical Image Analysis	27
5.4 A Comparison of Output Results: HEMIPHOT vs. PAMAP GIS	28
5.4.1 Percent open sky	28
5.4.2 Effective leaf area index (L_e)	30
6.0 TECHNICAL SHORTCOMINGS AND RECOMMENDATIONS	31
6.1 Digital Image Enhancement and Photography	32
6.2 Projection Distortions and Image Registration	32
6.3 Software Design and Implementation	33
6.4 Standardization of Theoretical Models	34
6.5 Post-processing Corrections for Climatic and Landscape-level Influences	34
7.0	REFERENCES
35	

APPENDICES

A. Catalogue of Representative Hemispherical Photographs Collected at Eight Chronosequences on Southern Vancouver Island	41
B. Measurement of Fisheye Lens Distortion and the Effect on the Calculation of Gap Fraction Magnitude and Distribution, Percent Open Sky, and L_e	45
C. A Model for Estimating Percent Open Sky and L_e Using PAMAP GIS, Microsoft Excel, and a Modified LI-COR Inc. Algorithm.....	55
D. Sample Design of Photo Archive Database for Southern Vancouver Island Chronosequence Study	61
E. Site Characteristics Database for Southern Vancouver Island Chronosequence Study	63
F. HEMIPHOT and PAMAP GIS Percent Open Sky, L_e , and PPFD Data for Southern Vancouver Island Chronosequence Study.....	65

ABSTRACT

Indirect optical techniques have been used increasingly in place of more laborious and often-destructive direct methods to derive stand-level estimates of gap fraction distribution, canopy openness, and effective leaf area index. Hemispherical canopy photography, combined with digital image analysis, is one indirect technique that has proven to be a fast and efficient way to measure various attributes of canopy structure and to predict seasonal patterns of forest canopy light transmission.

The Canadian Forestry Service, Pacific Forestry Centre, utilized hemispherical photography and paired LAI-2000 Plant Canopy Analyzers to measure gap fraction distribution, canopy openness, effective leaf area index, and seasonally-integrated understory light levels in several age sequences of Coastal Western Hemlock and Douglas-fir forests on southern Vancouver Island, British Columbia, Canada. The main purpose of the research was to document some of the structural changes caused by the conversion of old-growth temperate forests to second growth. This report describes the general theory, practical application, and technical shortcomings associated with the hemispherical photography and image-processing component of this project. The field and analytical methodologies used in this research are presented as a case study for those interested in similar ecological applications.

Current hemispherical image analysis systems have not kept pace with evolving digital technologies, computer hardware and software, or scientific models. A number of improvements must therefore be made to realize the full potential of this technique. Hemispherical models do not take into account the effects of local weather conditions, nor do they compensate for the effects of regional landform geometry and site orientation on the distribution of direct and diffuse solar radiation. Post-processing techniques that would correct for some of these deficiencies are possible, but only if intermediate summary data are made accessible to the end-user.

RESUMÉ

Des techniques d'optique indirectes remplacent de plus en plus des méthodes directes plus lourdes et souvent plus destructrices pour obtenir des estimations au niveau du peuplement de la répartition des trouées, du degré d'ouverture du couvert et de l'indice de superficie foliaire effective. La photographie hémisphérique du couvert associée à l'analyse d'images numériques est une technique indirecte qui s'est révélée un moyen rapide et efficace de mesure des différents attributs de la structure du couvert et de prévision des profils saisonniers de la quantité de lumière qui traverse le couvert forestier.

Le Centre forestier du Pacifique du Service canadien des forêts a utilisé la photographie hémisphérique et des appareils d'analyse du couvert végétal LAI-2000 couplés pour mesurer la répartition des trouées, le degré d'ouverture du couvert, l'indice de superficie foliaire effective, et la quantité de lumière dans le sous-étage intégrée en fonction des saisons dans plusieurs séquences d'âge des forêts côtières de pruches de l'ouest et de douglas taxifoliés dans le sud de l'île de Vancouver, en Colombie-Britannique (Canada). Les recherches visaient principalement à documenter certaines modifications structurales causées par la conversion de vieilles forêts tempérées en forêts de seconde venue. Le présent rapport décrit la théorie générale, les applications pratiques et les lacunes techniques de la photographie hémisphérique et du traitement des images de ce projet. Les méthodes pratiques et analytiques utilisées dans le cadre de ces travaux de recherche sont présentées sous forme d'étude de cas à l'intention des personnes intéressées par des applications écologiques du même genre.

Les systèmes actuels d'analyse hémisphérique des images n'ont pas suivi l'évolution des nouvelles techniques numériques, des ordinateurs et des logiciels, ou des modèles scientifiques. Il faut apporter un certain nombre d'améliorations pour tirer le maximum de cette technique. Les modèles hémisphériques ne prennent pas en compte les effets des conditions météorologiques locales, ni ne compensent les effets de la géométrie du relief de la région et l'orientation du site sur la répartition du rayonnement solaire direct et diffus. Il est possible d'appliquer des techniques après le traitement qui combleraient certaines de ces lacunes, mais seulement si l'utilisateur dispose de données sommaires intermédiaires.

ACKNOWLEDGEMENTS

The cooperation and assistance of the Greater Victoria Water District, MacMillan Bloedel and TimberWest in providing site access is acknowledged. Assistance with field sampling was provided by B. Rowsell and analysis of the LAI-2000 data by R. Leach. We would also like to thank H. Barclay, Canadian Forestry Service, C. Canham, Institute of Ecosystem Studies, New York, and D. Coates, B.C. Ministry of Forests, Prince Rupert District, for invaluable review comments. This work was supported (in part) by the Federal Panel on Energy R&D (PERD) through the ENFOR (ENergy From the FORest) program of Canadian Forest Service, Project P-404 and P-453, Canadian Forest Service Ecosystem Processes Network and by the B.C./Canada Forest Resources Development Agreement II (FRDA II) Integrated Resource Management Program, Projects FC-IRM10 and FC-IRM25. Funding for the structural attribute studies was through Forest Renewal B.C. award no. HQ96247 to J. A. Trofymow and K. P. Lertzman.

1.0 INTRODUCTION

Solar energy in the form of photosynthetically active radiation (PAR) is an extremely important component of the forest microclimate that directly influences plant growth and regeneration. The amount and quality of incident light within and under forest canopies is largely determined by the organization, geometry, and distribution of overstory stems, branches, and leaves. A variety of indirect and direct methods have been used to measure various components of canopy structure and solar radiation flux within and below forest canopies (Norman and Campbell 1989; Black *et al.* 1991; Chason *et al.* 1991; Gower and Norman 1991; Welles and Norman 1991; Chen *et al.* 1993; Smith 1993; Fassnacht *et al.* 1994; Welles and Cohen 1996).

Hemispherical canopy photography is one indirect method that utilizes a 180° fisheye camera lens and 35-mm film to capture and record the position, size, and shape of openings or “gaps” in a forest canopy. Pictures are typically taken from the ground looking up, but have also been used in combination with infrared film to photograph down from the top of the canopy (Rich 1990). A hemispherical photograph acts as a permanent record, and is therefore a valuable source of canopy gap position, size, density, and distribution information. These surrogate data are important parameters for indirect measurement of understory PAR and selected attributes of canopy structure such as canopy openness and leaf area index (LAI). With the advent of affordable digital technologies (e.g., film scanners, cameras, etc.), software support for standard graphic image formats, and more powerful desktop computing, digital image analysis techniques have been used increasingly to examine hemispherical canopy photographs (Chazdon and Field 1987; Rich 1988, 1989; Becker *et al.* 1989; ter Steege 1993; Canham 1995).

During the late summer of 1995, eight chronosequence sites located on southern Vancouver Island, British Columbia, were intensively sampled using hemispherical methods. This document describes the general theory, approach, and analytical tools associated with hemispherical canopy photography and computer-ized image analysis in the context of this research. As a result of this work, a technical protocol has been devised that can be adopted, modified, and hopefully improved upon by others who are interested in using hemispherical techniques for similar research initiatives. A number of recommendations have also been identified that would improve the quality and reliability of future hemispherical image analysis systems.

2.0 GENERAL THEORY

2.1 The Hemispherical Projection

The position of all objects relative to a fixed point on the ground surface can be defined within a hemispherical object region whereby each physical element has a unique location measured by an angular distance in both a vertical and horizontal plane (Figure 1). A fisheye photographic lens has a field of view (FOV) that approaches or equals 180°, and has therefore been widely utilized in photogrammetric applications to project a hemispherical object region onto a two-dimensional, circular image plane. A point (P) located within the hemispherical object region will project to another point (P') on the image plane in a manner predicted by the geometric projection used to define this transformation. Herbert (1987) mentioned four common geometrical projections used by commercially available fisheye lenses: a) polar projection, b) orthographic projection, c) Lambert's equal-area projection (Schmidt-net), and d) stereographic equal-angle projection (Wulff-net).

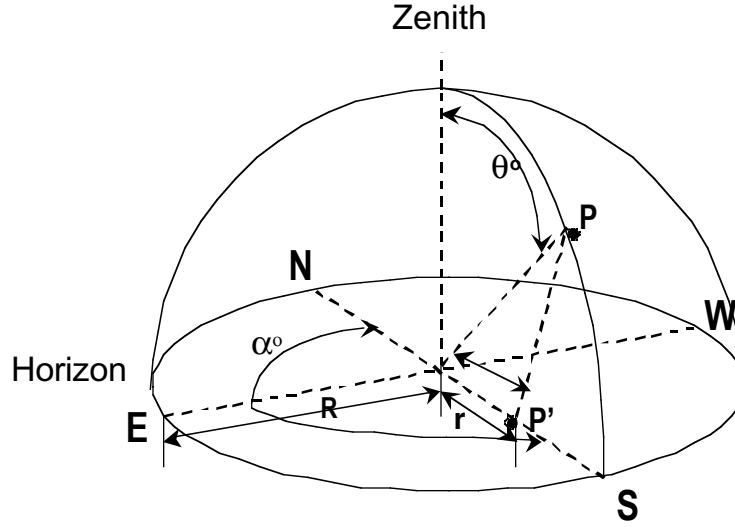


FIGURE 1. Elements in a hemispherical object region can be defined by their angular distance (α , θ) in the horizontal and vertical plane, respectively. An equiangular (polar) projection of the sky hemisphere assumes that zenith angle (θ) is proportional to radial distance (r) on the image plane. Points within the sky hemisphere (P) will be projected (P') onto a circular image according to the geometry of the projection transformation. (Modified from Rich, 1990).

The simplest and most common hemispherical lens geometry is known as an equiangular or polar projection. A polar projection assumes that zenith angle of an object in the sky hemisphere is directly proportional to radial distance in the image plane:

$$\theta/90^\circ = r/R$$

(1.1)

where, θ is the angle between the zenith of the sky hemisphere and the position of the object; r is the distance of the projected point from the image centre; and R is the radius of the circular image (ter Steege 1993). Appendix A shows examples of fisheye photographs taken from beneath a continuous tree canopy looking up from the forest floor. The centre of the photograph indicates the zenith ($\theta = 0^\circ$), and the circular edge represents the focal extent of the horizon ($\theta \cong 90^\circ$).

Accurate measurements of canopy gap size, shape, and distribution, as well as the precise placement of suntracks, depend entirely on first knowing how the image was projected. Herbert (1987) has suggested, in theory, that even small amounts of uncorrected angular distortion might cause substantial error in the measurement of gap area and distribution. This type of analytical error is easily controlled, and is often the result of one or both of the following problems: a) use of an incompatible projection transformation during image analysis, (e.g., correcting an orthographic image using a polar projection transformation), and b) ignoring the deviation of the true lens distortion from the theoretical projection distortions. Figure 2 shows the difference in the radial position of points projected according to a theoretical polar projection and factory calibration tests completed for the Nikkor 8-mm f/2.8 fisheye lens used in this study.

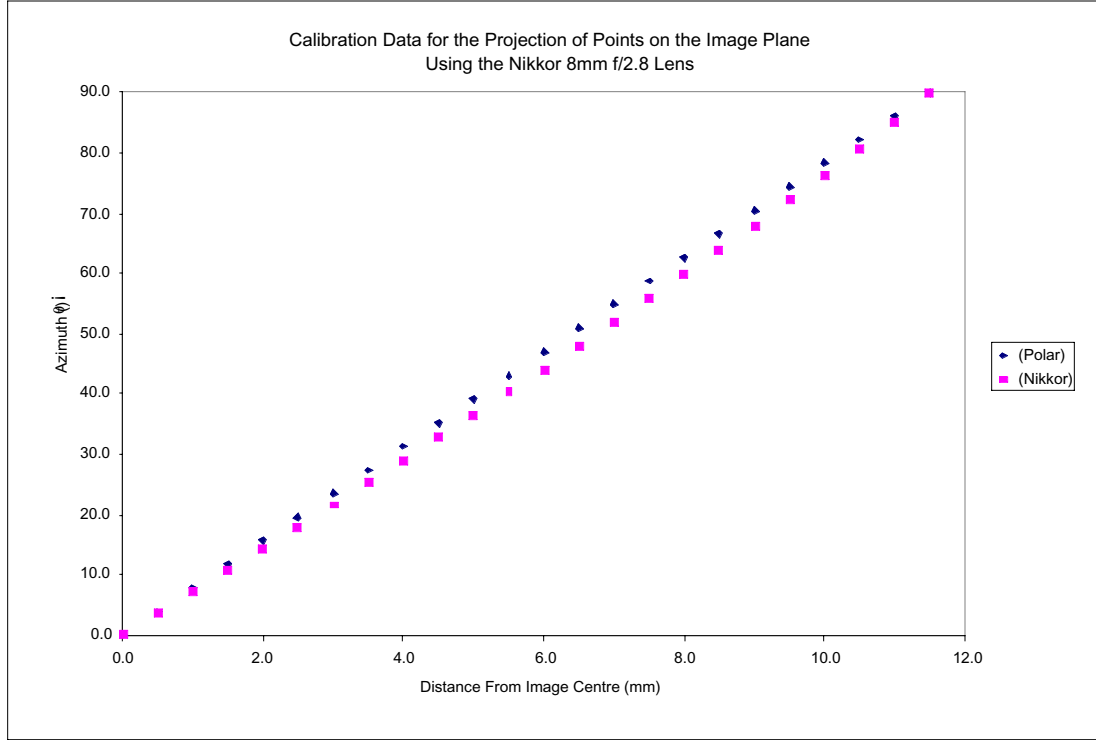


FIGURE 2. Calibration data obtained from the lens manufacturer (Nikon Inc.) indicate that some deviation occurs between a theoretical distribution of projected points and a lens' true measured distortion. Herbert (1987) has indicated that even a small amount of angular distortion may account for substantial error in the magnitude and distribution of gap fractions.

Calibration data for the Nikkor lens were obtained directly from Nikon Inc. and confirmed by direct measurements in Herbert (1987). The mean angular deviation between points projected according to a theoretical polar projection and the Nikkor lens is $1.93^\circ (\pm 1.01^\circ \text{ SD})$. A maximum angular difference of 3.05° occurs at a zenith angle of approximately 55° on the sky hemisphere. Preliminary analyses of selected hemispherical images indicate that even these small angular differences will account for an overestimation of percent open sky by $8.5\% (\pm 1.7\% \text{ SD})$, and therefore underestimate effective leaf area index, on average, by $4.3\% (\pm 1.8\% \text{ SD})$. The effect on estimates of understory global solar irradiation is unknown at this time; however, significant errors in estimates of photosynthetically active radiation (PAR) are also expected. Appendix B presents a correction procedure for hemispherical lenses having a known distortion, and also summarizes the consequence of these angular deviations on gap fraction distribution, percent open sky, and LAI.

2.2 Measurement of Solar Irradiance and Canopy Light Transmission

Electromagnetic energy that has been produced by the sun and is incident on the Earth's outer atmosphere is known as extraterrestrial solar radiation (Gates 1980; Iqbal 1983). The amount of extraterrestrial radiation illuminating an area located just outside the atmosphere and perpendicular to the Sun, and at the mean distance between the Sun and the Earth, is referred to as the solar constant. Approximately 99% of the energy comprising the solar constant is found at wavelengths between 0.25 and $3.8 \mu\text{m}$ (Iqbal 1983). Processes of scattering and absorption selectively attenuate solar radiation entering the Earth's atmosphere. Solar energy that reaches the surface of the Earth unaltered by these processes is known as direct (sunlight) or beam radiation. Attenuated radiation is either scattered back to space, absorbed, or directed towards the Earth (Gates 1980; Iqbal 1983). The attenuated component, which has been redirected towards the Earth's

surface, is known as diffuse (skylight) radiation. Global radiation is the term given to the sum of both direct and diffuse radiation incident on the Earth's surface.

Only a limited portion of the shortwave spectrum reaching the Earth's surface is used in plant photosynthesis (Chazdon and Field 1987). Photosynthetically active wavelengths fall in the visible part of the electromagnetic spectrum, which occurs between wavelengths of 400 and 700 nm (Gates 1980; Pearcy 1989). The term "photosynthetically active radiation" (PAR) was coined by ecologists to describe the spectra of incident light within this energy region. According to Gates (1980), 44% of incident radiation occurring at mid-latitudes is composed of PAR. Chazdon and Field (1987) have used a value of 51% to estimate PAR; however, the availability of PAR is variable and depends strongly on local atmospheric scattering and absorption (Gates 1980; Iqbal 1983). The term "photosynthetically active photon flux density" (PPFD) is used to define the number of photons (400–700 nm) striking a surface of unit area per unit time, and is typically reported in $\text{mol m}^{-2} \text{day}^{-1}$ or $\mu\text{mol m}^{-2} \text{s}^{-1}$ (Percy 1989; ter Steege 1993).

The amount of global PAR incident on the ground beneath a continuous forest canopy is a function of a) the size, shape, and distribution of openings in the overstory, and b) the position and intensity of the Sun in the sky hemisphere. The geometrical relationships between the Earth and Sun are well known and numerically predictable, and a variety of mathematical models to estimate the quantity and quality of incident solar radiation also exist (Hay 1979; Gates 1980; Iqbal 1983; Duffet-Smith 1990). It is therefore possible to calculate the position and potential energy flux of the Sun relative to any point on the Earth's surface over any time interval. Transposing these solar geometry and irradiance data onto the distribution of gap openings recorded in a hemispherical image allow instantaneous or long-term estimates of below-canopy PAR.

A variety of assumptions are inherent in most hemispherical light transmission models: a) canopy gaps allow complete unattenuated transmission of light energy, b) projected foliage surfaces block all incident light, c) the size, shape, and distribution of canopy gaps are static throughout the period of estimation, d) local or regional topography does not affect the distribution of incident global irradiance, and e) the ground albedo is zero and therefore understory light levels are not enriched by the downward transmission of reflected light. It is well known, however, that foliage will transmit and reflect light downwards, that canopies are not static but highly dynamic entities, that ground albedo is rarely zero, and that surrounding topography has a strong influence on light quality and quantity (Iqbal 1983; Flint and Childs 1987; Rich 1990; Chazdon and Pearcy 1991; Welles and Norman 1991; Chen *et al.* 1993; Canham *et al.* 1994). The effects of local atmospheric conditions (e.g., cloud cover, fog, pollution, etc.) on the attenuation and scattering of incoming radiation above the forest canopy are also ignored.

The contribution of diffuse light to the global radiation flux varies considerably and depends primarily on path length, solar angle, and atmospheric conditions (Gates 1980; Iqbal 1983; ter Steege 1993). Canham *et al.* (1994), using long-term empirical shadow-band data for the continental United States, concluded that roughly half of the total growing season radiation flux is composed of diffuse radiation. Empirical global radiation data published for Nanaimo (Departure Bay), British Columbia, were separated into direct and diffuse components by Hay (1979) using a mathematical technique. Results indicate that diffuse radiation accounts for approximately $51\% \pm (13.6\% \text{ SD})$ (minimum 35% in July, maximum 74% in December) of the annual global irradiance at this site (Figure 3). Numerous models of diffuse skylighting have been proposed for use in hemispherical analysis (Anderson 1971; Gates 1980; Iqbal 1983). Two ubiquitous models are the Uniform Overcast Sky (UOC) and the Standard Overcast Sky (SOC). The UOC assumes that diffuse radiation flux is isotropic. In contrast, the SOC estimates that diffuse lighting is three times greater at the sun zenith than at the horizon. The UOC and SOC distributions both ignore the influence of circumsolar radiation and solar angle and as a result are widely acknowledged as being a poor estimate of diffuse radiation flux (Gates 1980; Iqbal 1983; Rich 1990; ter Steege 1993). The hemispherical model is therefore a simplistic one, but is still capable of producing reasonable PPFD estimates, nonetheless (Rich *et al.* 1993; ter Steege 1993; Easter and Spies 1994).

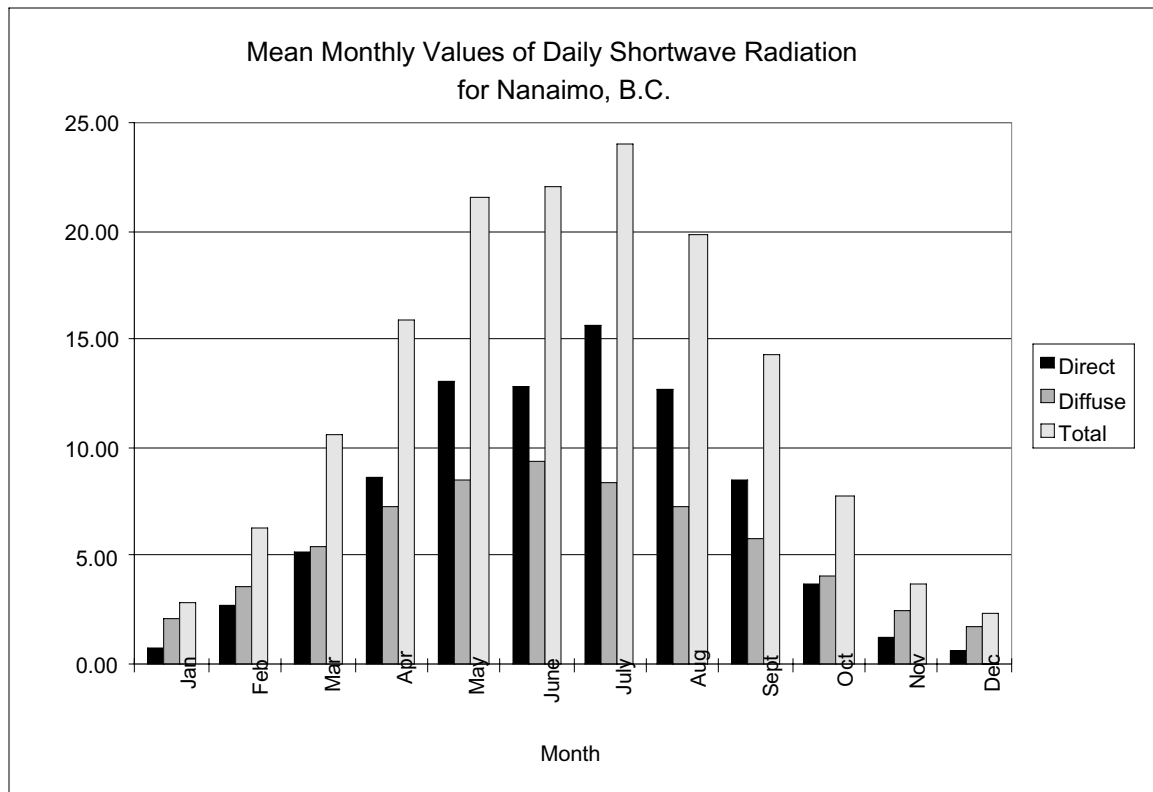


FIGURE 3. Direct and diffuse radiation components extracted from empirically derived global radiation summaries for Nanaimo, B.C. (Data taken from Hay, 1979).

2.3 Indirect Assessment of Canopy Structure

Canopy structure or architecture refers to the quantity, organization, and distribution of stems, branches, and foliage within a forest environment (Norman and Campbell 1989). Numerous measures, such as canopy cover, LAI, gap size and shape, and foliage density, orientation, and tilt angle, have all been used to describe various characteristics of the forest canopy (Norman and Campbell 1989; Welles and Norman 1991). Foliage density, LAI, and foliage orientation and tilt angle can be calculated using mathematical *inversion techniques* presented by Wang and Miller (1987), Perry *et al.* (1988), Norman and Campbell (1989), Chen and Black (1991), Welles and Norman (1991), Chen and Black (1992), Chen and Cihlar (1995) and Chen *et al.* (1997). The theoretical foundation of all indirect structural measures is based on the assumption that the probability of light passing unimpeded through the canopy is proportional to path

length, and foliage type, density, distribution, and orientation. As a result, gap fraction as a function of zenith angle becomes the kernel of these mathematical formulae (Norman and Campbell 1989; Chason *et al.* 1991; Welles and Norman 1991).

Hemispherical photographs provide a permanent record of the size, shape, and spatial distribution of openings in the forest canopy, and have therefore been used successfully as a source of gap fraction data (Neumann *et al.* 1989; Chen *et al.* 1991; ter Steege 1993; Strachan and McCaughey 1996). The relative proportion of open sky contained in any defined region on the projected image plane is known as the gap fraction. These data can be readily calculated and summarized for any interval of azimuth or zenith angle depending on the required application. The true size and shape of the canopy gaps represented on the photographic image have been distorted in a manner predicted by the optics of the lens. In order to estimate structural attributes that rely upon measures of undistorted gap size or shape, objects must first be projected back onto the sky hemisphere. For example, gap fractions must be corrected for area distortion before calculations of canopy openness or cover are made. Percent open sky is defined as the percentage area of the sky hemisphere that is unobstructed by vegetation, and can be calculated as the sum of all area corrected gap fractions multiplied by 100% (ter Steege 1993).

LAI was first defined as the total one-sided area of photosynthetic tissue per unit ground surface area (Watson 1947). Other definitions and interpretations of LAI have subsequently been published and vary depending on the technique used to measure this attribute. Direct sampling of individual trees combined with stand-level allometric methods provide the only dependable techniques to determine LAI as it was originally defined (Marshall and Waring 1986; Norman and Campbell 1989; Smith 1993; Smith *et al.* 1993). Indirect methods that use optical techniques to estimate LAI are based on probability functions that rely on a number of assumptions about the penetration of light through a theoretical canopy. As a result, a variety of terms, definitions, and interpretations are commonly applied to LAI data generated using optical methods. Two contrasting definitions of LAI appear in current research literature: 1) the total one-sided (projected) area of foliage elements per unit of ground surface area (Welles and Norman 1991; Gower and Norman 1991; Deblonde *et al.* 1994), and 2) one half the total leaf area per unit ground surface area (Chen and Black 1992; Fassnacht *et al.* 1994; Stenborg *et al.* 1994; Chen and Cihlar 1995; Chen *et al.* 1997). The differences between these two definitions become significant when applied to canopies composed of non-flat leaves (needles). Chen and Black (1992) and Chen and Cihlar (1995) have demonstrated that the first definition will produce a significant negative bias in LAI estimates obtained indirectly from conifer stands.

Most indirect estimates of LAI are based on the assumptions that canopy elements are randomly distributed spatially, that they do not transmit light, and that individual leaf elements are small relative to the field of view. Given these assumptions, the gap fraction at any angle of zenith may be mathematically related to LAI (Lang and Yueqin 1986; Norman and Campbell 1989; Neumann *et al.* 1989; Chason *et al.* 1991; Chen *et al.* 1991; Welles and Norman 1991; Smith 1992; ter Steege 1993; Fassnacht *et al.* 1994). It is well documented, however, that conifer needles are not randomly distributed but concentrated along individual shoots (Chen and Black 1991; Gower and Norman 1991; Chen and Black 1992; Smith *et al.* 1993; Chen and Cihlar 1995; Chen *et al.* 1997). Models that assume a random distribution of conifer needles will significantly underestimate LAI. Smith *et al.* (1993) have reported LAI underestimates of 62% in mature Douglas-fir stands on southern Vancouver Island, British Columbia, when models that assume a random distribution of foliage elements are used. Chen and Cihlar (1995) and Chen *et al.* (1997) have proposed a new “compacting” technique to remove the effects of non-randomness from clumped canopies.

Current optical methods for estimating LAI do not distinguish between photosynthetic (leafy) tissue and other plant elements such as branches, boles, cones, and other attachments such as lichen and moss. Alternative terms have therefore been proposed such as “vegetation area index” (VAI) (Fassnacht *et al.* 1994; Strachan and McCaughey 1996), “plant area index” (PAI) (Neumann *et al.* 1989; Chen *et al.* 1991; Strachan and McCaughey 1996), and “foliage area index” (FAI) (Welles and Norman 1991). Chen and Black (1992) coined the term “effective LAI” (L_e) to describe LAI estimates derived optically. This

nomenclature seems most appropriate because it recognizes that conventional optical methods and inversion models are a) incapable of measuring the surface area contributed solely by leafy material, and b) unable to compensate for the non-random positioning of canopy elements. Some researchers have derived site- and species-specific measures to correct optical LAI estimates for the negative effects of foliage clumping (Chen and Black 1991; Gower and Norman 1991; Smith *et al.* 1993; Deblonde *et al.* 1994; Fassnacht *et al.* 1994; Chen and Cihlar 1995; Trofymow and Leach 1996; Chen *et al.* 1997). However, few studies have attempted to estimate the contribution of non-photosynthetic surfaces to the total intercepting surface area of a canopy. The definition of LAI used in this report is equivalent to the term “effective LAI” (L_e) proposed by Chen *et al.* (1997).

3.0 IMAGE ANALYSIS SOFTWARE

A number of computer programs have been written to automate the process of calculating understory solar irradiance, canopy openness (or cover), and L_e using digital hemispherical images. All of these programs have been produced in-house by scientific staff, and no commercial versions exist to-date. Examples of such programs are SOLARCALC (Chazdon and Field 1987), CANOPY (Rich 1988, 1989), SYLVA (Becker *et al.* 1989), HEMIPHOT (ter Steege 1993), GLI/C (Canham 1995), and HEMIVIEW (per. comm., Vieglais 1996). HEMIPHOT evolved from SOLARCALC and is a refinement and extension of the original code. All programs have been compiled for the IBM-PC with the exception of SOLARCALC, which is MAC based. HEMIVIEW is currently in beta testing, and will be released as a commercial product sometime in 1997 (per. comm., Vieglais 1996). HEMIPHOT, GLI/C, and a custom image application developed using PAMAP GIS™ and Microsoft Excel have been used in this study to estimate percent open sky, L_e , and understory PAR at several sites on southern Vancouver Island, British Columbia.

3.1 HEMIPHOT

HEMIPHOT is an IBM-PC DOS-based program that was designed to run with a minimum of hardware support (i.e., 80286 processor, 640×400×8-bit (256 colours) graphics) and versions 0, 2 or 5 Zsoft Paintbrush (PCX) image files as input. Image files are limited to 1-bit (2 colours) colour depths at 400 DPI and 8-bit depths at 100 DPI. The calculations performed vary with the resolution and colour depth of the image files used. HEMIPHOT will calculate canopy cover (%), annual, daily, or 24-hour PPFD in relative (%) or absolute ($\mu\text{mol}/\text{m}^2/\text{sec}$ or $\text{mol}/\text{m}^2/\text{day}$) units, L_e , red:farred ratio (R/FR), and gap size. Available calculations are reduced to canopy cover and annual PPFD (in % and $\text{mol}/\text{m}^2/\text{day}$) when 100-DPI, 8-bit gray-scale images are used as input.

HEMIPHOT divides the projected image plane into 89 concentric circles where each circle corresponds to a circular sphere segment on the sky hemisphere having an arc (θ) of 1° (Figure 4). Gap fraction data are calculated for each concentric circle using the ratio of sky pixels to total number of pixels. The sum of all cosine-corrected gap fraction segments is equivalent to the canopy cover. Aggregation of raw gap fraction data into specific intervals of zenith has been related to L_e using various algorithms. HEMIPHOT provides the option for three different estimates of L_e . Raw gap fraction data are also conveniently made available to the user in ASCII format.

Seven suntracks superimposed on the sky hemisphere for equal-interval dates covering a full-year cycle ending with summer solstice (i.e., Julian day 173) are used to calculate absolute and relative, above- and below-canopy PPFD values averaged for the entire year. Direct (DSF), indirect (ISF), and total site factors (TSF) are written to the screen at run-time, but are unavailable when the PPFD data are transferred to an ASCII file. These data are easily calculated as the ratio of below- to above-canopy PPFD once the flat files have been imported into any spreadsheet application. Daily PPFD can also be calculated for each Julian day, and will be automatically written to a filename having the following filename format: *<image file prefix>.YRD*.

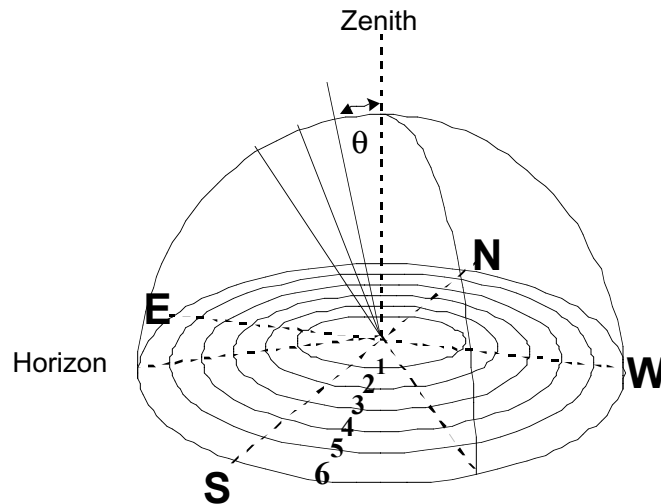


FIGURE 4. The hemispherical photograph can be divided into concentric circles. Each circle will correspond to a proportional degree of arc (θ) projected onto the sky hemisphere. HEMIPHOT divides the image plane into 89 concentric circles that correspond to proportionate 1° arcs on the sky hemisphere.

Figure 5, is an example of mean daily PPFD (*<image file prefix>.YRD*) data plotted using a third-party spreadsheet application. Daily PPFD averages are converted to mean monthly summaries using the subroutine *YEAR2MON.EXE*, included with HEMIPHOT, and written to the filename *<image file prefix>.MON*. Figures 6A and 6B are examples of mean monthly PPFD data plotted for above- and below-canopy locations. Hourly summaries of PPFD over a 24-hour period will also be calculated for the sample date or for Julian day 173. The end-user must define the particular day of interest as well as the filename to which these data will be written.

The theory behind HEMIPHOT is well documented in the supporting manual; however, certain functions and input instructions are unclear and often omitted. The program offers comprehensive hemispherical analysis functions and is extremely robust. It allows access to raw and summarized digital information, and is extremely fast due to the DOS environment. The vector tools, utilized to contain and georeference the hemispherical image, are also reasonably accurate and easy to use. Refer to *HEMIPHOT: a Programme to Analyze Vegetation Indices, Light and Light Quality from Hemispherical Photographs* by ter Steege (1993) for a detailed treatment of the theory.

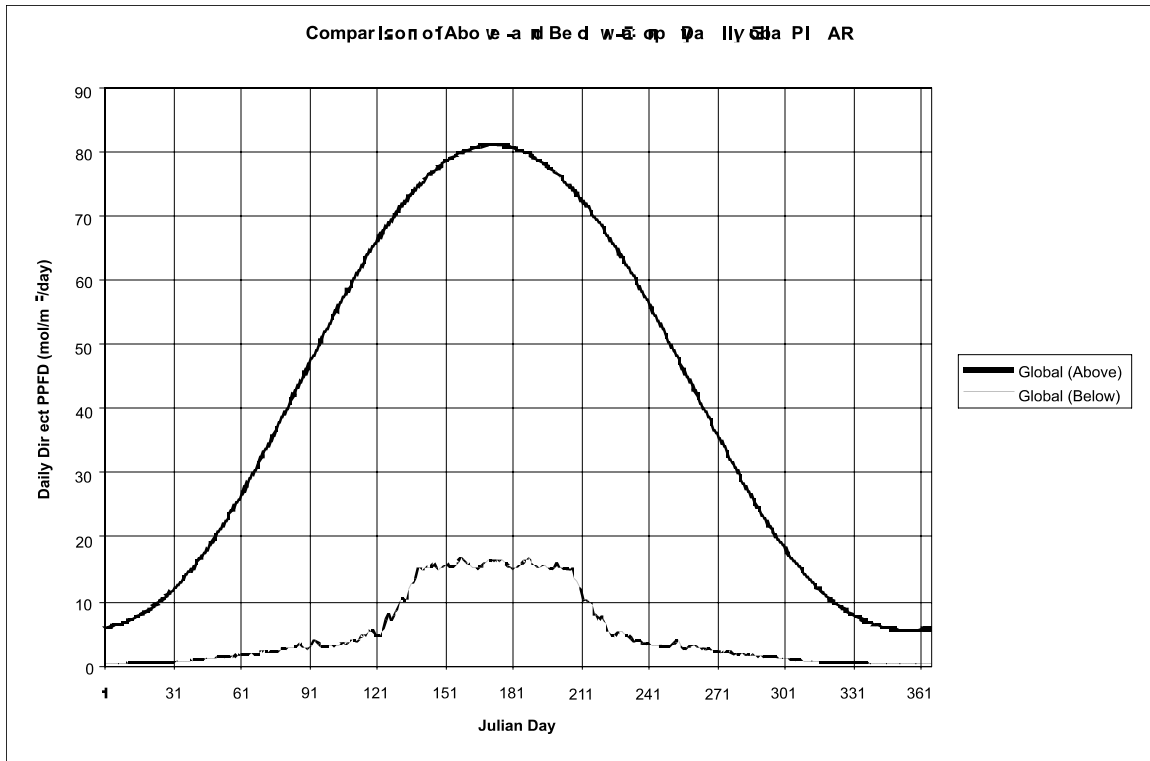


FIGURE 5. Frequency distribution of global radiation incident above and below a continuous forest canopy. These data were imported from a ASCII file produced by HEMIPHOT. Notice that the below-canopy PPFD values are irregular compared to the above-canopy curve. The irregular pattern of the below-canopy readings is a function of the anisotropic distribution of direct light across the sky hemisphere, the randomness of canopy gaps, the eccentricity of the earth's orbit, and the constantly changing solar angle. Notice also the apparent symmetry about Julian day 173 (i.e., summer solstice).

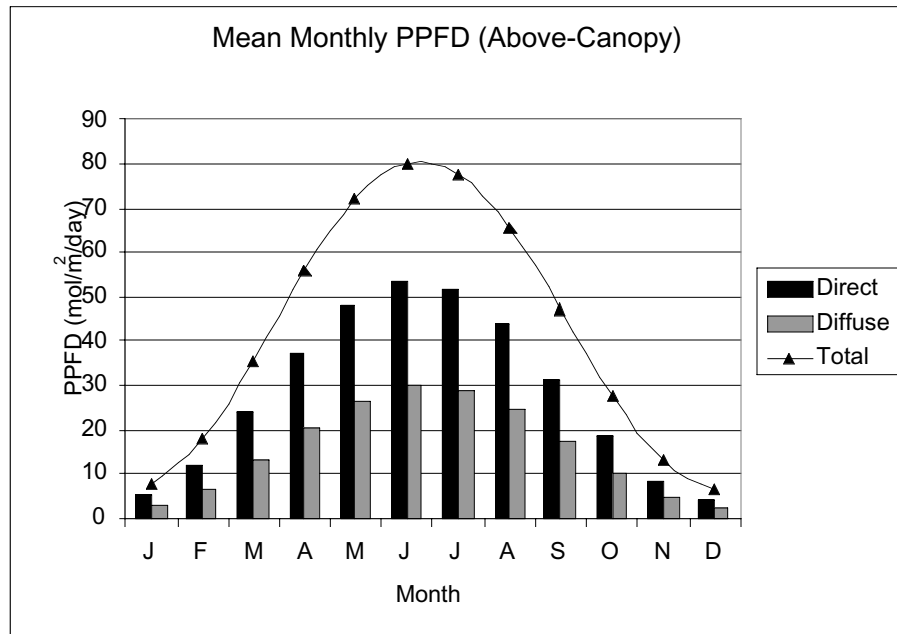


FIGURE 6A. Mean monthly above-canopy PPFD data calculated using the program *YEAR2MON.EXE*. The symmetry of these distributions is a direct consequence of the predicted orbit of the Earth around the Sun and the changing solar angle.

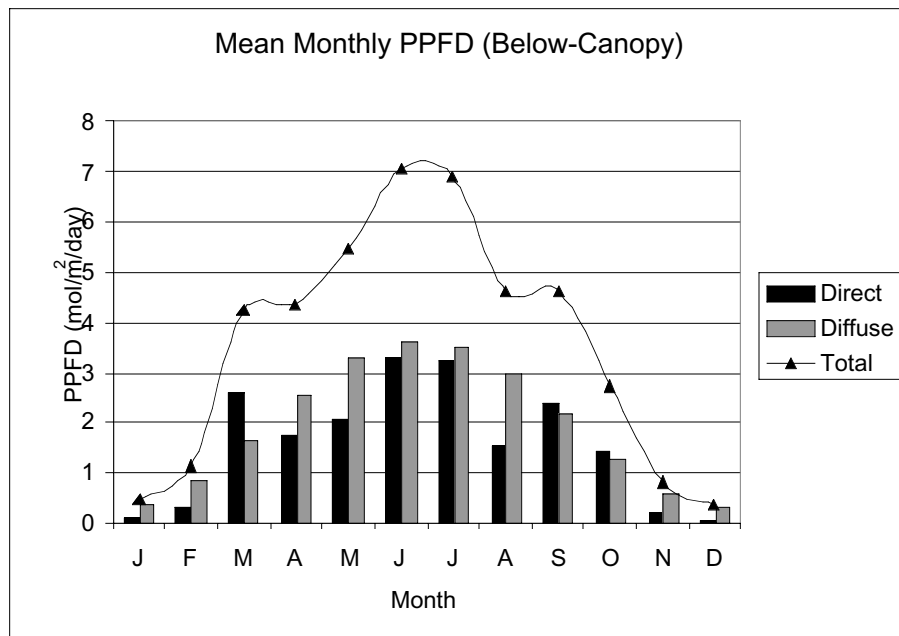


FIGURE 6B. Mean monthly below-canopy PPFD data calculated using *YEAR2MON.EXE*. Notice that unlike the direct and total PPFD data, the diffuse values are symmetrical about JD 173. This is an artifact of the UOC diffuse sky distribution that assumes that all points on the sky hemisphere are equally bright

3.2 GLI/C

GLI/C was written for Microsoft Windows™ 3.1 or higher and requires the following minimum hardware configuration: fast 80486 or preferred Pentium class processor, 8 MB RAM, graphics adapter with 4 MB (VRAM) that can support 24-bit (16.8 million) colour depth display at a screen resolution of 1280×1024. Image files must be in the standard BMP MS-Windows™ raster format; however, no upper limits have been specifically placed on image resolution. Since analysis is done on a pixel-by-pixel basis it is worth remembering that processing time goes up by the square of image resolution. Canham (1995) suggests that 1000-DPI images offer a resolution that will allow sufficient discrimination between sky and foliage without incurring unreasonable processing time. GLI/C will output four parameters including percent open sky, percent beam (i.e., the percent of direct radiation that penetrates through openings in the canopy), percent diffuse (i.e., the percent of diffuse radiation that penetrates directly through gaps in the canopy), and percent global (i.e., combined direct and diffuse total radiation that penetrates directly through all openings in the canopy). These data, as well as gap fraction information organized by azimuth and zenith angle, will be written to an ASCII file (*.DAT) if desired. The radiation model assumes clear sky conditions and therefore produces estimates of potential understory solar irradiance. GLI/C outputs PAR calculations in relative units of measure only.

The support documentation for using GLI/C is found in Canham (1995) and the theory is published in Canham (1988) and in Appendix 1 of Canham *et al.* (1994). According to Canham (*per. comm.*, 1996), gap fraction data are calculated by scanning the image file row by row and assigning pixels inside the sky hemisphere to one of the user-defined azimuth-by-zenith regions or cells (Figure 7). The total number of sky pixels in each cell is then divided by the total number (sky + non-sky) of pixels to derive the gap fraction. Gap fractions are subsequently corrected for the area differences between a circle and a sphere using a cosine transformation and summed for the entire sky region to estimate percent open sky.

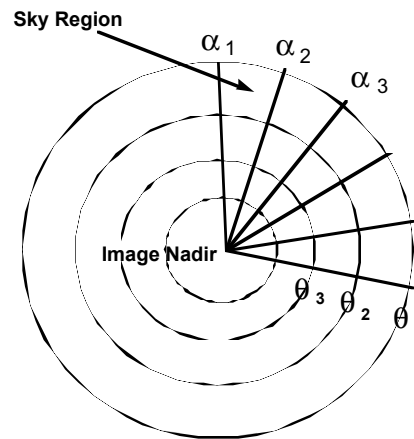


FIGURE 7. GLI/C divides the image file into user-defined regions or cells of azimuth (α) and zenith (θ). The maximum intervals of zenith and azimuth are 24 and 36, respectively.

The distribution of direct, diffuse, and global radiation across the sky hemisphere is derived by calculating the position and intensity of the sun at fixed intervals of time (every 3 minutes) over the course of a day for a specified period (e.g., full year, growing season, *etc.*). The relative intensity of direct radiation on a horizontal surface for any moment in time is calculated as a function of path length and atmospheric clarity (Canham *et al.* 1994). Relative intensities of direct, diffuse, and global solar irradiance are estimated for each region or cell and integrated over the length of the defined season. Relative diffuse radiation flux is measured for any interval of time as a proportion of global radiation flux; i.e., (1-% beam). GLI/C follows the UOC model and assumes that the intensity of diffuse light across the sky hemisphere is isotropic. Prior to run-time, the end-user indirectly specifies the relative weighting of diffuse light as a fraction of total incident radiation. Below-canopy direct, diffuse, and global radiation flux in units of percentage of full sun is estimated by multiplying the gap fraction for each region by the corresponding component of the total mean annual radiation originating from that portion of the sky hemisphere. Summation of these regional data provide gap light estimates for the entire sky hemisphere (Figure 8). The blocky and abrupt patterning of the sky distribution is noticeably unnatural and lacks the smooth transition that should occur between areas of high- and low-intensity lighting. This abstraction is a consequence of averaging radiation intensity on a region-by-region basis.

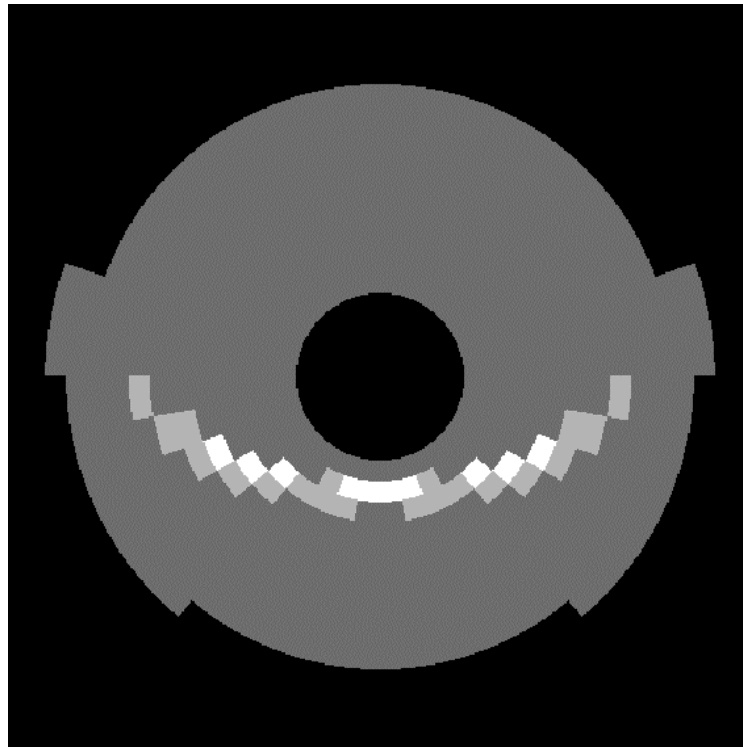


FIGURE 8. GLI/C-derived sky brightness file describing the distribution and relative intensity of global irradiance across the sky hemisphere at a site located on southern Vancouver Island. The top of the image faces north and the left, right, and bottom represent east, west, and south directions, respectively.

The instruction manual that accompanies GLI/C does not include a theoretical discussion of the methods used to calculate gap fractions, percent open sky, or solar radiation flux. This information must be inferred from Canham (1988), Canham *et al.* (1994) and personal communications with the author. GLI/C is very specific about image alignment and will not work properly with hemispherical images that have not been oriented with north at the top (per. comm., Canham 1996). Photographs must be correctly oriented at the time of exposure or a number of difficulties with image registration and pixel assignment could arise. Detailed testing indicated that our image orientations were incompatible with GLI/C. As a result, we chose to abandon use of this software in our particular study. However, a detailed description of GLI/C is given in Section 4.5.2 for those who may be interested in using the software.

3.3 PAMAP GIS and Microsoft Excel Application

A custom application using PAMAP GIS, Microsoft Excel, and Microsoft Visual Basic was written for this study to analyze hemispherical images for gap fraction magnitude and distribution, percent open sky, and L_e . A method to estimate the amount of solar irradiance beneath a forest canopy was not built into this particular application but could be done with additional effort. All the above application software is compiled to run on a PC platform under Microsoft Windows 3.X or higher. PAMAP GIS was used to import, display, and analyze 8-bit (gray scale), 1000-DPI, bitmap-formatted (BMP) images. Specific PAMAP and Visual Basic routines were written to facilitate: a) the import of bitmap images into PAMAP using a converted RAW raster format, and b) conversion of the bitmap colour palette into a PAMAP colour lookup table for purposes of display only. Microsoft Excel was used to a) sort GIS attribute information into an array of gap fraction data organized by azimuth and zenith angles, b) calculate percent open sky, and c) determine L_e using the LI-COR Inc. model modified for use on inclined or horizontal surfaces. A detailed treatment of the PAMAP GIS and the modified LI-COR Inc. L_e methods is given in Appendix C.

PAMAP GIS uses integrated raster and vector data structures to represent spatial information. The hemispherical image was stored as a raster cover and vector arcs and lines were used to partition the image into unique areas of interest defined by angles of zenith (θ) and azimuth (α). The full 90° of zenith angle between the image nadir (0°) and horizon (90°) were divided into 6 equal intervals of 15° arc. The horizontal plane of the projected image was subdivided into 16, 22.5° segments starting at 0° north and rotated through 360° of azimuth (Figure 9). Divisions of the sky hemisphere through the vertical plane follow the geometry of the five rings comprising the LI-COR Inc. LAI-2000 optical sensor (LI-COR Inc., 1992). Gap fraction data were extracted for each unique region using standard PAMAP image statistic functions and then stored in an internal proprietary database. These data were subsequently imported into an Excel spreadsheet application that was used to calculate percent open sky, plot gap fraction and open sky distributions, and estimate L_e using a standard and modified LI-COR Inc. algorithm. In addition to generating gap fraction data, the PAMAP GIS application was also used as a reference to test the reliability of HEMIPHOT and GLI/C for accurate image registration, partitioning, and pixel assignment. Unlike both HEMIPHOT and GLI/C, the PAMAP GIS application allowed constant graphical and numerical checking at each of these critical stages of image analysis.

The modified L_e algorithm developed for this application is based on the mathematical procedures introduced in Welles and Norman (1991) and LI-COR Inc. (1992). The solution presented in both these sources is based on the probable attenuation of diffuse light penetrating a continuous forest canopy of uniform height at a number of defined angles of zenith. The LI-COR Inc. equation relies heavily on the integrity of two major assumptions: a) light depletion will increase with increasing path length through the canopy, and b) path length at a fixed angle of zenith will be the same at any angle of azimuth. The second

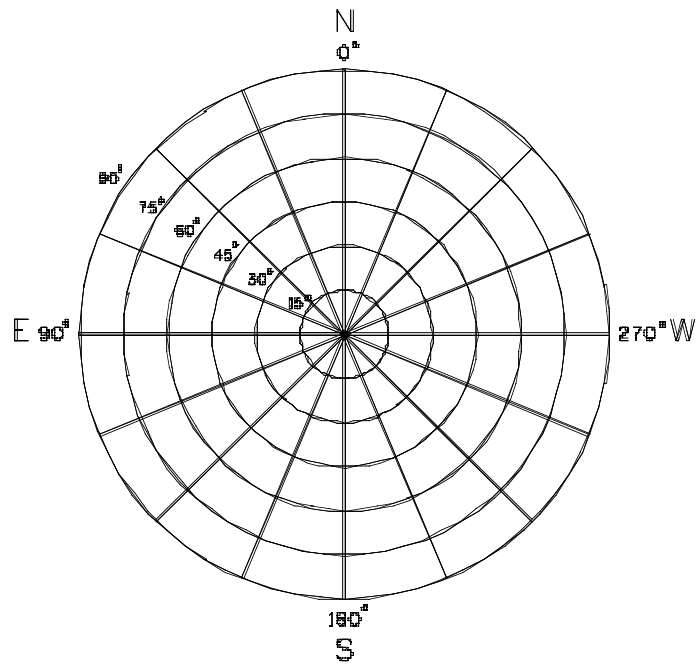


FIGURE 9. PAMAP GIS vector template used to partition hemispherical images into discrete sky regions.

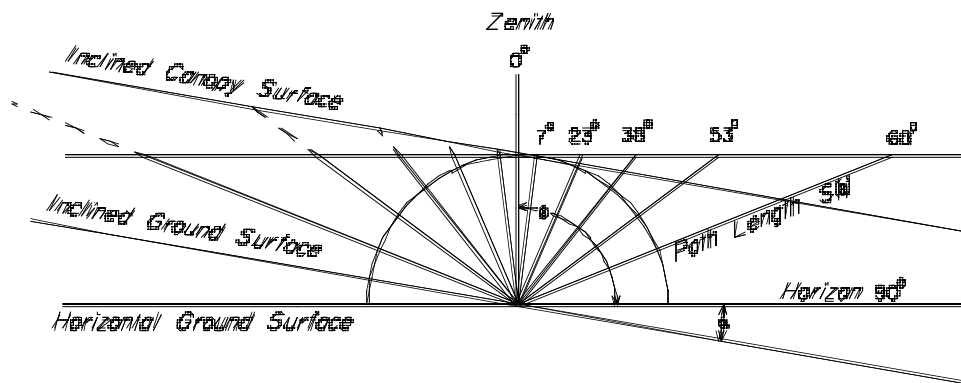


FIGURE 10. Cross-section of a continuous forest canopy of uniform height. On an inclined surface, apparent path lengths through the canopy are shortened in the downslope direction, and lengthened upslope.

assumption is automatically violated on inclined slopes if the hemispherical camera was aligned perpendicular to the local zenith angle. Figure 10 demonstrates the effect of apparent slope on path-length distances through the canopy. In the downslope direction, path lengths are shortened as apparent view angles become smaller. The opposite effect occurs along an upslope bearing where path lengths through the canopy increase as apparent view angles increase. A simple method to correct for these topographic influences on path length involved a modification of the original LI-COR Inc. equation. These modifications were as follows: a) apparent path lengths were estimated for the mid-points of each 22.5° azimuth segment at zenith angles 7, 23, 38, 53, and 68°, b) L_e was determined for each 22.5° segment using the adjusted path lengths, and c) total L_e for a single stand location was calculated by averaging L_e values estimated for each of the 16 sky directions. A detailed procedure is outlined in Appendix C.

4.0 PHOTOGRAPHY, SCANNING, IMAGE ENHANCEMENT AND ANALYSIS

4.1 Hemispherical Photography

Hemispherical photography provides a mechanism for collecting forest canopy geometry and gap distribution information. It is therefore important that these photographs are captured in a form that can be readily used by existing image analysis programs to produce good, reliable results. As mentioned earlier, it is a requirement of most image analysis programs, including HEMIPHOT and GLI/C, that the hemispherical lens is both 180° and equiangular, and that it is of sufficient quality as not to introduce unreasonable distortions. The lens should be tested beforehand to make sure that it conforms to the distortions predicted by a standard polar projection transformation (Herbert 1987). Appendix B can be used as a guide to understanding what lens distortion is, how it can be corrected, and what the implications might be if uncorrected lens distortion is ignored. A similar procedure should be used to investigate image distortions introduced during film scanning.

In the field, the camera body must be mounted on a sturdy tripod equipped with an accurate leveling bubble. The plane of the film must be perfectly horizontal and the camera body must be aligned to true north (not magnetic north). The easiest way to accomplish this is to mark the camera body with an arrow for north and adjust the compass according to the local magnetic declination. Other more reliable techniques using LED markers have been devised, and should be used when possible. Each time the camera is moved it will have to be leveled and realigned with true north. This will allow consistency in picture alignment and orientation between frames and rolls. It is worth noting that the metal camera body will interfere with the ability of the compass to accurately resolve magnetic north, so it is important to stand an appropriate distance away while aligning the camera.

Due to the lower light conditions within the forest canopy it is necessary to shoot with a higher-speed film (e.g., 200–400 ASA). Black-and-white (B&W) film has traditionally been used for below-canopy applications; however, high-speed colour film combined with appropriate lens filtering and digital image enhancement techniques might improve the potential for discriminating between sky and foliage. Kodak Tri-X Pan, Kodak P-Max, and Ilford HP-5 film series are all mentioned as suitable film types (Rich 1990; ter Steege 1993). Numerous bracketed shots should be taken at each sample location just to make sure that a properly exposed picture is collected. The best quality pictures have been taken during uniformly overcast days by underexposing the camera three or four full stops. It is also possible to collect reasonably good pictures on clear days, either early in the morning or later on in the afternoon when the sun is near the horizon. Rich (1990) suggests using a red filter on overcast days and a blue filter on clear days to enhance the contrast between sky and foliage. Film should be exposed at shutter speeds at or greater than 1/125th of a second to make sure any wind-induced movement in the upper canopy is frozen.

It is worth the extra cost to take the exposed film rolls to a custom B&W laboratory for development. Reputable custom labs offer the advantage of higher quality work and usually allow direct access to the technician developing your film. If you are planning to digitize directly from 35-mm film negatives, there is no need to have the negatives printed; however, if you do have a lot of bracketed shots and numerous sample sites, it is worthwhile having contact sheets made. These sheets are invaluable for keeping track of exposures and security in case film strips from different sample sites and rolls become mixed. Contact prints are also very helpful for choosing the proper exposure.

4.2 Digitization

Digitization describes the process of converting film negatives or positives to digital graphic image formats (e.g., BMP, PCX, GIF, JPEG, etc.) for import into image analysis software programs (e.g., HEMIPHOT, GLI/C, etc.). A number of relatively inexpensive IBM-PC and MAC-compatible 35-mm film scanners exist that will digitize colour or B&W film negatives and positives in the form of slides or film strips. Four popular manufacturers and models are Microtek Scanmaker 35T™, Minolta Quickscan 35™, Nikon LS-1000™ and Polaroid Sprintscan 35™. All models with the exception of the Microtek (1828 DPI) will produce scanned image resolutions of a least 2700 DPI.

TWAIN-compliant software applications such as Adobe Photoshop, Paint Shop Pro, Corel Draw, etc., are used to acquire an image directly from the film scanner. Paint Shop Pro for Windows™ 3.X or Windows™ 95 are distributed as shareware and may be downloaded via the internet (URL <http://WWW.JASC.COM/>). Most scanners come with their own software for acquiring and post-processing digital images; however, many of these products are limited in functionality. Adobe Photoshop appears to be an industry standard for graphic image enhancement and is a worthwhile purchase if significant cleanup and modification of the original scanned images are required. Setting up these third-party graphics applications to acquire an image directly from the scanner will save the added steps of exporting an image from the acquisition software and importing into the image enhancement software.

The digitization process is a simple one provided the equipment and support software have been properly installed. The greatest time expenditure will be in choosing the best negative for scanning. Pictures that produce the best results at the analytical stage are a) underexposed 3 or 4 full stops, b) high contrast so that all components of the forest canopy (e.g., foliage, stems, branches, etc.) are completely silhouetted against the backdrop of a light sky, c) exposed under conditions of uniform diffuse skylighting, and d) uniformly underexposed across the entire sky hemisphere. It is always prudent to scan at least two images so that they can be compared side by side, especially during the threshold process. Consistency in defining the optimal exposure is the key to producing high-quality digital images for analysis.

4.3 Media Alignment and Orientation

In order to preserve the orientation of the film negative through the digitization stage, the operator must make sure that the film negative is properly aligned during scanning. The Polaroid SprintScan 35™ will scan both mounted and unmounted (i.e., strips) film negatives. Figure 11A shows the difference between a film slide and strip, and their orientation relative to true north if the camera has been aligned according to the setup in Figure 11B. To preserve correct orientation through digitization, the image must be placed inverted in the scanner with the emulsion side of the negative facing towards the backside of the scanner. This, of course, holds true for the both mounted and unmounted media. Figure 11B indicates how the camera was aligned in the field to produce the geographic orientations of the film negative shown in Figure 11A. Assuming that the north arrow parallels the long axis of the camera body and is directed towards the film advance knob, north, east, west, and south will be always be centred on the left-hand, bottom, top, and right-hand sides of the resultant digital image, respectively.

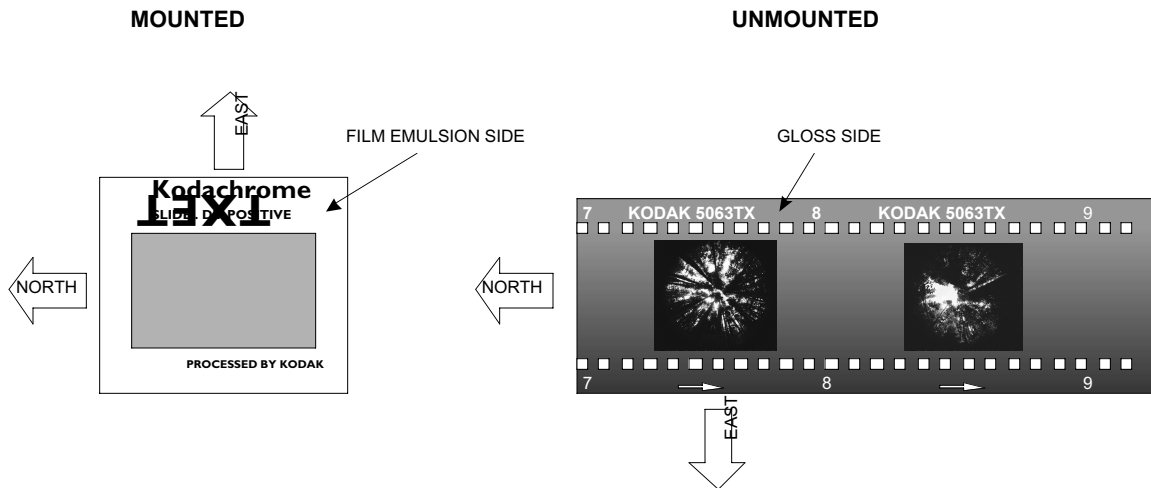


FIGURE 11A. Proper orientation of the slide at scan time is critical for maintaining the alignment through the scanning process. If the body of the camera is positioned as in Fig. 11B, the geographic orientation will be as indicated above. Notice the orientation for both mounted and unmounted developed negatives.

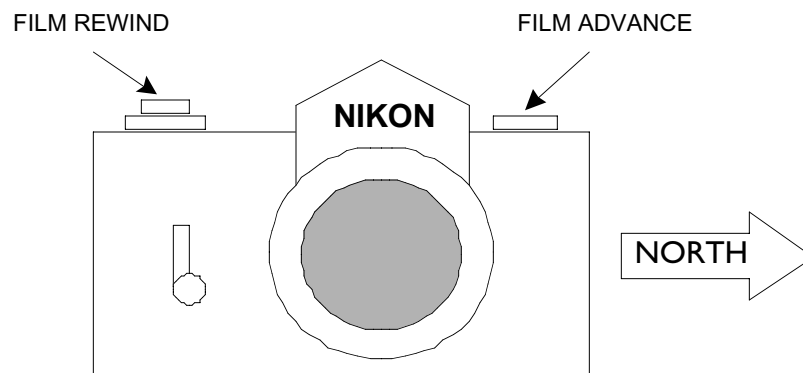


FIGURE 11B. Alignment of the camera in the field defines the orientation of the digital image after scanning. Other methods, which take advantage of LED markers, provide a much more reliable way of recording film orientation.

4.4 Image Enhancement

The contrast quality of a B&W digital image scanned from a photograph is a function of film type, method of development, scan quality, and digital enhancement. Assuming that the film type, exposure settings, and film development laboratory have been correctly chosen, any increased contrast enhancement will occur in the digital world. Colour contrast can be controlled as early as the scanning or digitization stage. In most cases, the scanner will automatically alter colour and contrast according to built-in proprietary rules; however, these settings can be easily modified by an experienced user. The Polaroid SprintScan 35TM has a setting known as *AutoContrast Enhance* that is used to optimize colour balance and boost contrast according to prescribed built-in rules. It is worth spending the extra time understanding the significance of these scanner settings, particularly how they affect image resolution and colour depth, balance, contrast, and quality.

Further digital enhancement is also possible once the initial graphics image has been acquired. Third-party software applications such as Adobe Photoshop incorporate a wealth of tools for manipulating digital image files. These tools include filters for combining neighbouring pixels (i.e., edge smoothing), overlays for blending multiple images, and individualized procedures to adjust the distribution and intensity of pixel spectra. One of the most useful filters for hemispherical applications is that designed for image sharpening. Sharpening filters are typically used to enhance the boundaries between objects that have dissimilar spectral characteristics but are poorly focused. Conditions like these occur in hemispherical photographs, where halos develop around clumps of foliage that are directly backdropped against a light sky. Halos are caused by a scattering of direct beam radiation and produce boundaries that are indistinct. Sharpening filters (e.g., unsharpen mask) may be used to correct this phenomenon, but care should be taken while applying the mask so that canopy gaps are not artificially enlarged.

The exposure quality of a picture taken outdoors is seldom perfect. This is due to the extreme contrast in brightness between areas that are in shadow and those exposed to direct sunlight. The potential for improper exposure is magnified significantly when trying to capture an object that is backlit by the sun. Problems arise in hemispherical image analysis because overexposed (light) objects are considered sky and underexposed (dark) objects are classified as vegetation. Inaccuracies in image classification will lead to substantial errors in the estimation of canopy gap size, and therefore poor estimates of understory radiation flux. It is possible, however, to modify these imperfections using graphical image tools that control the magnitude and frequency of pixel spectra. Adjustments can be made directly to individual or ranges of spectra to control brightness and contrast in regions of under or overexposure. Paint tools equipped with various tips, brushes, and heads can be used to modify flaws that are localized and cannot be improved using techniques that apply global corrections. Third-party image tools offer a wealth of options for image quality enhancement prior to hemispherical analysis. These methods, although relatively time consuming, may provide unlimited potential for a) salvaging poorly exposed photographs that were collected at a great expense and b) improving the quality of gap fraction magnitude and distribution data derived from hemispherical image analysis systems.

4.5 Hemispherical Image Analysis

Hemispherical image analysis describes a set of methods that have been designed to facilitate the indirect measurement of various components of canopy structure, and radiation quality and quantity. Manual methods of analysis have been developed but are considered tedious, time consuming, and outdated (Anderson 1964). Until very recently, most of the computerized image analysis systems were both expensive and proprietary; however, with the development of relatively inexpensive CCD technologies (e.g., film scanners) and software support for non-proprietary graphics formats (e.g., BMP, PCX, GIF, etc.), computer-aided methods are now accessible by most researchers. The following subsections will introduce two distributed hemispherical image analysis programs that can be run on an IBM-PC-

compatible platform running under MS-DOS and MS Windows™ 3.1 or higher. Any technical information regarding the PAMAP GIS and Microsoft Excel application can be found in Appendix C.

4.5.1 HEMIPHOT

HEMIPHOT software requires image-input files that have a PCX format. The software has been compiled for a 80286 processor running under DOS, and, as a result, inherent memory restrictions limit the image resolution and colour depth to the following combinations: 400 DPI at 1 bit (2 colours) and 100 DPI at 8 bits (256 colours). HEMIPHOT automatically converts 8-bit colour images to 4 bits (16 colours), so it probably better to trade off colour depth for resolution from the start of the analysis. The best way to produce 1-bit colour images is to use a threshold function in a third-party image program (e.g., Adobe Photoshop). The threshold function is used to divide the colour display (24, 16, 8, 4 bits) into two colours (1 bit) at a certain intensity value. In hemispherical applications, the threshold value is important and represents the boundary between sky and vegetation. For example, if the specified threshold value is 207 then all image pixels above and below 207 will be considered sky and vegetation, respectively. Once the image has been separated into two colours, all other colour-depth information must be dropped. Colour-depth reductions can be made using the same third-party image program.

Once the image files are in an acceptable graphics format, resolution, and colour depth, these data may be imported into HEMIPHOT for registration and analysis. Image registration is used to a) determine the boundaries of the hemisphere and b) define the orientation of the projected image relative to true north. Registration is a critical stage of analysis because it defines both the proportionate area (in number of pixels) of the hemisphere and the coincident position of the suntrack across the sky. HEMIPHOT uses vector-drawing tools to define the extent of the hemisphere and establish the position of magnetic or true north. In order to use these tools correctly, however, the image must be modified prior to import by marking the positions of true north and the extent of the hemisphere. Small white (value 255) ticks or dots should be placed on the image before the threshold and colour reduction procedures are initiated. It is important that these markings are made on the outside edge of the circular image so that they are not regarded as canopy openings during analysis.

Figure 12 shows the HEMIPHOT analytical screen with a registered image rendered on the left side of the application window. The vector circle containing the hemisphere is sized and placed by the end-user. The application window will not allow any type of analysis until the image is successfully registered. Once an image is registered, HEMIPHOT will automatically load a configuration file (*HEMIPHOT.CFG*) that contains 15 input parameters. These parameters control program execution and contribute numeric input through the calculation stage. Input parameters are entered at run-time and may be modified or saved anytime the program is activated and the image has been registered. Necessary input includes *latitude*, *longitude*, *time zone*, *altitude*, *sampling date*, *diffuse sky model*, *trans. red*, *trans. farred*, *R/FR*, *diffuse fraction*, *clear sky transmission*, *magnetic declination*, *leaf angle*, and *leaf azimuth*. Detailed descriptions of the required input parameters are summarized in ter Steege (1993).

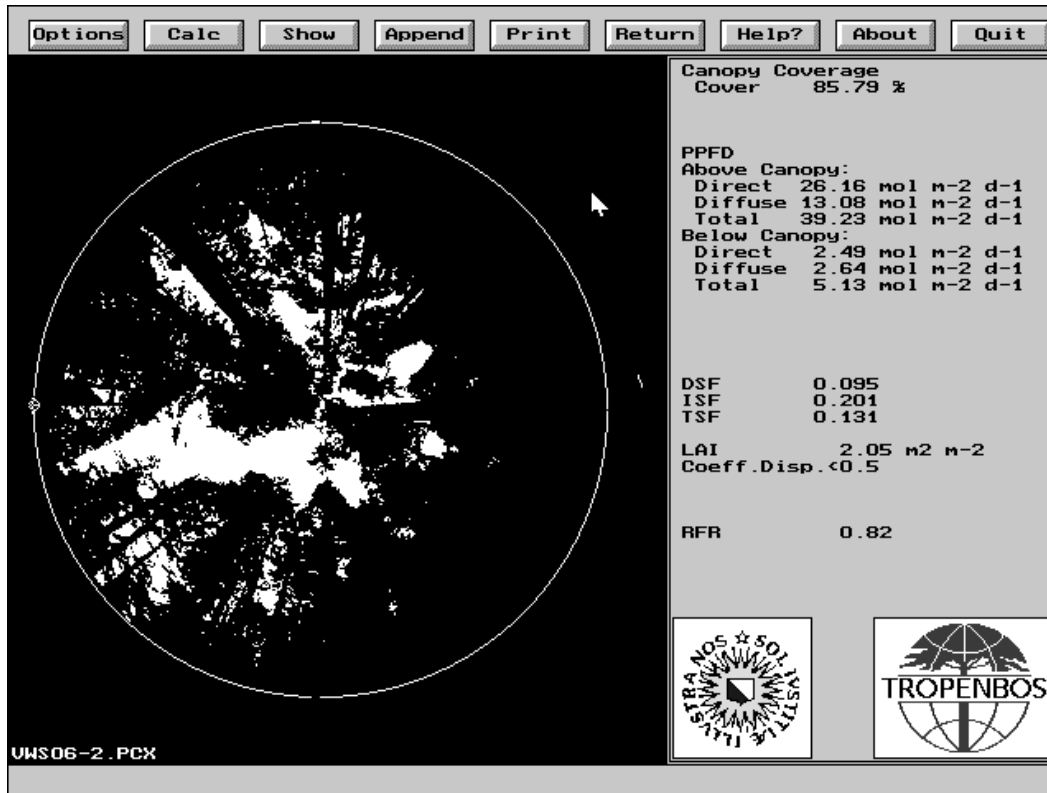


FIGURE 12. The HEMIPHOT analytical screen writes run-time calculations to the right-hand side of the screen while maintaining a rendered image on the left. Notice the vector circle outlining the hemisphere and the north marker centred on its left-hand side.

HEMIPHOT offers a variety of options for analysis and so not all input parameters are required for the software to run. For example, unless you are calculating radiation quality information, (i.e., R/FR ratio), or mean leaf tilt angle, it is unnecessary to specify *trans. red*, *trans. farred*, *R/FR*, or *leaf angle* and *azimuth* input parameters. HEMIPHOT is extremely flexible and allows the end-user to decide which PPFD and L_e models to use, and how the data shall be displayed (i.e., to the screen or file).

4.5.2 GLI/C

GLI/C is a very recent contribution to the limited number of hemispherical imaging applications that currently exist. This program requires a hardware configuration that reflects more of what is considered high-end on the PC platform today. GLI/C runs under MS WindowsTM 3.X and MS WindowsTM 95, and requires substantial CPU and graphics power to run. In order for all information within the application window to be displayed, the monitor and graphics adapter must be able to display at 1280×1024×24 bits at a vertical refresh rate of a least 60 Hz. In addition, GLI/C will process 24-bit (16.8 million colours) images that are in excess of 1000 DPI. Therefore, it is recommended to run the software on a very fast 80486 or Pentium-class machine for best performance. According to Canham (*per. comm.*, 1996), the next release of GLI/C will be written using third-party image tools that will speed up many of the functions and relieve the requirement for such expensive graphics hardware support.

GLI/C will analyze either 24-bit B&W or colour images in BMP format only. The application includes a number of image manipulation tools to view the frequency distribution of spectra in each 8-bit RGB plane, resize the image by cropping, apply a threshold, and alter individual pixel colours using a paint function.

Figure 13 shows the layout of the GLI/C application window. The majority of available functions and output are organized as command buttons in a single view window. Those functions not displayed appear under options shown in the pull-down menu located at the very top. Image rendering is constrained to the bottom half of the window, whereas the top is devoted to the display of textual information (with the exception of the RGB spectral histograms).

To begin an analysis, the program requires input in the form of an image file and numeric parameters. There are 7 distinct input variables: *latitude* (in decimal degrees), *beam fraction*, *clear sky transmission*, *growing season start and end* (in Julian days), *azimuth resolution*, and *altitude resolution*. A detailed description of these variables is given on page two of *GLI/C: Software for Calculation of Light Transmission Through Forest Canopies Using Colour Fisheye Photography*, Canham (1995). These numeric inputs are mathematically combined to produce a sky brightness file that is used for estimating the seasonal contribution of beam, diffuse, and global radiation flux. The sky brightness file (*.SBF) can be saved, modified, and displayed at any time. Analysis cannot take place until a sky brightness file has been loaded.

Images are imported using the *RETRIEVE* button in the application window or the *SCAN* pull-down menu option. If file import is successful, the image will appear centred in the bottom of the application window. The original image must be cropped in order to define the orientation and extent of the sky hemisphere. To do this, click on one of the radio buttons labeled *EAST* or *WEST* and use the mouse to identify the corresponding pixel coordinates. It is very important to note that GLI/C assumes that north is at the top, and the program will produce erroneous gap fraction matrices if this is not the case (per. comm., Canham 1996). When the registration process is complete, press the *CROP* button and the image will be resized and aligned accordingly. The results of the resizing are written to the text boxes framed by the label *Crop Region (X, Y, W, H)*.

A threshold must be applied after the image has been registered and cropped. Assuming that the image is a 24-bit B&W, only a single colour plane needs to have a threshold value applied, since all RGB bands have spectral distributions that are a mirror image of one another. To accomplish this, make sure the *Red* and *Green* check boxes are unchecked and the *Blue* check box is checked. Use the slide bar under the blue spectral histogram to set the threshold value. Press the *THRESHOLD* button to complete the operation. A rendering of the threshold image will be painted to the bottom right-hand corner of the application window. Any touch up to the image can be done using the *BLACK* or *WHITE* radio controls. Calculations of percent open sky and relative beam, diffuse, and global radiation flux are done using the threshold image. Press the *CALCULATE* command button to compute the four values that will be subsequently stored in the text boxes contained by the frame labeled *Output*. These data can be written directly to a user-defined ASCII file using the *STORE* command button. Sample identification or other pertinent information may be added to the text boxes labeled *ID#1*, *ID#2*, and *ID#3* for storage along with the numeric data. Gap fraction data organized into intervals of zenith and azimuth can be saved to a file (<prefix of image file>.DAT), if required.

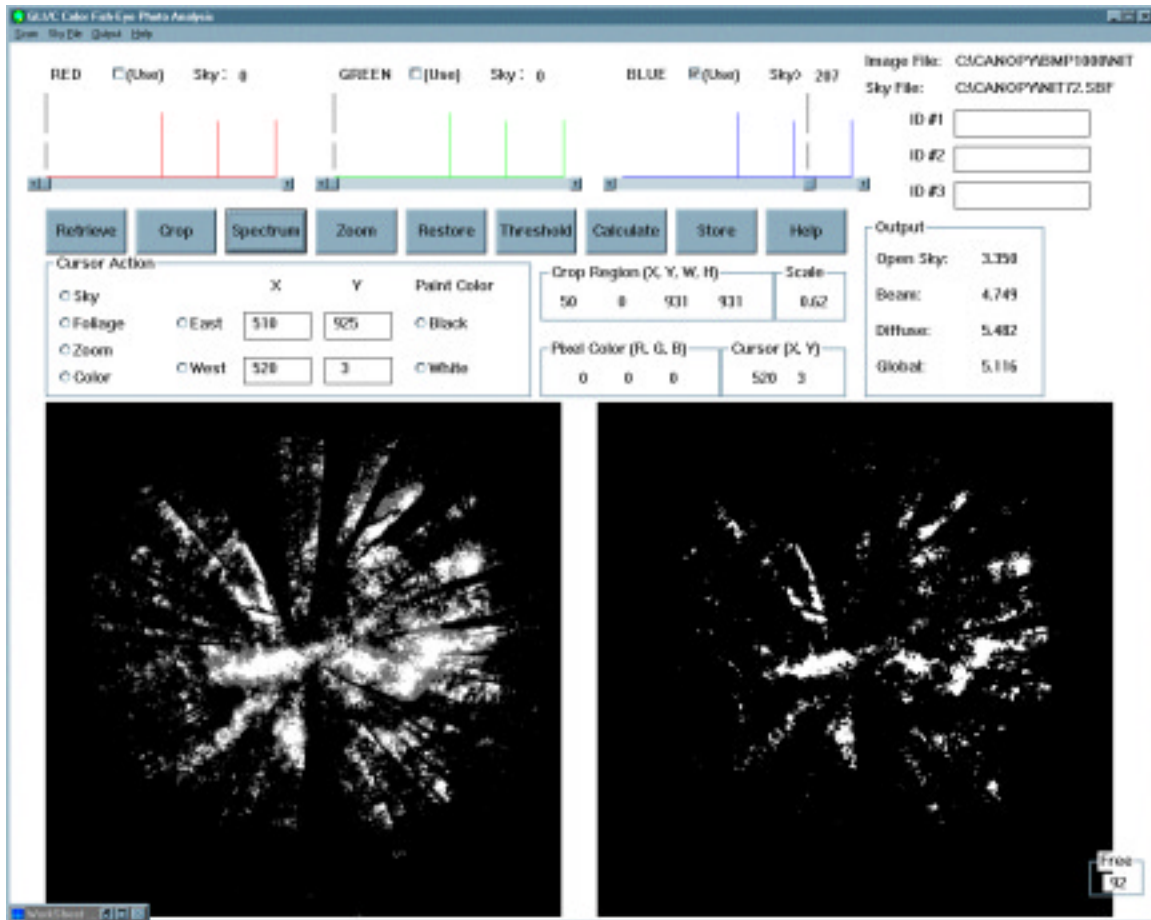


FIGURE 13. The GLI/C application window requires a screen resolution of 1280×1024 for all the information to be displayed. The bottom half is devoted to image rendering and the top to textual and command button display. The left-hand image is a cropped 24-bit original and the image on the right has had a threshold applied (pixel value 207) to the blue RGB plane only.

5.0 HEMISPHERICAL ANALYSIS OF SOUTHERN VANCOUVER ISLAND CHRONOSEQUENCES: A CASE STUDY

A joint research project utilizing indirect methods, (i.e., hemispherical photography and paired light sensors (LI-COR Inc. LAI-2000 Plant Canopy Analyzer)), to measure forest canopy structure and understory light regime was undertaken by the School of Resource and Environmental Management (REM), Simon Fraser University, Burnaby, B.C., and by Natural Resources Canada, Canadian Forestry Service (CFS), Pacific Forestry Centre, Victoria, B.C. The field component of this study took place in August and September of 1995 within eight chronosequences established and monitored by the CFS. All study plots lie within the Coastal Western Hemlock (CWH) biogeoclimatic zone of southern Vancouver Island, British Columbia, between latitudes 48°33' N and 49°03' N. Half of the chronosequences are situated on the west side of the island within the Very Wet Maritime (CWHvm) subzone, while the remaining sites are found in the Very Dry Maritime (CWHxm) subzone on the opposing east side.

(Figure 14). Each chronosequence was composed of three seral stands ranging in age class from immature, mature to old growth (Trofymow *et al.* 1997).

The main objective of this research was to establish an inventory of biophysical data describing the structure and light environments of forest canopies across a wide spectrum of age classes, stand developmental stages, and geographic locations. Analyses of these data will provide further insight into a) the structural changes that occur in forest canopies over time, b) the interrelationships between gap development and canopy (gap) light transmission, and c) the natural variability in the occurrence and geometry of canopy gaps within and between stands of similar or different age and biogeoclimatic class. A project funded by Forest Renewal BC (FRBC) to complete the statistical analyses and interpretation of these data is currently under way.

The hemispherical canopy photography and image analysis methods used in this study will be outlined in the following subsections as a case study for those interested in further application of this technique. The case study will be presented in the context of defining a methodology for field data acquisition, database storage, image processing, and data presentation. The following methodological approach is not definitive and should therefore be read as a guideline or foundation for further development.

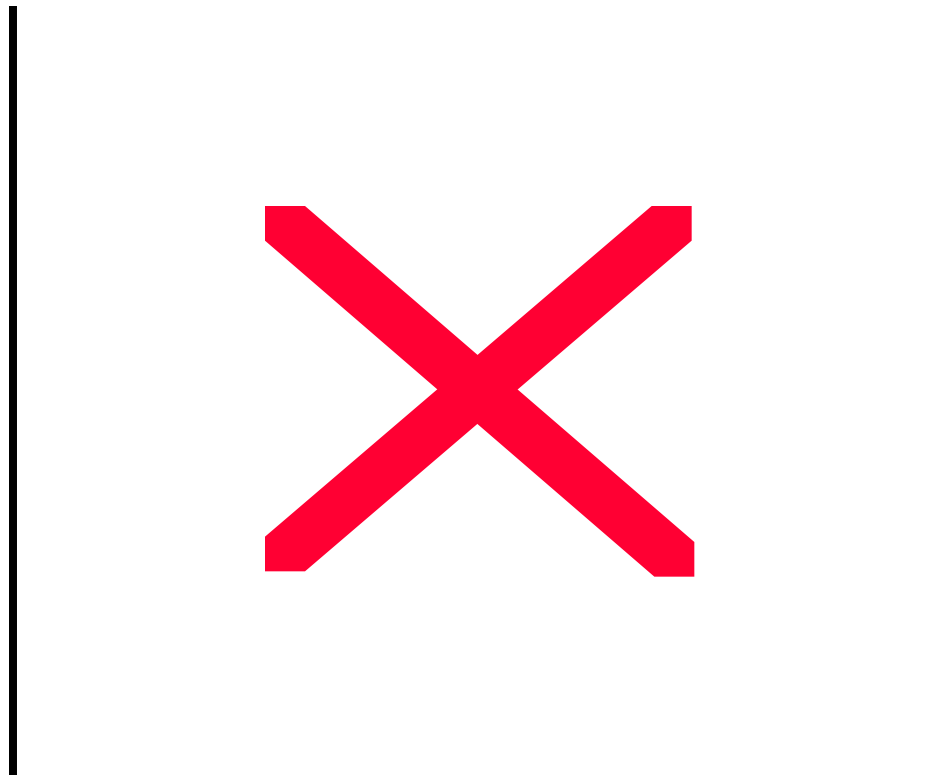


FIGURE 14. The study sites (plots) are all located within the Coastal Western Hemlock (CWH) biogeoclimatic zone of southern Vancouver Island, B.C. Eight chronosequences, each composed of three seral stands (immature, mature, and old growth), were intensively sampled using paired light sensors and hemispherical photography.

5.1 Field Methods

The adopted sampling approach was a hierarchical one. Eight individual chronosequences were each composed of 3 seral stands ranging in age class from immature (20–40 yrs.), mature (65–90 yrs.) to old growth (>200 yrs.). Each of the 24 seres (plots) was sub-sampled 7 times according to a pre-determined sub-plot geometry (Figure 15). The sub-plot geometry was fixed in dimension and positioned relative to true north. All sub-plots were located 30 m from a central point (sub-plot #4) at 60° increments of azimuth. The bearing of the line originating at sub-plot #4 and passing through sub-plot #1 defines the orientation of the plot relative to true north. Eleven of the plots were oriented on 0° and the remainder ranged from 330° to 120°. In total, 167 sub-plots were sampled using hemispherical photography.

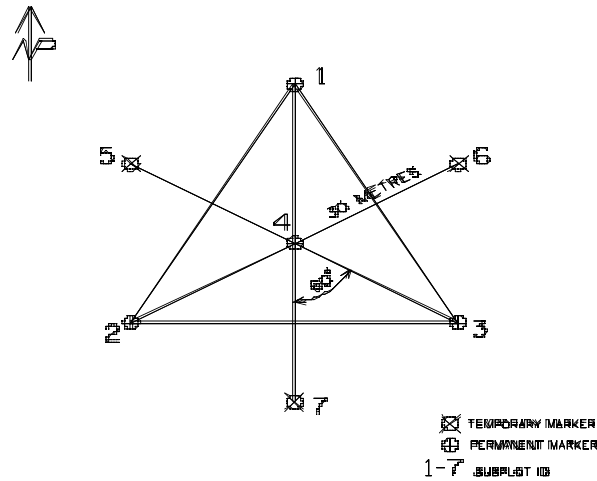


FIGURE 15. Sub-plot sampling configuration for each of the 24 plots. All sampling points were established 30 m and 60° from a central point. The orientation of the plots relative to true north varied from an azimuth of 330° to 120°. Eleven of the plots were oriented at 0°.

The forest canopy was photographed from the forest floor looking up using a 35-mm camera (Nikon F) outfitted with 180° equiangular fisheye lens (Nikkor 8-mm f/2.8, Nikon Inc.) and loaded with B&W Kodak Tri-X Pan 400 ASA film. The camera was mounted on a fully adjustable tripod for easy leveling in the horizontal plane and alignment with true north. A compass corrected for local magnetic declination (20.5° E, 1994) was used to align the camera each time the tripod and camera were moved. The tripod was placed over the centre point of the sub-plot marker unless a distance of off-set was required to avoid interference from large trees and understory plants during film exposure. As a general rule, the camera was positioned at 1.3 m above the ground and a minimum of 2 m away from any tree larger than 30 DBH. Any dangling branches or foliage falling within 1 m of the lens was also pushed aside before exposure. To avoid self-portraits, camera operators must make sure they are below the level of the lens when pictures are taken. All exposures were bracketed using a fixed aperture of f/8 and shutter speeds ranging from 1/1000th to 1/60th of a second.

As always, detailed field notes are an invaluable resource when organizing data for analysis. It is extremely important, therefore, to devise a reliable protocol for data recording, film processing, and archiving before going into the field. This is especially true of hemispherical canopy photography where samples (exposures) cannot be directly tagged with specific information, (e.g., identification, comments, etc.), at the time of collection. In this study, detailed field notes were arranged in a tabular format for each chronosequence, sere, plot, and sub-plot. The following information was recorded: site and sub-plot

identification, sample time and date, roll I.D., frame number, camera settings, weather conditions, and general comments. Since all fisheye pictures are similar in appearance, it is important that the roll identification and frame numbers correspond to the appropriate site and sub-plot locations at the end of the day. To ensure this, all film rolls were physically marked and logged with a unique identifier. The B&W laboratory contracted to develop the film negatives should be made aware of this identifier and its importance. All information was subsequently transferred to a computer database for permanent storage (Appendix D).

5.2 Media Preparation, Scanning, and Image Archive

B&W development laboratories provided services for film negative development and cutting, and for preparation of contact sheets. Contact sheets were used to select exposures for scanning and also as media for hardcopy archive. A light table was also helpful for identifying exposures with optimum contrast for image processing. Most often, pictures underexposed by 3–4 stops beneath diffuse sky conditions were perfect for analysis. In contrast, a hemispherical photograph taken under clear sky conditions with the Sun close to the zenith is rarely uniform in exposure across the entire image and will show imperfections

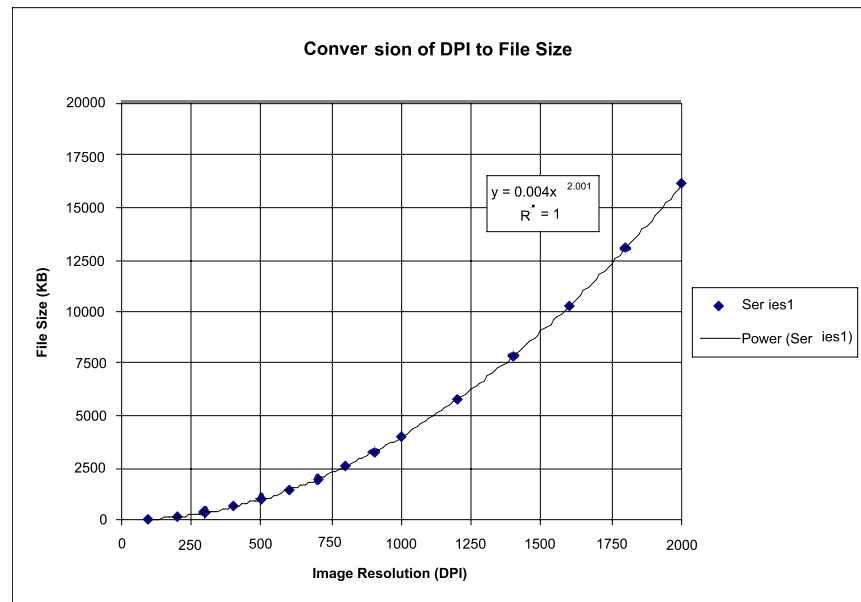


FIGURE 16. The relationship between DPI and file size is important when considering the computer resources required to move, modify, process, and store digital image data. The above relationship holds true only for 35-mm film media (24.2×36.3 mm) scanned at a colour depth of 24 bits. Sixteen- and 8-bit colour depths will reduce file sizes by 1/3 and 2/3, respectively.

such as halos and overexposure on the proximal side of vertically aligned stems. These kinds of imperfections produce digital images that are difficult to classify without overestimating canopy openness and understory light levels. For canopy photographs taken under clear sky conditions, the optimal exposure is one that minimizes overexposure effects without losing too much of the light sky back drop in sensitive areas near the horizon.

Image digitization was accomplished using a Polaroid SprintScan 35TM film scanner connected via a SCSI adapter to an IBM-compatible PC. Images were acquired directly from the scanner using Adobe Photoshop. The scanner was set to *AutoContrast Enhance* mode for automatic optimization of colour (gray scale)

quality and contrast, and colour-cast removal. All 167 images were digitized at a resolution of 1000 DPI in 24-bit true-colour mode and stored on a local hard drive. A 1000-DPI true-colour image will occupy approximately 4017 KB of hard disk space so all images were cropped to 2800 KB at scan time. Figure 16 shows the relationship between DPI resolution and file size. Choosing an appropriate DPI setting is very important when considering a) the time constraints imposed by RAM and CPU overhead for scanning, image enhancement, and analysis, and b) hard disk storage limits. Canham (1995) suggested that image resolutions higher than 1000 DPI require substantially more system overhead using GLI/C without providing a noticeable improvement in data quality. One thousand DPI was therefore used as a maximum image resolution for scanning and processing.

Adobe Photoshop 3.X was used to acquire, crop, resize, threshold, and discard colour information. The GLI/C and HEMIPHOT image analysis software applications require two very different image input formats, resolutions, and colour depths. As a result, the 35-mm negatives were initially scanned in a BMP format at an image resolution of 1000 DPI and 24-bit colour depth, and then archived in a separate directory (e.g., /1000BMP) (Figure 17A). Once the GLI/C image input file was saved, the image resolution

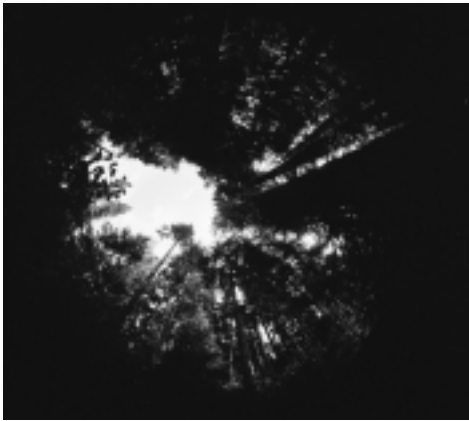


FIGURE 17A. GLI/C image analysis software will import BMP formatted files with image resolutions higher than 1000 DPI at colour depths of 24 bits. File size is 4017 KB (uncropped or 2800 KB (1040×931 pixels) cropped).



FIGURE 17B. HEMIPHOT is limited to image resolutions of 400 DPI (400×358 pixels) or less. The image must have a threshold applied, reduced in colour depth to 1 bit (2 colours) and converted to PCX format. File size is reduced to 6 KB.

was reduced to 400 DPI, the threshold value was set to 207 to distinguish between sky and non-sky, the colour depth was decreased to 1 bit (2 colours), and the file was converted into PCX format and then finally saved to a separate archive directory (e.g., /400PCX) (Figure 17B). None of the images were enhanced using filters, overlays, or individual pixel modification tools; however, these procedures do offer unlimited potential for improved colour (gray scale) contrast.

5.3 Hemispherical Image Analysis

The time required to analyze hemispherical canopy images is quite short compared to the effort spent photographing, developing, scanning, and converting the digital image files into a usable format. The image analysis process is a straightforward one, but requires some understanding of program flow, mandatory input, and output options, nonetheless. HEMIPHOT is substantially more function rich than GLI/C, and thus demands more time and attention. Both *GLI/C: Software for Calculation of Light Transmission Through Forest Canopies Using Colour Fisheye Photography*, Canham (1995) and *HEMIPHOT: A Programme to Analyze Vegetation Indices, Light and Light Quality from Hemispherical Photographs*, ter Steege (1993) should be read in detail before undertaking any analysis.

GLI/C was used to analyze the complete database of image files; however, incompatibilities between image orientation and GLI/C forced abandonment of this program. Those researchers interested in using this software should consult its author before capturing photographs in the field. An alternative application was developed for this study using PAMAP GIS, Microsoft Visual Basic, and Microsoft Excel to import hemispherical images, extract gap fraction magnitude and distribution data, and calculate percent open sky and L_e . The dataset generated from this software application was used as a standard to further test the ability of HEMIPHOT and GLI/C to accurately extract gap fraction magnitude and distribution information. A detailed description of the GIS-based application is outlined in Appendix C. The following paragraphs describe the registration techniques and input data used by HEMIPHOT to process all 167 digital images produced from this study.

HEMIPHOT will only process 1-bit colour images at 400 DPI, so it is essential to mark the east, west, north, and south positions of the hemisphere prior to colour depth reduction and import. Paint tools in Adobe Photoshop were used to accomplish this task. Registering an image in HEMIPHOT is fast and accurate, provided the positional markings were carefully placed. Rotation and registration of images not previously aligned in the field are readily accommodated by HEMIPHOT. Fifteen input parameters are submitted by the user during run-time; however, not all model parameters are mandatory. The input parameters chosen are wholly dependent on the necessary output. For example, input parameters such as *trans. red*, *trans. farred*, and *R:FR* can be left unchanged if understory *R:FR* is not required by the operator. This also holds true for *leaf ang.* and *leaf azim.* input parameters as well. In this study, *HEMIPHOT.CFG* was set to the following input parameters: *latitude*, *longitude*, and *altitude* were derived from data in Appendix E; *time zone* = -8; *number of days* = 7; *day* is derived from Appendix E; *sky type* = UOC; *trans. red* = 0.02; *trans. farred* = 0.25; *R:FR* = 1.1; *diffuse part* = 0.50; *tau* = 0.65; *magn. corr.* = 0; *leaf ang.* = 0, and ; *leaf azim.* = 0.

Values for *trans. red*, *trans. farred*, and *R:FR* were derived from responses solicited by Rachel McGhee (*pers. comm.*, 1995) using an internet USENET server. The actual values were submitted by Robert G. Knox, Biospheric Sciences Branch, Code 923, NASA/Goddard Space Flight Centre (GSFC), Greenbelt, MD 20771 (knox@spruce.gsfc.nasa.gov). The value for the *diffuse part* variable (i.e., 0.50) came from two independent sources: a) long-term shadow band data generated for the continental United States, (Canham 1988, 1995), and b) modeled data published by Hay (1979) for Nanaimo, BC. This term is only valid for PAR integrated over an entire year, since the contribution of diffuse light to total radiation varies according to local climatic conditions and therefore season. A standard clear sky transmission coefficient of 0.65 is used for all but severely polluted atmospheres (Gates 1980; Iqbal 1983).

5.4 A Comparison of Output Results: HEMIPHOT vs. PAMAP GIS

HEMIPHOT was configured to run only a minimum set of analyses that included percent open sky, yearly averages of absolute (in mol/m²/day) and relative (in percent) direct, diffuse, and total PPFD for above- and below-canopy environments, and L_e using the LI-COR Inc. method (Welles and Norman 1991; LI-COR Inc. 1992). The PAMAP GIS and Microsoft Excel application was designed to measure percent open sky and L_e only. Consequently, it was not possible, within the context of this study, to compare the PPFD output produced by HEMIPHOT with independent data measured using another image analysis program. How HEMIPHOT PPFD output would compare with data generated by any other image analysis software would depend upon inherent differences in a) software implementation strategies, (i.e., image registration and pixel assignment techniques), b) the quality and complexity of the solar radiation model, and c) assumptions about canopy light transmission.

The quality of gap fraction magnitude and distribution, percent open sky, and L_e data is directly related to hemispherical image quality and the ability of the software to perform specific spatial measurements with a high degree of accuracy. The PAMAP GIS application utilizes very complex but proven spatial algorithms and techniques to extract gap fraction data from hemispherical images. Also, unlike HEMIPHOT and GLI/C, each analytical step could be checked graphically and numerically for processing errors. The PAMAP GIS application, therefore, provided a reliable basis for comparing the percent open sky and L_e data output from HEMIPHOT. All raw data generated from the HEMIPHOT and PAMAP GIS applications, including selected descriptive statistics (i.e., minima, maxima, means, medians, and standard deviations) are presented in Appendix F.

5.4.1 Percent open sky

Figure 18 is a scattergram indicating the coincidence between measures of percent open sky determined using HEMIPHOT and PAMAP GIS. Linear regression results for this comparison reveal a strong correlation supported by a coefficient of determination (R^2) equal to 0.98 (significant at 95% confidence level) and a slope coefficient slightly less than 1.0. A slope less than unity suggests that HEMIPHOT produces slightly lower estimates of percent open sky than the PAMAP GIS application for the same photograph. A variety of tests were implemented to isolate the source of this disparity, and results indicated that the colour-depth reduction procedure used for one set of photographs and not the other strongly influenced the classification of sky and non-sky pixels. The effect of colour-depth reduction (converting 24-bit images to 8-bit), in this case, was to cause a slight increase in the estimation of open sky. A way to limit this type of error is to make sure the image threshold value is defined after colour reduction and not before. Other tests indicate that the resizing process and differences in image resolution, at least in the 400- to 1000-DPI range, do not seem to contribute to any significant increase or decrease in the estimate of percent open sky.

Variation in the measurements of percent open sky collected from a number of locations under a contiguous forest canopy using a single technique may be attributed to two main factors: a) the natural variability of gap sizes within heterogeneous forest canopies, and/or b) poor measurement repeatability associated with the analytical method. Table 1 summarizes HEMIPHOT and PAMAP GIS percent-open-sky data averaged for each of the 24 chronosequence plots. The standard deviation associated with each of the means is a reliable measure of variance and therefore a function of the two factors stated above; i.e., analytical repeatability and the natural variability in gap size. Comparison of the standard deviation associated with each of the techniques has provided an indirect mechanism for evaluating analytical performance. The standard deviation of HEMIPHOT percent-open-sky data is slightly larger than that produced by the PAMAP GIS application. This finding is most likely due to additional user error associated with HEMIPHOT image registration techniques. An analysis of variance (ANOVA) of these data, however, suggests that these differences are not statistically significant.

Inadequate image registration techniques may account for a significant portion of the analytical error introduced during hemispherical image processing. One of the difficulties associated with image registration is in adequately defining the horizontal extent of the hemispherical photograph. This problem becomes more acute with photographs that are so underexposed that the boundary between the exposed and unexposed portion of the film is lost. A new registration technique was implemented within the PAMAP GIS application whereby a random 256-colour palette was assigned to a gradational gray-scale palette ranging from black to white. The effect of this procedure was to uncover the true boundary between the exposed and unexposed portion of the picture, which in turn permitted accurate and repeatable partitioning of the image.

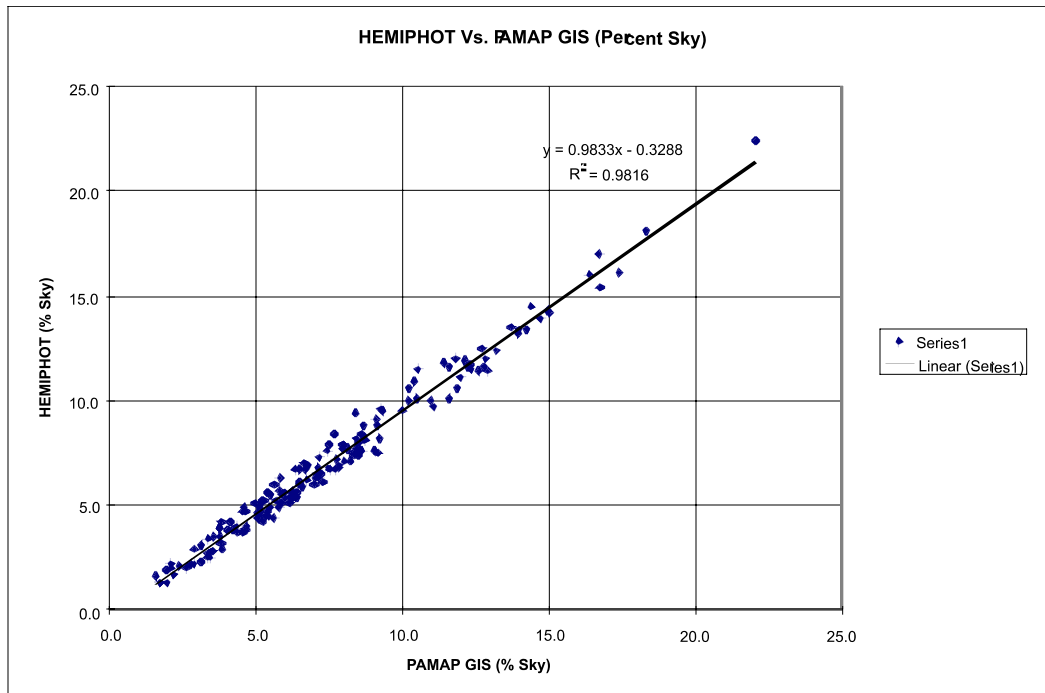


FIGURE 18. Scattergram, trendline, and coefficient of determination (R^2) plotted for estimates of percent open sky output by HEMIPHOT and PAMAP GIS.

TABLE 1. Comparison of mean percent-open-sky results produced by HEMIPHOT and PAMAP GIS

Site	Mean HEM % Sky	Mean PAM % Sky	Δ % Sky (H-P)	% Diff % Sky (H/P)	StdDev HEM % Sky	StdDev PAM % Sky	Δ StdDev % Sky (H-P)	% Diff StdDev % Sky (H/P)
KLA82	1.99	2.23	-0.24	10.90	0.61	0.52	0.10	-18.73
KLA83	2.59	2.76	-0.17	6.17	0.96	0.90	0.07	-7.30
KLA84	5.97	6.21	-0.24	3.80	1.92	1.84	0.08	-4.10
KOK22	7.56	7.80	-0.24	3.05	2.65	2.68	-0.02	0.87
KOK23	7.83	8.13	-0.30	3.71	2.22	1.76	0.47	-26.49
KOK24	13.29	14.07	-0.79	5.60	2.15	2.45	-0.31	12.44
NAN33	9.60	10.00	-0.40	4.02	4.25	4.19	0.06	-1.46
NAN34	10.90	10.93	-0.03	0.24	6.73	6.41	0.32	-5.02
NAN35	5.17	5.67	-0.50	8.78	1.87	1.89	-0.02	1.19
NIT72	4.80	4.97	-0.17	3.45	1.58	1.45	0.13	-8.83
NIT73	3.05	3.79	-0.74	19.48	0.80	0.76	0.05	-6.08
NIT74	8.46	8.58	-0.13	1.47	3.57	3.38	0.19	-5.69
REN52	5.37	5.98	-0.61	10.14	1.67	1.93	-0.26	13.55
REN53	6.27	6.80	-0.53	7.82	1.01	0.98	0.03	-3.58
REN54	11.47	12.15	-0.68	5.56	2.70	2.55	0.15	-6.05
RGC62	4.84	5.40	-0.56	10.33	0.70	0.68	0.01	-1.90
RGC63	6.27	7.26	-0.99	13.63	1.49	1.65	-0.16	9.48
RGC64	5.87	6.21	-0.34	5.40	2.26	2.29	-0.03	1.47
VWN12	8.49	8.90	-0.41	4.63	2.26	2.48	-0.22	8.84
VWN13	8.10	8.29	-0.19	2.27	2.49	2.85	-0.35	12.40
VWN15	10.00	11.00	-1.00	9.10	3.02	2.98	0.04	-1.19
VWS02	4.09	4.61	-0.52	11.38	1.66	1.45	0.21	-14.16
VWS05	8.09	8.79	-0.70	7.98	1.87	1.88	-0.01	0.30
VWS06	10.26	10.76	-0.50	4.65	3.74	3.82	-0.08	2.14

NOTE: Mean and standard deviation estimates of percent sky were calculated using seven (7) sub-plot measurements per plot.

5.4.2 Effective leaf area index (L_e)

Both HEMIPHOT and the PAMAP GIS application have utilized a linear averaging algorithm to estimate L_e (Welles and Norman 1991; LI-COR Inc. 1992). This model is based on a Poisson probability distribution and works well provided foliage is randomly distributed and the ground and canopy surfaces are not inclined (Neumann *et al.* 1989; Welles and Norman 1991; ter Steege 1993). Both these assumptions, however, are untrue in the context of this study, since all sites were located within mountainous terrain under conifer canopies that are clumped and highly organized. The effects of foliage clumping on indirect measures of LAI are well documented in the literature (Chen and Black 1991; Gower and Norman 1991; Chen and Black 1992; Smith 1993; Fassnacht *et al.* 1994; Chen *et al.* 1997). Neumann *et al.* (1989) and Fassnacht *et al.* (1994) have all shown that foliage clumping strongly underestimates LAI, and that alternative probability distributions (e.g., negative binomial, Markov models, etc.) plus the application of site- and species-specific clumping indices may be used to improve the predictability of indirect measurement techniques. Neither HEMIPHOT nor PAMAP GIS applications have included any provision for foliage clumping, although the PAMAP application has attempted to compensate for surface orientation effects (see Appendix C). These slope-correction factors have only been tested on a few hemispherical images, and were not applied to the entire dataset.

Figure 19 shows a linear regression of the L_e estimates produced by HEMIPHOT and PAMAP GIS applications. With the exception of a few noticeable outliers, there is a significant correlation ($R^2 = .96$) between the two datasets. HEMIPHOT produces L_e measures that are slightly larger than PAMAP GIS, but this is to be expected given the higher PAMAP GIS estimates of percent open sky.

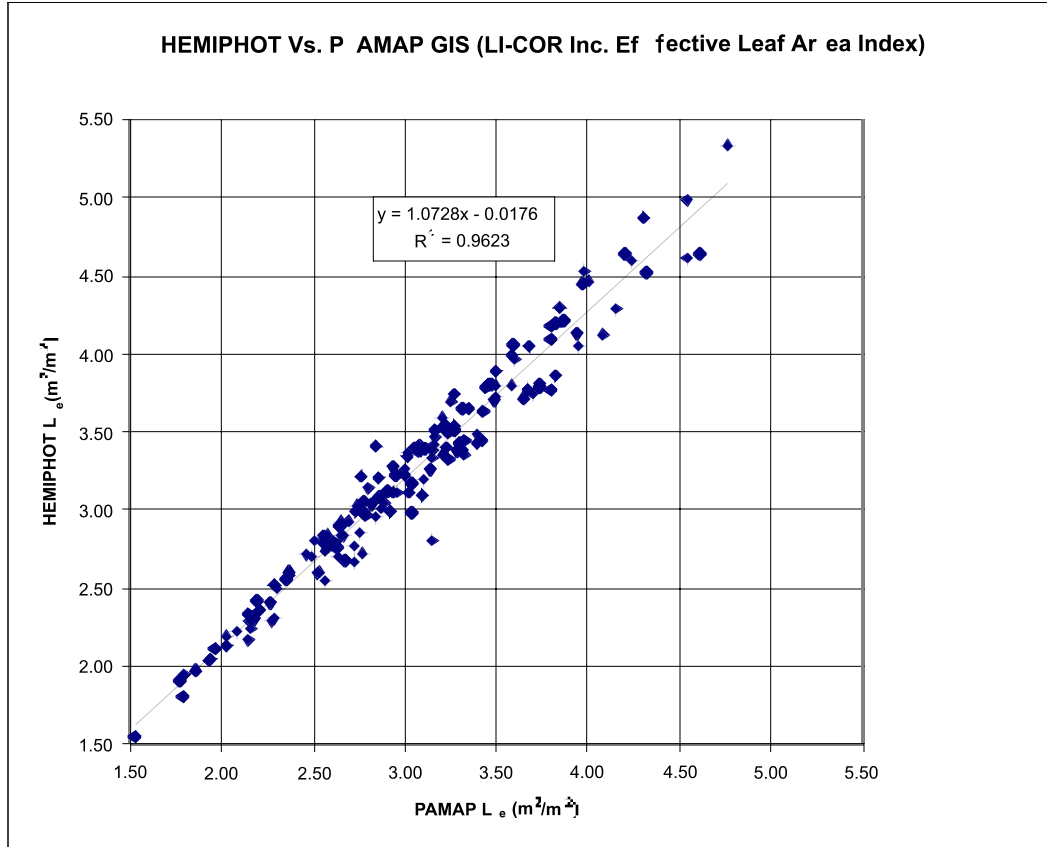


FIGURE 19. Correlation between HEMIPHOT and PAMAP L_e estimates.

6.0 TECHNICAL SHORTCOMINGS AND RECOMMENDATIONS

Hemispherical canopy photography and computerized image analysis techniques have proven to be powerful indirect methods for measuring various components of canopy structure and understory light regime. Numerous advances in hemispherical image analysis have taken place over the last decade, which are directly related to evolving computer, photographic, and digital technologies and scientific modeling methods. However, it has become apparent through the course of this research that current hemispherical image analysis programs and methods have not kept pace with supporting technologies, and, as a consequence, these intrinsic weaknesses limit the full potential of the technique. Five areas of improvement have been identified that would benefit this technology: a) digital image enhancement and photography, b) projection distortion and image registration methods, c) software design and implementation, d) consolidation and standardization of theoretical models, and e) post-processing calibration and correction for climatic and landscape-level influences.

6.1 Digital Image Enhancement and Photography

Modern photographic film, filters, and digital image enhancement technologies offer remarkable opportunity to improve hemispherical image quality and contrast. These improvements in turn would facilitate a higher success rate in the classification of sky and non-sky pixels during the threshold process. The potential for digital image enhancement is increased using true-colour (24-bit) images because various combinations of techniques can be applied to any one or all of the three RGB planes. Image enhancement methods include the application of a) digital filters to mathematically recombine neighbouring pixels, b) overlays to splice multiple RGB planes or even separate images, and c) tools that modify the frequency and magnitude of pixel spectra. All of these digital techniques should be explored and tested to see what improvement can be made in the exactness of sky and non-sky pixel classification.

Relatively expensive, high-resolution, true-colour digital cameras have been commercially available for sometime now. At present, both Minolta and Nikon Inc. (e.g., Nikon E2 Series) offer high-end SLR-type digital cameras that will support interchangeable lenses and 1280×1000 (24-bit) image resolutions at a cost of \$10–15K. These prices, although extreme, are continuing to drop while image quality and resolution also improves. The benefits of incorporating digital image capture are a) elimination of the error, time, and cost associated with handling, development, and scanning of traditional photographic films, and b) the ability to produce a streamlined data-capture and image analysis system with enough speed and versatility for complete throughput in the field.

6.2 Projection Distortions and Image Registration

Two kinds of unnecessary errors are typically introduced into current hemispherical image analyses: a) optical distortion errors associated with image projection through photographic lens and 35-mm film scanners and b) inaccuracies related to image registration and pixel assignment techniques. Most hemispherical image analysis systems assume that all optical distortion inherent in any projected canopy image can be adequately predicted by a standard projection transformation (Appendix B). Specific research presented within this report and by Herbert (1986, 1987) has shown this assumption to be untrue. Procedures to define and control for these optical distortions should be incorporated into future image analysis systems. Digital image capture in the field will eliminate the cumulative distortion effects imposed by film scanning.

Image registration may be defined as the process used to determine the horizontal extent of the projected hemispherical image and the spatial orientation of each pixel relative to a known point. Imprecise image registration will cause a) erroneous estimates of gap fraction position, magnitude, and distribution, and b) inconsistencies in suntrack placement. The consequence of these combined errors is poor measurement repeatability and less-reliable estimates of understory radiation flux and L_e . Current registration tools and techniques are limited at best. Registration can be improved by modifying both the photographic equipment and software application tools. Camera lenses could be modified using external LED lights so that the film would automatically record the horizontal extent of the hemisphere and orientation relative to true north. Another solution is to develop more-graphical software interfaces that will allow quick and easy placement of vector circles to define the hemispherical extent of images. The vector circles must be fully expandable, positioned by drag and drop, and able to rotate clockwise or counterclockwise to define true north. Third-party graphics applications produced by commercial vendors do exist that allow integration of vector drawing tools with standard raster image formats. The availability of these commercial products should also be looked at.

6.3 Software Design and Implementation

Obscure scientific software rarely makes it into the commercial sector. As a result, many of these applications have poor graphical user interfaces (GUI), use limited data structures, require specialized computer equipment, and are fraught with run-time errors. Numerous program routines for reading, writing, and displaying standard image formats, defining areas of interest, and calculating area, etc. have all been written before by professional programmers. These routines have been packaged as software development kits (SDK) that can be used to produce stand-alone custom applications. The use of third-party tools would free the scientist from the details of GUI development, image manipulation and enhancement, and spatial measurement tasks, and allow greater focus on application theory and program organization. Hemispherical applications are well suited to vector and raster data structures because of the need to select, manipulate, and measure physical parameters within precise areas of interest. Many of these manipulations are therefore spatial in nature, and have already been created by GIS and other image analysis developers that produce commercially available SDKs. All hemispherical applications should also allow easy digital access to both raw and processed summary data so that site-specific calibrations can be applied by the end-user.

6.4 Standardization of Theoretical Models

The fact that hemispherical programs can produce such varied results would suggest that there is a need to consolidate and standardize theoretical definitions, models, and procedures. A number of solar radiation models have been published that are recognized by groups such as the International Energy Agency (IEA) and have undergone considerable testing and calibration (Hay and McKay 1988). Although mathematical models are seldom perfect and most often better suited to one part of the globe than another, standardization provides a mechanism for comparing regional datasets and procedures. Two levels of the hemispherical canopy model require consolidation: a) estimation of direct and diffuse solar irradiance incident on the top of a tree canopy, and b) gap light transmission through the forest overstory. Methods published by groups such as the IEA may be used to estimate incident light levels above the canopy; however, specific, recognized research published by forest meteorologists, ecologists, etc. must be used to model light attenuation through the canopy.

Indirect methods for evaluating various measures of canopy structure are strongly dependent upon assumed foliage orientation distributions (Norman and Campbell 1989; Fassnacht *et al.* 1994). In most cases, LAI models rely on a perfectly random distribution of foliage elements. Natural forests, however, rarely conform to this assumption, and as a result optical methods significantly underestimate, or in rare cases overestimate, LAI measures obtained using direct sampling techniques (Whitford *et al.* 1995). Foliage clumping along shoots, branches, and stems contribute to the non-random distribution of foliage elements. Chen and Black (1992) proposed the term “effective LAI” (L_e) to describe LAI data generated using optical methods because these techniques do not distinguish between the surface area of photosynthetic and non-photosynthetic matter, nor are they capable of measuring the overlap of clumped canopy elements. Chen *et al.* (1997) have done a considerable amount of work trying to standardize optical methods for determining LAI in natural forest stands. In an effort to support standardization, new hemispherical image software should integrate well-accepted L_e algorithms such as the one developed by Miller (1967). The quality of L_e data might also be improved by providing added software options for aggregating and excluding gap fraction data.

6.5 Post-processing Corrections for Climatic and Landscape-level Influences

Hemispherical models are simplistic in that they disregard the influence of daily or longer-term climatic cycles and site orientation and landscape relief. The diurnal cycle of clouds, rain, fog, pollution, etc. play an enormous role in the quality and quantity of direct and diffuse light that is available at any one time (Iqbal 1983). Hay (1979), Gates (1980), and Iqbal (1983) have all shown that slope magnitude and orientation strongly influences incident light levels. Hemispherical models also assume that the tree canopy itself is the only barrier to global radiation reaching the forest floor. This is obviously untrue in an area of rugged relief where landform geometry can significantly alter the distribution of direct and diffuse light. The west coast of British Columbia is an environment characterized by rugged mountains and unpredictable maritime climatic conditions, and therefore an area that would benefit most from more-sophisticated hemispherical models.

Numerous solar radiation models have already been developed for inclined sites (e.g., Hay 1979; Gates 1980; Iqbal 1983; Hay and McKay 1988). It is possible, however, to construct post-processing methods for both climate and terrain influences when suitable empirical data exists. The ability to integrate climatic influences into clear sky models is most often limited by the scarcity of weather data. Iqbal (1983) mentioned a number of studies using observed sunshine hours and percent-cloud-cover information to modify modeled solar radiation data. In contrast, large-scale topographic data are inexpensive and far more ubiquitous than climatic information. Digital elevation models (DEM), in combination with GIS interviewability algorithms, can be used to estimate the precise timing and frequency of shading that a site will experience over the course of a day as a result of local relief. These data could in turn be used to correct above-canopy radiation estimates. It is possible to alter the complexity of hemispherical models; however, the ease with which these modifications can be implemented depends entirely on the access available to intermediate or summary data generated by current hemispherical models.

7.0 REFERENCES

- Anderson, M.C. 1964. Studies of the woodland light climate I. The photographic computation of light condition. *Journal of Ecology* 52: 27–41.
- . 1971. Radiation and crop structure. Pages 77–80 in Z. Sestak, J. Catsky and P.G. Jarvis, eds. *Plant Photosynthesis Production, Manual of Methods*, Dr. Junk N.V. Publishers, The Hague, The Netherlands.
- Becker, P.; Erhart, D.; Smith, A.P. 1989. Analysis of forest light environments Part I. Computerized estimation of solar radiation from hemispherical canopy photographs. *Agricultural and Forest Meteorology* 44: 217–232.
- Black, T.A.; Chen, J.M.; Xuhui, L.; Sagar, R.M. 1991. Characteristics of shortwave and longwave irradiances under a Douglas-fir forest stand. *Canadian Journal of Forest Research* 21: 1020–1028.
- Canham, C.D. 1988. An index for understory light levels in and around gaps. *Ecology* 69(5): 1634–1638.
- . 1995. GLI/C: Software for calculation of light transmission through forest canopies using color fisheye photography. Unpublished manuscript. Institute of Ecosystem Studies, Box AB, Millbrook, NY. 7 p.
- . (*per. comm.*). 1996. E-mail correspondence dated January 13 to November 10, 1996. Institute of Ecosystem Studies, Millbrook, NY.
- Canham, C.D.; Finzi, A.C.; Pacala, S.W.; Burbank, D.H. 1994. Causes and consequences of resource heterogeneity in forests: interspecific variation in light transmission by canopy trees. *Canadian Journal of Forest Research* 24: 337–349.
- Chason, J.W.; Baldocchi, D.D.; Huston, M.A. 1991. A comparison of direct and indirect methods for estimating forest canopy leaf area. *Agricultural and Forest Meteorology* 57: 107–128.
- Chazdon, R.L.; Fetcher, N. 1984. Photosynthetic light environments in a lowland tropical rain forest in Costa Rica. *Journal of Ecology* 72: 553–564.
- Chazdon, R.L.; Field, C.B. 1987. Photographic estimation of photosynthetically active radiation: evaluation of a computerized technique. *Oecologia (Berlin)* 73: 525–532.
- Chazdon, R.L.; Pearcy, R.B. 1991. The importance of sunflecks for forest understory plants. *BioScience* 41(11): 760–766.
- Chen, H.Y.N.; Klinka, K.; Kayahara, G.J. 1996. Effects of light on growth, crown architecture, and specific leaf area for naturally established *Pinus contorta* var. *latifolia* and *Pseudotsuga menziesii* var. *glauca* saplings. *Canadian Journal of Forestry* 26: 1149–1157.

-
- Chen, J.M.; Black, T.A. 1991. Measuring vegetation area index of plant canopies with branch architecture. *Agricultural and Forest Meteorology* 57: 1–12.
- _____. 1992. Defining vegetation area index for non-flat leaves. *Plant, Cell and Environment* 15: 421–429.
- Chen, J.M.; Black, T.A.; Adams, R.S. 1991. Evaluation of hemispherical photography for determining plant area index and geometry of a forest stand. *Agricultural and Forest Meteorology* 56: 129–143.
- Chen, J.M.; Black, T.A.; Price, D.T.; Carter, R.E. 1993. Model for calculating photosynthetic photon flux densities in forest openings on slopes. *Journal of Applied Meteorology* 32: 1656–1665.
- Chen, J.M.; Cihlar, J. 1995. Plant canopy gap-size analysis theory for improving optical measurements of leaf-area index. *Applied Optics* 34 (27): 6211–6222.
- Chen, J.M.; Rich, P.M.; Gower, S.T.; Norman, J.M.; Plummer, S. 1997. Leaf area index of boreal forests: theory, techniques, and measurements. *Journal of Geophysical Research (BOREAS special issue, in press)*.
- Deblonde, G.; Penner, M.; Royer, A. 1994. Measuring leaf area index with the LI-COR LAI-2000 in pine stands. *Ecology* 75: 1507–1511.
- Duffet-Smith, P. 1990. *Practical astronomy with your calculator*. Cambridge University Press, Cambridge, United Kingdom.
- Easter, M.J.; Spies, T.A. 1994. Using hemispherical photography for estimating photosynthetic photon flux density under canopies and in gaps in Douglas-fir forests of the Pacific Northwest. *Canadian Journal of Forestry Research* 24: 2050–2058.
- Fassnacht, K.S.; Gower, S.T.; Norman, J.M.; McMurtrie, R.E. 1994. A comparison of optical and direct methods for estimating foliage surface area index in forests. *Agricultural and Forest Meteorology* 71: 183–207.
- Flint, A.L.; Childs, S.W. 1987. Calculation of solar radiation in mountainous terrain. *Agricultural and Forest Meteorology* 40: 233–249.
- Gates, D.M. 1980. *Biophysical ecology*. Springer-Verlag, New York, NY.
- Gholtz, H.L.; Fitz, F.K.; Waring, R.H. 1976. Leaf area differences associated with old-growth forest communities in the western Oregon Cascades. *Canadian Journal of Forest Research* 6: 49–57.
- Gower, S.T.; Norman, J.M. 1991. Rapid estimation of vegetation area index in conifer and broad-leaf plantations. *Ecology* 72(5): 1896–1900.
- Hay, J.E. 1979. *An analysis of solar radiation data of British Columbia*. Ministry of Environment, Resource Analysis Branch, RAB Bulletin 14. 125 p.

-
- Hay, J.E.; McKay, D.C. 1988. Final report IEA task IX—Calculation of solar irradiances for inclined surfaces: verification of models which use hourly and daily data. International Energy Agency, Solar Heating and Cooling Programme.
- Herbert, T.J. 1986. Calibration of fisheye lenses by inversion of area projections. *Applied Optics* 25(12): 1875–1876.
- _____. 1987. Area projections of fisheye photographic lenses. *Agricultural and Forest Meteorology* 39: 215–223.
- Iqbal, M. 1983. An introduction to solar radiation. Academic Press, Orlando, FL.
- Lang, A.R.G.; Yueqin, X. 1986. Estimation of vegetation area index from transmission of direct sunlight in discontinuous canopies. *Agricultural and Forest Meteorology* 37: 229–243.
- Lertzman, K.P.; Sutherland, G.D.; Inselberg, A.; Saunders, S.C. 1996. Canopy gaps and the landscape mosaic in a coastal temperate rain forest. *Ecology* 77(4): 1254–1270.
- LI-COR Inc. 1992. LAI-2000 Plant Canopy Analyzer: Operating manual. April 1992. LI-COR, Inc. Lincoln, Nebraska.
- Marshall, J.D.; Waring, R.H. 1986. Comparison of methods of estimating leaf-area index in old-growth Douglas-fir. *Ecology* 67(4): 975–979.
- McGhee, R. (*per. comm.*). 1995. E-mail correspondence. School of Resource and Environmental Management (REM), Simon Fraser University, Burnaby, British Columbia.
- Miller, J.B. 1967. A formula for average foliage density. *Aust. J. of Bot.* 34: 141–144.
- Neumann, H.H.; Hartog, G.D.; Shaw, R.H. 1989. Leaf area measurements based on hemispheric photographs and leaf-litter collection in a deciduous forest during autumn leaf-fall. *Agricultural and Forest Meteorology* 45: 325–345.
- Nikon, Inc. 1996. Personal communication with Technical Services, Mississauga, Ontario.
- Norman, J.M.; Campbell, G.S. 1989. Canopy structure. Pages 301–325 in R.W. Pearcy, J. Ehrlinger, H.A. Mooney, and P.W. Rundel eds. *Plant ecology: field methods and instrumentation*. Chapman and Hall, London and New York.
- Pearcy, R.W. 1989. Radiation and light measurements. Pages 97–116 in R.W. Pearcy, J. Ehrlinger, H.A. Mooney, and P.W. Rundel eds. *Plant ecology: field methods and instrumentation*. Chapman and Hall, London and New York.
- Perry, S.G.; Fraser, A.B.; Thomson, D.W.; Norman, J.M. 1988. Indirect sensing of plant canopy structure with simple radiation measurements. *Agricultural and Forest Meteorology* 42: 255–278.
- Rich, P.M. 1988. Video image analysis of hemispherical canopy photography. Pages 84–95 in P.W. Mausel ed. *First Special Workshop on Videography*. American Society for Photogrammetry and Remote Sensing, Terre Haute, Indiana. May 19–20, 1988.

-
- _____. 1989. A manual for analysis of hemispherical canopy photography. Los Alamos National Laboratory Report LA-11732-M.
- _____. 1990. Characterizing plant canopies with hemispherical photographs. *Remote Sensing Reviews* 5(1): 13–29.
- Rich, P.M.; Clark, D.B.; Clark, D.A.; Oberbauer, S. 1993. Long-term study of solar radiation regimes in a tropical wet forest using quantum sensors and hemispherical photography. *Agricultural and Forest Meteorology* 65: 107–127.
- SAS Institute Inc. 1986. SAS Language and Procedures: Version 6.0, First Edition. SAS Institute Inc., Carey, NC.
- Smith, N.J. 1991. Predicting radiation attenuation in stands of Douglas-fir. *Forest Science* 37(5): 1213–1223.
- _____. 1993. Estimating vegetation area index and light extinction coefficients in stands of Douglas-fir (*Pseudotsuga menziesii*). *Canadian Journal of Forest Research* 23: 317–321.
- Smith, N.J.; Chen, J.M.; Black, T.A. 1993. Effects of clumping on estimates of stand vegetation area index using the LI-COR LAI-2000. *Canadian Journal of Forest Research* 23: 1940–1943.
- Stenberg, P.; Linder, S.; Smolander, H.; Flower-Ellis, J. 1994. Performance of the LAI-2000 plant canopy analyzer in estimating leaf area index of some Scots pine stands. *Tree Physiology* 14: 981–995.
- Strachan, I.B.; McCaughey, J.H. 1996. Spatial and vertical vegetation area index of a deciduous forest resolved using the LAI-2000 Plant Canopy Analyzer. *Forest Science* 42(2): 176–181.
- ter Steege, H. 1993. HEMIPHOT, a programme to analyze vegetation indices, light and light quality from hemispherical photographs. Unpublished manuscript, The Tropenbos Foundation, Wageningen, The Netherlands. 44 p.
- Trofymow, J.A.; Blackwell, B.A.; Porter, G.L.; Marshall, V.; Arskey, R.; Pollard, D. 1997. Chronosequences selected for research into the effects of converting coastal British Columbia old-growth forests to managed forests: an establishment report. BC-X-374. Nat. Res. Can., Can. For. Ser., Pacific Forestry Centre, Victoria, B.C. in press.
- Trofymow, J.A.; Leach, R.I. 1996. The effects of converting coastal old-growth to managed forests: Changes in site carbon and nutrient contents during post-disturbance succession. Phase 2.5: Vegetation area index and foliar biomass estimation. Unpublished report, Natural Resources Canada, Pacific Forestry Centre, Victoria, B.C.
- Vieglais, D. 1996. Personal communication via e-mail on December 10, 1996.
- Wang, Y.S.; Miller, D.R. 1987. Calibration of the hemispherical photographic technique to measure leaf area index distributions in hardwood forests. *Forest Science* 33 (1): 210–216.

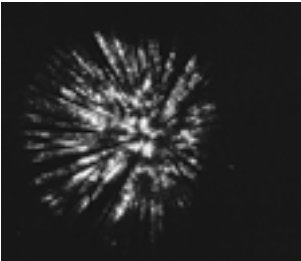
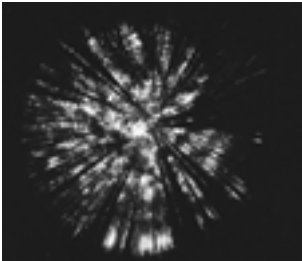

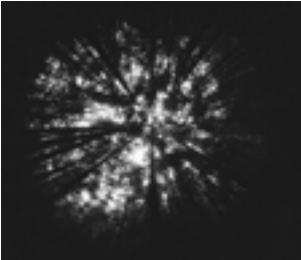
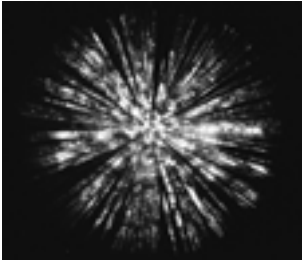
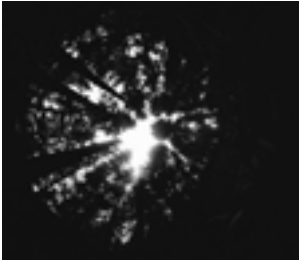
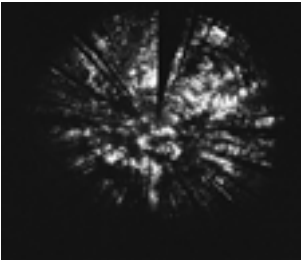
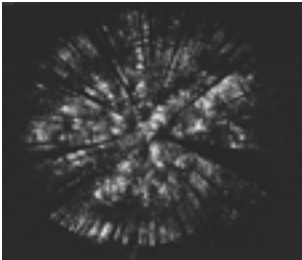
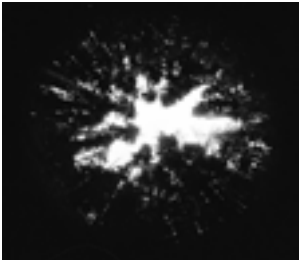
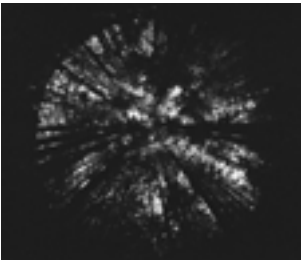
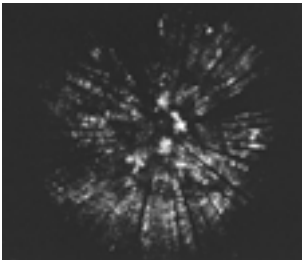
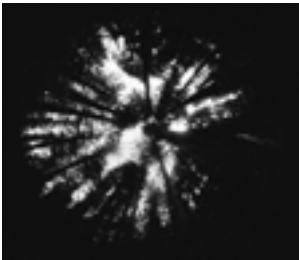
-
- Watson, D.J. 1947. Comparative physiological studies in the growth of field crops. I: Variation in net assimilation rate and leaf area between species and varieties, and within and between years. *Ann. Bot.* 11: 41–76.
- Welles, J.M.; Cohen, S. 1996. Canopy structure measurement by gap fraction analysis using commercial instrumentation. *Journal of Experimental Botany* 47 (302): 1135–1342.
- Welles, J.M.; Norman, J.M. 1991. Instrument for indirect measurement of canopy architecture. *Agronomy Journal* 83: 818–825.
- Whitford, K.R.; Colquhoun, I.J.; Lang, A.R.G.; Harper, B.M. 1995. Measuring leaf area index in a sparse eucalypt forest: a comparison of estimates from direct measurement, hemispherical photography, sunlight transmittance and allometric regression. *Agricultural and Forest Meteorology* 74: 237–249.



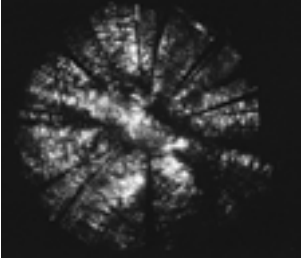
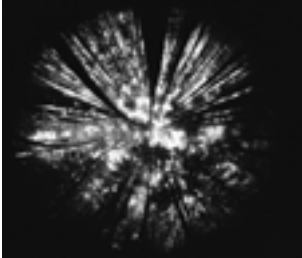
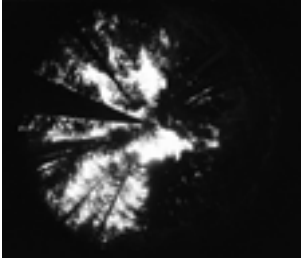
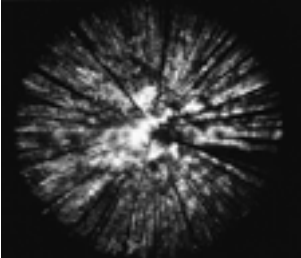
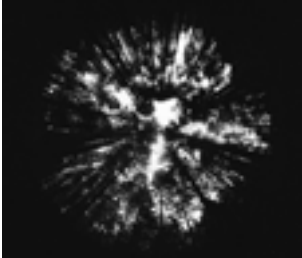
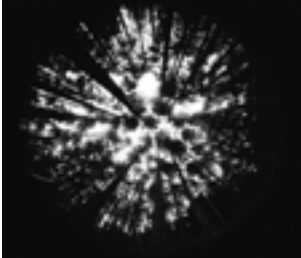
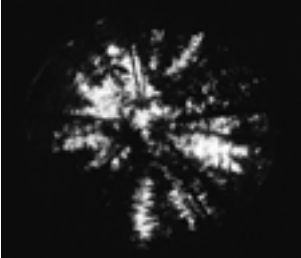
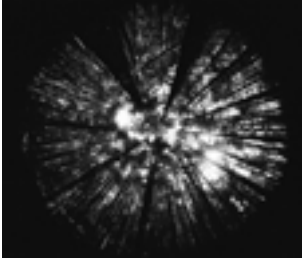
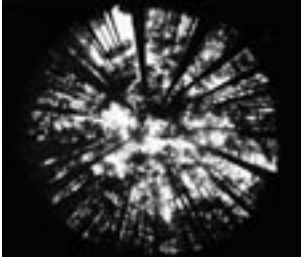
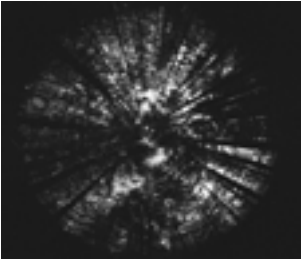
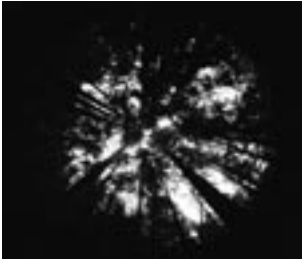
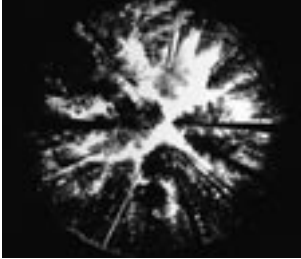
APPENDIX A.

Catalogue of Representative Hemispherical Photographs Collected at Eight
Chronosequences on Southern Vancouver Island

Select Hemispherical Canopy Photographs (West Side)

Immature	Mature	Old Growth
 <p>REN52-3.BMP % Open Sky = 5.4 $L_e = 3.27$</p>	 <p>REN53-5.BMP % Open Sky = 6.2 $L_e = 3.01$</p>	 <p>REN54-3.BMP % Open Sky = 13.9 $L_e = 2.08$</p>
 <p>RGC62-3.BMP % Open Sky = 5.9 $L_e = 3.15$</p>	 <p>RGC63-6.BMP % Open Sky = 9.2 $L_e = 2.56$</p>	 <p>RGC64-7.BMP % Open Sky = 6.5 $L_e = 3.23$</p>
 <p>NIT72-2.BMP % Open Sky = 5.1 $L_e = 3.28$</p>	 <p>NIT73-7.BMP % Open Sky = 3.1 $L_e = 3.85$</p>	 <p>NIT74-6.BMP % Open Sky = 11.6 $L_e = 2.89$</p>
 <p>KLA82-1.BMP % Open Sky = 2.4 $L_e = 3.94$</p>	 <p>KLA83-1.BMP % Open Sky = 2.1 $L_e = 4.16$</p>	 <p>KLA84-3.BMP % Open Sky = 8.5 $L_e = 2.64$</p>

Select Hemispherical Canopy Photographs (East Side)

Immature	Mature	Old Growth
 <p>VWS02-6.BMP % Open Sky = 5.6 $L_e = 3.06$</p>	 <p>VWS05-3.BMP % Open Sky = 8.5 $L_e = 2.58$</p>	 <p>VWS06-5.BMP % Open Sky = 12.2 $L_e = 2.18$</p>
 <p>VWN12-2.BMP % Open Sky = 7.7 $L_e = 2.94$</p>	 <p>VWN13-3.BMP % Open Sky = 8.4 $L_e = 2.57$</p>	 <p>VWN15-7.BMP % Open Sky = 12.3 $L_e = 2.18$</p>
 <p>KOK22-1.BMP % Open Sky = 8.7 $L_e = 2.62$</p>	 <p>KOK23-4.BMP % Open Sky = 7.5 $L_e = 2.78$</p>	 <p>KOK24-5.BMP % Open Sky = 17.4 $L_e = 1.77$</p>
 <p>NAN35-4.BMP % Open Sky = 3.5 $L_e = 3.60$</p>	 <p>NAN33-3.BMP % Open Sky = 8.6 $L_e = 2.59$</p>	 <p>NAN34-3.BMP % Open Sky = 16.7 $L_e = 1.80$</p>

APPENDIX B.

Measurement of Fisheye Lens Distortion and the Effect on the Calculation of Gap
Fraction Magnitude and Distribution, Percent Open Sky, and L_e

B-1 Introduction

Some hemispherical image analysis software, such as HEMIPHOT and GLI/C, assume that radial distortions on the image plane are identical to the geometry predicted by a theoretical polar projection. Direct calibration of a few commercially available lenses, (e.g., Canon, Nikon, Spiratone), indicates that significant angular distortion occurs between the optical axis of the lens and its full field of view ($\cong 90^\circ$), and that these distortions cannot be corrected using a standard projection transformation (e.g., orthographic, polar, stereographic, etc.) (Herbert 1987). Herbert (1987) has suggested that even small deviations between theoretical and measured angular lens distortions may produce large errors in estimates of canopy gap size, shape, and distribution. Variation in the radial position of points on the image plane is demonstrated to be negligible at different angles of azimuth around the lens (Herbert 1987). Angular distortion in the vertical plane, however, is significant, but easily corrected provided accurate calibration data are acquired via direct optical measure or through the lens manufacturer. The photographic lens used in this study was a Nikkor 8-mm f/2.8 fisheye lens produced by Nikon Inc. The following text details the methods used to calculate the specific distortions inherent in the Nikkor lens, and also outlines the direct consequences of ignoring this procedure on estimates of gap fraction distribution, percent open sky, and L_e .

B-2 Determining True Lens Distortion

Correct calibration of the optical properties of a photographic lens is difficult without access to adequate testing facilities. Lens manufacturers, however, often publish factory calibration data for specialty lenses that have been designed specifically for photogrammetric applications (Table B-1). These technical data should indicate where points in the hemispherical object region would be projected onto the image plane (Figure B-1). For example, a point (P) located at 55.67° in the sky hemisphere will be projected to a point (P') located exactly 7.5 mm from the nadir (centre) of the image plane by the Nikkor 8-mm f/2.8 fisheye lens, (per.comm., Nikon Inc. 1996). The same point located at 7.5 mm from the image centre would project to a point at 58.70° in the hemispherical object region if the lens followed the geometry of a true polar projection. The angular deviation between the point predicted by a polar projection and the Nikkor lens is 3.03° .

The effect of radial distortion on area calculations is more apparent when these angular deviations are projected onto the image plane itself. For example, a point located at 60° in the sky hemisphere will be projected to a point located at 7.67 and 8.04 mm from the image centre according to the transformation predicted by the polar and Nikkor projections, respectively. The deviation in radial measure is therefore only 0.37 mm on the image plane. Assuming that these two points are radii of circles sharing the same origin point as the image plane, it is possible to calculate the effect that this small amount of radial distortion will have on area measurements. In this case, a 4.6% (i.e., $0.37 \text{ mm}/8.04 \text{ mm}$) difference in radial measure translates to a 9.0% ($18.26 \text{ mm}^2/203.08 \text{ mm}^2$) difference in circular area.

TABLE B-1. Calibration data supplied by Nikon Inc. for the Nikkor 8-mm f/2.8 fisheye lens. Radial distance and zenith angle are measured from the centre of the image plane and from the optical axis of the lens, respectively.

Radial Distance (mm)	Zenith (θ°) (Nikkor)	$\Delta \theta^\circ$
0.0	0.00	
0.5	3.58	3.58
1.0	7.17	3.59
1.5	10.76	3.59
2.0	14.36	3.60
2.5	17.98	3.62
3.0	21.62	3.64
3.5	25.27	3.65
4.0	28.95	3.68
4.5	32.66	3.71
5.0	36.40	3.74
5.5	40.17	3.77
6.0	43.98	3.81
6.5	47.83	3.85
7.0	51.73	3.90
7.5	55.67	3.94
8.0	59.67	4.00
8.5	63.72	4.05
9.0	67.84	4.12
9.5	72.03	4.19
10.0	76.31	4.28
10.5	80.69	4.38
11.0	85.21	4.52
11.5	89.97	4.76

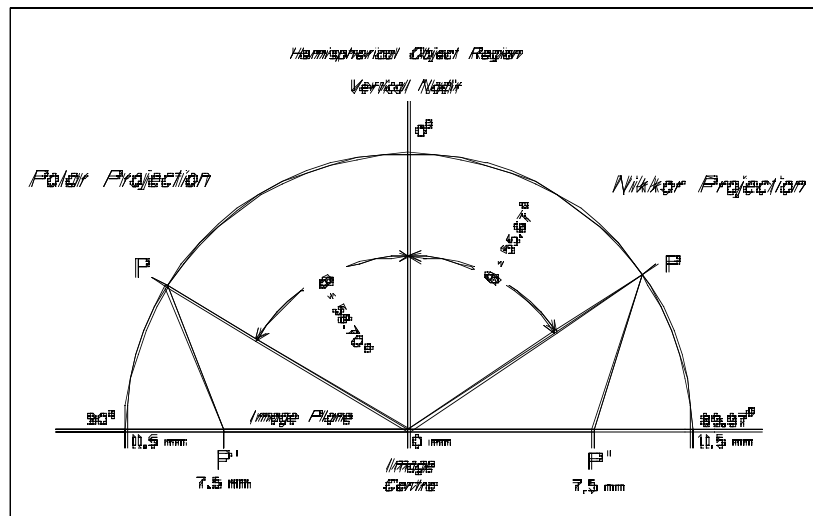


FIGURE B-1. Calibration data indicate how points in the hemispherical object region (P) are projected onto the image plane (P').

B-3 Constructing a Calibration Function

A mathematical function to accurately predict where points in the sky hemisphere will be projected on the image plane can be estimated by fitting the lens calibration data to a 6th order polynomial equation (Herbert 1986). The curve-fitting procedure is not straightforward due to the fact that the equation must be constrained to fixed points of 0 mm at $\theta = 0^\circ$ and 11.5 mm when θ is equal to the lens' full field of view (i.e., 89.97° for the Nikkor lens). Herbert (1986) proposed a mathematical method to constrain a best-fit line. Such procedures, however, are often unnecessary if enough calibration data are available from the manufacturer and the hemispherical application does not require an extremely high degree of spatial resolution close to the image centre or horizon. SAS statistical procedures allow the user to constrain the curve-fitting technique so that the best-fit line intercepts the y-axis at zero when $x = 0$ (SAS Institute Inc. 1986). The calibration function determined by SAS for the Nikkor 8-mm f/2.8 fisheye lens is as follows:

$$P' = c_1 P + c_2 P^2 + c_3 P^3 + c_4 P^4 + c_5 P^5 + c_6 P^6 \quad (\text{B.1})$$

where P' is the distance measured in millimeters from the centre of the image, P is the zenith angle (θ) in the hemispherical object region, and the numerical coefficients are: $c_1 = 0.139869$, $c_2 = -4.4195E-5$, $c_3 = 7.65E-7$, $c_4 = -6.672396E-8$, $c_5 = 9.094432E-10$, and $c_6 = -4.28448E-12$. Figure B-2 shows the best-fit line plotted for the 24 pairs of calibration points obtained from Nikon, Inc.

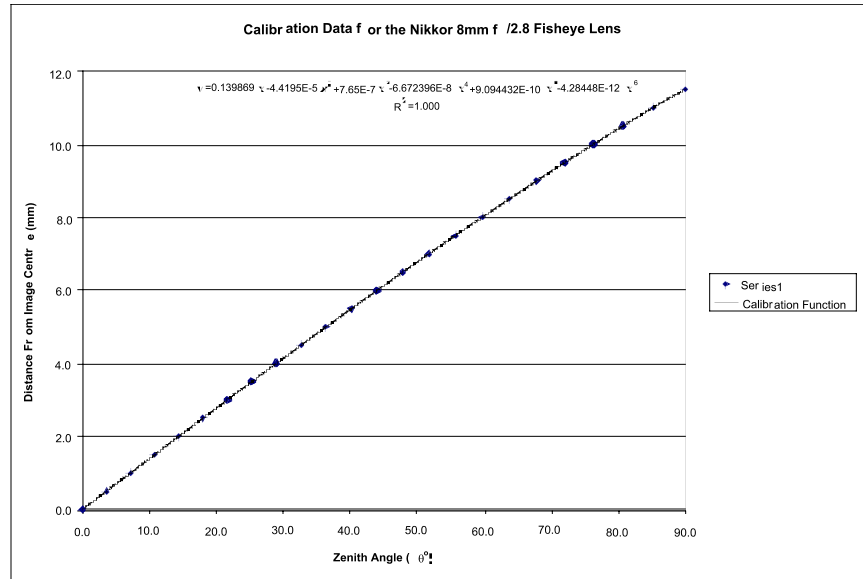


FIGURE B-2. Calibration curve constructed using a 6th order polynomial function. The calibration function must be constrained so that $P=0^\circ$ at $P'=0$ mm, and $P=89.97^\circ$ at $P'=11.5$ mm.

B-4 Calculating Relative Area Distortion

It has been shown that points within a hemispherical object region will project to various points on the image plane depending on the true geometric distortion of the lens. It would follow then that small deviations in the angular distortion of points might translate to substantial area distortion, depending on where these deviations occur within the hemispherical object region. Relative area distortions for any projection are easily calculated by dividing the image plane into concentric rings of equal interval and then projecting each of the concentric rings as arcs onto the sky hemisphere. The area of a ring (P_A) centred on the nadir of the image plane is given by:

$$P_A = \pi r_2^2 - \pi r_1^2 \quad (\text{B.2})$$

where r_2 is the maximum radial distance (in millimeters) of the ring interval, and r_1 is the minimum radial distance (in millimeters) of the bounding ring interval. To find the corresponding projected area on the sky hemisphere, the positions of both r_1 and r_2 must be projected onto the sky hemisphere. The area of a projected sphere segment (H_A) contained by the maximum (θ_2) and minimum (θ_1) angle of zenith is defined by:

$$H_A = 2\pi R^2 (\cos \theta_1 - \cos \theta_2) \quad (\text{B.3})$$

where R is the radius of the hemisphere in millimeters, θ_1 is the smaller angle of zenith measured in degrees, and θ_2 is the larger angle of zenith measured in degrees. The ratio of projected hemispherical area to image area at selected intervals throughout the full field of view of the lens can be calculated by dividing the area of a projected sphere segment by the area of a corresponding ring in the image plane:

$$\frac{H_A}{P_A} = \frac{2\pi R^2 (\cos \theta_1 - \cos \theta_2)}{\pi r_2^2 - \pi r_1^2} \quad (\text{B.4})$$

The ratio of projected spherical area to image area can be further reduced to show the variability in relative area distortion for objects projected on the sky hemisphere from the zenith to the horizon. Area distortion relative to that occurring at zenith angle 0° can be measured using the following equation:

$$R\left(\frac{H_A}{P_A}\right) = \frac{H_{A_i}}{P_{A_i}} \bigg/ \frac{H_{A_n}}{P_{A_n}} \quad (\text{B.5})$$

where the numerator represents the ratio of spherical area to projected image area for the ring interval closest to the zenith, and the denominator is the ratio of spherical area to projected image area for each successive ring interval from 0° to 90° .

Table B-2 and Figure B-3 present the distribution of relative area distortions calculated for a polar projection and the Nikkor 8-mm f/2.8 fisheye lens. The relative area distortion curves for the true polar and Nikkor projections are markedly different. These data indicate that objects projected at a zenith angle of approximately 88° using a true polar projection will appear 1.54% larger than objects projected at zenith angles close to 0° . In contrast, objects projected using the Nikkor fisheye lens have a maximum distortion of 7% at zenith angles between 82° and 86° . Herbert (1987) has noted that the Nikkor lens more closely approximates the image area distortions produced by a Lambert's equal-area projection than it does a polar projection. The difference in mean area distortion between the two projections is 14.56% with a maximum difference of 47.9% occurring at zenith angle 88.04° . These differences are significant because most hemispherical image analysis software programs, including HEMIPHOT and GLI/C, assume that the

distortion inherent in fisheye photographs can be corrected using a simple polar projection transformation. This assumption is obviously untrue in the case of the Nikkor and other fisheye lenses that deviate from a true polar projection.

TABLE B-2. The distribution of relative area distortions for a theoretical polar and Nikkor 8-mm f/2.8 fisheye lens projection

Radial Distance (mm)	Zenith (θ°) (Nikkor)	Zenith (θ°) (Polar)	Diff. ($N\theta^\circ - P\theta^\circ$)	Zenith (θ°) Mid.-Pt. (Polar)	Image Area/Ring P_A	H_A (Nikkor)	H_A (Polar)	H_A/P_A (Nikkor)	H_A/P_A (Polar)	$R(H_A/P_A)$ (Nikkor)	$R(H_A/P_A)$ (Polar)	Δ $R(H_A/P_A)$
0.0	0.00	0.00	0.00	-	-	-	-	-	-	-	-	-
0.5	3.58	3.91	-0.33	1.96	0.79	1.62	1.94	2.06	2.47	1.00	1.00	0.0000
1.0	7.17	7.83	-0.66	5.87	2.36	4.88	5.80	2.07	2.46	1.00	1.00	0.0040
1.5	10.76	11.74	-0.98	9.78	3.93	8.11	9.64	2.07	2.45	1.00	1.00	0.0052
2.0	14.36	15.65	-1.29	13.70	5.50	11.35	13.43	2.06	2.44	1.00	1.01	0.0095
2.5	17.98	19.57	-1.59	17.61	7.07	14.62	17.16	2.07	2.43	1.00	1.02	0.0174
3.0	21.62	23.48	-1.86	21.52	8.64	17.88	20.82	2.07	2.41	1.00	1.02	0.0261
3.5	25.27	27.39	-2.12	25.43	10.21	21.06	24.37	2.06	2.39	1.00	1.03	0.0324
4.0	28.95	31.30	-2.35	29.35	11.78	24.32	27.81	2.06	2.36	1.00	1.04	0.0446
4.5	32.66	35.22	-2.56	33.26	13.35	27.55	31.12	2.06	2.33	1.00	1.06	0.0577
5.0	36.40	39.13	-2.73	37.17	14.92	30.74	34.28	2.06	2.30	1.00	1.07	0.0713
5.5	40.17	43.04	-2.87	41.09	16.49	33.87	37.29	2.05	2.26	1.01	1.09	0.0855
6.0	43.98	46.96	-2.98	45.00	18.06	37.02	40.12	2.05	2.22	1.01	1.11	0.1031
6.5	47.83	50.87	-3.04	48.91	19.63	40.09	42.77	2.04	2.18	1.01	1.13	0.1213
7.0	51.73	54.78	-3.05	52.83	21.21	43.18	45.21	2.04	2.13	1.01	1.16	0.1430
7.5	55.67	58.70	-3.03	56.74	22.78	46.04	47.44	2.02	2.08	1.02	1.18	0.1627
8.0	59.67	62.61	-2.94	60.65	24.35	49.01	49.46	2.01	2.03	1.03	1.21	0.1885
8.5	63.72	66.52	-2.80	64.57	25.92	51.70	51.24	1.99	1.98	1.03	1.25	0.2126
9.0	67.84	70.43	-2.59	68.48	27.49	54.48	52.78	1.98	1.92	1.04	1.28	0.2428
9.5	72.03	74.35	-2.32	72.39	29.06	57.07	54.08	1.96	1.86	1.05	1.33	0.2740
10.0	76.31	78.26	-1.95	76.30	30.63	59.70	55.13	1.95	1.80	1.06	1.37	0.3113
10.5	80.69	82.17	-1.48	80.22	32.20	62.23	55.91	1.93	1.74	1.07	1.42	0.3521
11.0	85.21	86.09	-0.88	84.13	33.77	65.04	56.44	1.93	1.67	1.07	1.48	0.4038
11.5	89.97	90.00	-0.03	88.04	35.34	68.95	56.71	1.95	1.60	1.06	1.54	0.4790

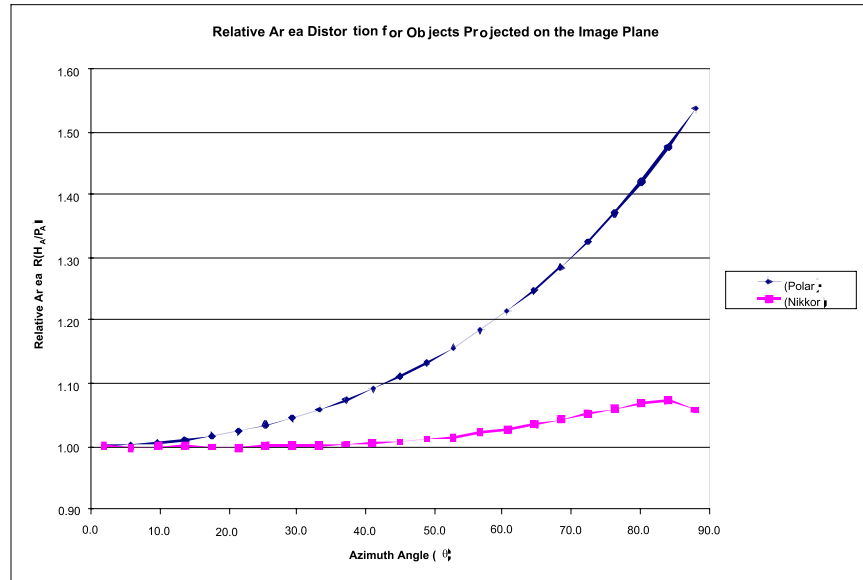


FIGURE B-3. A comparison of relative area distortions for a theoretical polar projection and the Nikkor 8-mm f/2.8 fisheye lens.

B-5 The Effects of Using Incompatible Projection Transformations on the Derivation of Gap Fraction Magnitude and Distribution, Percent Open Sky, and Effective Leaf Area Index (L_e)

Herbert (1987) has already proven through direct measurement and mathematical modeling that small amounts of radial lens distortion will account for significant variation in projected area on the image plane. It is possible, however, to correct for these distortions provided a proper geometric transformation is applied to the image data. Applying an incompatible transformation will not compensate for these distortions, and may, in fact, exaggerate them. A method to quantify the effects of applying a polar projection transformation to an image captured using the Nikkor 8-mm f/2.8 fisheye lens has been developed using standard GIS image statistics functions, a common spreadsheet application, and various hemispherical images produced using the Nikkor fisheye lens.

The theoretical consequence of applying a polar projection transformation to a Nikkor projected image on the magnitude and redistribution of gap fractions was measured by dividing the hemispherical object region into 18 sky segments of equivalent 5° arc. The position of each arc was projected onto the image plane using both the Nikkor and polar transformation functions. Table B-4 summarizes the results of the transformations and the calculated areas for each projected ring segment. Three distinct differences are apparent between the two projections: 1) the radial distance of each projected circle is greater for the Nikkor projection, 2) the interval ring width is uniform for the polar projection and declining for the Nikkor lens, and c) relative differences in projected area occur between transformations and these differences vary strongly with zenith angle. In more specific terms, arcs projected between zenith angle 0° and 65° using the polar transformation have a projected area that is smaller than rings projected using the Nikkor lens. The opposite effect occurs at zenith angles greater than 65° . Projected ring width is approximately equal at 65° , but the radial positions on the image plane are still not coincident.

TABLE B-4. Spatial characteristics of rings projected onto the image plane using a Nikkor and polar projection transformation

Zenith (θ_1)	Zenith (θ_2)	Mid-Pt. (θ)	Percent Area/Sky Interval	P ^{POLAR} Dist. (mm) (Polar (ζ_1))	P ^{POLAR} Dist. (mm) (Polar (ζ_2))	Δ Dist. (mm) (Polar)	P ^{NIKKOR} Dist. (mm) (Nikkor (ζ_1))	P ^{NIKKOR} Dist. (mm) (Nikkor (ζ_2))	Δ Dist. (mm) (Nikkor)	Projected % Area (Polar ($\zeta_2 - \zeta_1$))	Projected % Area (Nikkor ($\zeta_2 - \zeta_1$))	Δ % Area (P/N)
0	5	2.5	0.38	0.00	0.64	0.64	0.00	0.70	0.70	0.34	0.37	0.84
5	10	7.5	1.14	0.64	1.28	0.64	0.70	1.30	0.70	0.93	1.10	0.84
10	15	12.5	1.89	1.28	1.92	0.64	1.30	2.09	0.69	1.54	1.83	0.86
15	20	17.5	2.62	1.92	2.56	0.64	2.09	2.78	0.69	2.16	2.54	0.85
20	25	22.5	3.34	2.56	3.19	0.64	2.78	3.46	0.68	2.78	3.23	0.86
25	30	27.5	4.03	3.19	3.83	0.64	3.46	4.14	0.68	3.40	3.90	0.87
30	35	32.5	4.69	3.83	4.47	0.64	4.14	4.81	0.67	4.01	4.55	0.88
35	40	37.5	5.31	4.47	5.11	0.64	4.81	5.48	0.66	4.63	5.17	0.90
40	45	42.5	5.89	5.11	5.75	0.64	5.48	6.13	0.66	5.25	5.75	0.94
45	50	47.5	6.43	5.75	6.39	0.64	6.13	6.78	0.65	5.86	6.31	0.93
50	55	52.5	6.92	6.39	7.03	0.64	6.78	7.41	0.64	6.48	6.83	0.96
55	60	57.5	7.36	7.03	7.67	0.64	7.41	8.04	0.63	7.10	7.31	0.97
60	65	62.5	7.74	7.67	8.31	0.64	8.04	8.66	0.62	7.72	7.77	0.99
65	70	67.5	8.06	8.31	8.94	0.64	8.66	9.26	0.60	8.33	8.17	1.02
70	75	72.5	8.32	8.94	9.58	0.64	9.26	9.85	0.59	8.96	8.52	1.05
75	80	77.5	8.52	9.58	10.22	0.64	9.85	10.42	0.57	9.57	8.79	1.09
80	85	82.5	8.65	10.22	10.86	0.64	10.42	10.98	0.56	10.19	8.95	1.14
85	90	87.5	8.72	10.86	11.50	0.64	10.98	11.50	0.52	10.80	9.07	1.20

Applying a polar projection to a Nikkor distorted image causes variable effects on the magnitude and distribution of canopy gap fractions. Two general effects may be noted: 1) gap fraction distributions will shift depending on the true angular position of the canopy gaps, and 2) the magnitude of measured gap fractions will change due to the radial redistribution of gaps. Between zenith angles 0° and 65° , the magnitude of gap fractions will be underestimated, on average, by $10\% \pm (5.2\% \text{ SD})$ (min. 1%, max. 16%) if a polar projection is applied to a Nikkor image. The magnitude of this underestimation increases to a

maximum of 16% at a zenith mid-point angle of 2.5°. Gap fractions are equivalent at approximately 65°, but a rapid increase in the overestimation of gap fractions occurs as the zenith angle approaches 90°. A maximum overestimate of 20% in gap fraction magnitude may occur at a zenith mid-point of 87.5°; however, the average overestimate is 10% \pm (7.3% SD) (min. 2%) for zenith angles 65° to 90°.

Errors in gap fraction magnitude and distribution that have been introduced via the incorrect application of a projection transformation may translate into significant inaccuracies in the estimate of percent open sky, L_e , and understory light regime. The degree to which these estimates affect calculations of percent open sky was measured using gap fractions of known magnitude and distribution. A single open sky segment of 5° arc was projected onto the image plane using the Nikkor calibration function. Gap fractions and percent open sky were then calculated using both projection transformations. This process was repeated 18 times at different zenith mid-point angles so that the differences could be measured throughout the full field of view (Table B-5). Results from this experiment show that percent open sky will be overestimated, on average, by 11.97% \pm (6.5% SD) (minimum 0.96%, maximum 18.75%) when gap fractions are distributed between zenith angles 0° to 60°. In contrast, underestimates of percent open sky occur when gap fractions are distributed close to the horizon. On average, this attribute will be underestimated by 8.7% \pm (6.5% SD) (minimum 1.4%, maximum 17.5%) at zenith angles greater than 60°.

TABLE B-5. Measured theoretical differences in percent open sky for a Nikkor image corrected using a polar projection transformation

Zenith (θ_1)	Zenith (θ_2)	Mid-Pt. (θ)	% Sky (Polar)	% Sky (Nikkor)	Relative Diff. (P/N)	% Diff. (P/N)
0	5	2.5	0.45	0.38	1.1875	18.75
5	10	7.5	1.35	1.14	1.1883	18.83
10	15	12.5	2.23	1.89	1.1823	18.23
15	20	17.5	3.07	2.62	1.1696	16.96
20	25	22.5	3.87	3.34	1.1583	15.83
25	30	27.5	4.60	4.03	1.1416	14.16
30	35	32.5	5.27	4.69	1.1236	12.36
35	40	37.5	5.86	5.31	1.1029	10.29
40	45	42.5	6.37	5.89	1.0801	8.01
45	50	47.5	6.80	6.43	1.0580	5.80
50	55	52.5	7.16	6.92	1.0351	3.51
55	60	57.5	7.43	7.36	1.0096	0.96
60	65	62.5	7.63	7.74	0.9858	-1.42
65	70	67.5	7.74	8.06	0.9602	-3.98
70	75	72.5	7.76	8.32	0.9332	-6.68
75	80	77.5	7.70	8.52	0.9043	-9.57
80	85	82.5	7.52	8.65	0.8692	-13.08
85	90	87.5	7.19	8.72	0.8252	-17.48

The theoretical data presented above indicate that the magnitude and direction of error introduced into the calculations of percent open sky are strongly dependent on the gap fraction distribution. In continuous forest canopies of uniform height, the probability of unobstructed sky views decreases proportionally as zenith angles approach 90°. Most gap fraction distributions will therefore be noticeably skewed towards the horizon. As a consequence, polar transformations of Nikkor images will most often produce significant overestimates of percent open sky. Exceptions to this rule can occur on steep slopes or in discontinuous forest canopies where probabilities of unobstructed sky view near the horizon are much higher. In cases like these, less significant differences in estimates of percent open sky will occur between the two different projection transformations.

Twenty-four representative Nikkor images produced in this study (Appendix A) were analyzed for percent open sky and L_e using the appropriate Nikkor calibration function and the theoretical polar projection (Table B-6). Summary data indicate that percent open sky is consistently overestimated, on average, by $8.5\% \pm (1.7\% \text{ SD})$ (minimum 4.9%, maximum 13.5%) when a polar projection transformation is applied to an image produced with the Nikkor fisheye lens. Not surprisingly, significant overestimates of percent sky translate to underestimates of L_e . L_e is underestimated, on average, by $4.3\% \pm (1.8\% \text{ SD})$ (minimum 0.7%, maximum 7.3%). The effect on estimates of understory solar irradiance has not been measured in this study, but it is assumed to be significant due to the potential imprecision in suntrack positioning and distortions in gap fraction distribution and magnitude.

TABLE B-6 Percent open sky and L_e data calculated using a Nikkor calibration and polar projection function

Site ID	% Sky (Nikkor)	L_e (Nikkor)	% Sky (Polar)	L_e (Polar)	% Diff. % Sky (P/N)	% Diff. L_e (P/N)
vws05-6	6.601	3.002	7.192	2.812	8.948	-6.341
kla82-1	2.224	4.013	2.364	3.943	6.277	-1.725
kla83-1	1.921	4.272	2.079	4.157	8.259	-2.690
kla84-3	7.848	2.747	8.541	2.636	8.830	-4.045
kok22-1	8.053	2.820	8.734	2.627	8.462	-6.859
kok23-4	6.912	2.896	7.498	2.784	8.474	-3.881
kok24-5	16.580	1.813	17.398	1.779	4.939	-1.869
nan33-3	8.010	2.676	8.555	2.572	6.798	-3.899
nan34-3	15.460	1.932	16.715	1.792	8.120	-7.275
nan35-4	3.264	3.687	3.512	3.603	7.580	-2.282
nit72-2	4.736	3.376	5.091	3.283	7.495	-2.770
nit73-7	2.927	3.830	3.124	3.804	6.730	-0.681
nit74-6	10.222	3.135	11.602	2.926	13.496	-6.671
ren52-3	4.931	3.474	5.423	3.282	9.975	-5.536
ren53-5	5.782	3.074	6.224	3.013	7.649	-1.981
ren54-3	12.782	2.207	13.956	2.082	9.181	-5.684
rgc62-3	5.359	3.347	5.897	3.166	10.035	-5.417
vwn12-2	6.945	3.109	7.694	2.944	10.785	-5.303
vwn13-3	7.742	2.699	8.414	2.565	8.679	-4.988
vwn15-7	11.375	2.288	12.346	2.178	8.537	-4.808
rgc63-6	8.417	2.691	9.211	2.549	9.431	-5.278
vws02-6	5.185	3.144	5.592	3.056	7.840	-2.784
vws05-3	6.619	2.906	7.231	2.777	9.246	-4.458
vws06-5	11.313	2.299	12.276	2.181	8.517	-5.137

APPENDIX C.

A Model for Estimating Percent Open Sky and L_e Using PAMAP GIS, Microsoft Excel,
and a Modified LI-COR Inc. Algorithm

C-1 Introduction

Any image analysis or GIS software application that supports raster and vector data structures and can perform simple area calculations and extract standard image statistics for defined areas of interest, can be used to measure gap fraction magnitude and distribution. Gap fraction magnitude and distribution are required for indirect estimates of L_e using inversion techniques (Norman and Campbell 1989). A PAMAP GIS application was constructed to import, display, threshold, and analyze 167 hemispherical images, and also to store resultant raw counts of sky and non-sky pixels. Gap fraction, percent open sky, and L_e were subsequently calculated within Microsoft Excel using modified canopy structure equations published in Welles and Norman (1991), LI-COR Inc. (1992), and ter Steege (1993).

C-2 Extraction of Gap Fraction Magnitude and Distribution Data

True-colour (24-bit) graphic image files scanned at 1000 DPI were converted to 8-bit colour depths for translation and import into a native PAMAP raster format (RFL). Image colour depth was reduced using an optimizing method found in Paint Shop Pro Version 3.12 to produce the closest 8-bit approximation of the true-colour value. The altered image was also converted to a RAW raster format so that PAMAP could import the raster data using a standard translation module. A Visual Basic 3.0 program was written to convert a standard 8-bit BMP colour palette into a PAMAP colour display table (CLT) so that the hemispherical image could be viewed in its original colour. An internal PAMAP threshold table was used to classify the image into sky and non-sky pixels.

The image plane was partitioned into 6 equal, 15° intervals of zenith according to the gap fraction inversion method outlined in Welles and Norman (1991) and LI-COR Inc. (1992). The projected position of each arc onto the image surface was determined using a polar projection transformation (ter Steege 1993). The horizontal plane was also divided into 22.5° segments of azimuth starting at 0° north and rotated counter-clockwise through 360° of arc. When photographic film is exposed with the camera looking up, east and west coordinates are opposite to where they occur on a regular paper map depicting some portion of the earth surface, (i.e., if north is at the top of the hemispherical image, east is on the left and west is on the right). This is an important point to remember, since most geographically based mapping and image analysis software systems will assume that north is at the top, and east and west are located on the right and left side, respectively.

Divisions of both the vertical and horizontal plane into equal-interval segments have resulted in 96 distinct areas within the hemispherical object region (Figure C-1). PAMAP image statistic routines were executed so that the number of sky and non-sky pixels could be calculated for each of the unique sky regions. These data were stored in an internal database and referenced to their spatial origin by an alphanumeric identifier. SQL commands were used to search through the database and replace sky pixel attribute values of 0 with the value 1 to avoid computing gap fractions equal to 0. This step is essential, since gap fraction estimates must undergo a natural logarithmic transformation to solve for L_e (Welles and Norman 1991; LI-COR Inc. 1992). The effect of this procedure on calculations of percent open sky is insignificant for high-resolution images (i.e., ≥ 1000 DPI), and could, at maximum, account for an additional 0.086% added to the percent-open-sky estimate. In reality, this error will be in the order of 0.008%.

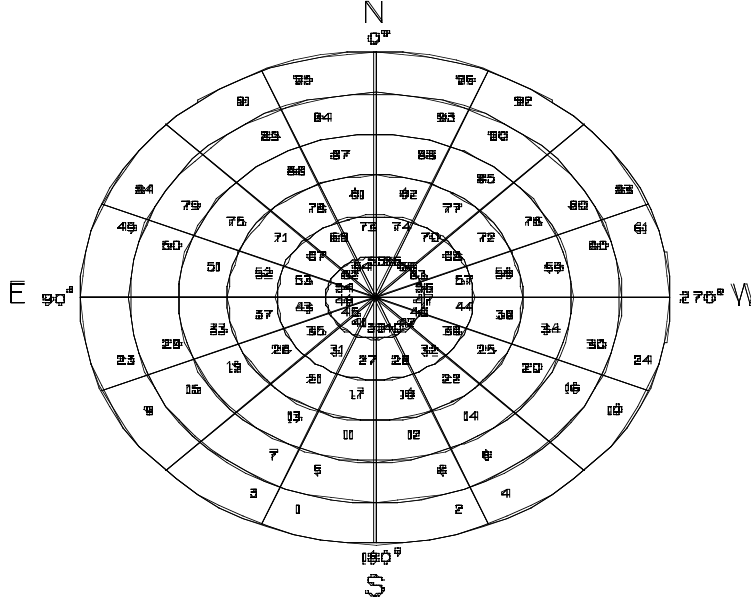


FIGURE C-1. The hemispherical object region was subdivided into 96 distinct sky regions for the purpose of extracting gap fraction data and measuring percent open sky and L_e . Divisions of zenith angle correspond to the angular requirements of the L_e equation published by Welles and Norman (1991).

C-3 Gap Fraction and Percent Open Sky Calculations

Data stored in the PAMAP GIS proprietary database were exported as an ASCII file and imported directly into an intermediate Microsoft Excel spreadsheet. In turn, these data were cut and paste via the Windows clipboard into a final spreadsheet designed to a) calculate gap fractions for each sky region, b) sort input data into an array organized by azimuth and zenith angle, c) determine percent open sky, and d) correct path-length data and calculate L_e . The gap fraction for a sky region located at zenith (θ) and azimuth (α) mid-point angles is measured using the following equation:

$$T(\theta, \alpha) = P_s / (P_s + P_{ns}) \quad (C.1)$$

where $T(\theta, \alpha)$ is the gap fraction estimated for a sky region located at a mid-point zenith angle (θ) and a mid-point azimuth angle (α), P_s is the number of sky pixels contained within the sky region, and P_{ns} is the number of non-sky pixels (i.e., vegetation) counted within the same defined area. Percent-open-sky data were calculated for each cell or region within the array using the following equation:

$$A(\theta, \alpha) = [(\cos(\theta_1) - \cos(\theta_2)) / n] \times T(\theta, \alpha) \times 100\% \quad (C.2)$$

where $A(\theta, \alpha)$ is the portion of the total percent open sky contributed from a sky region located at midpoints (θ, α), θ_1 is the smallest angle of zenith (measured in degrees) which defines the upper boundary of the sky region, θ_2 is the largest angle of zenith (measured in degrees) defining the lower boundary of the sky region, n is the number of divisions of azimuth angle, and $T(\theta, \alpha)$ is the gap fraction within the sky region (θ, α). Percent open sky for the complete hemisphere is calculated by summing all 96 values of $A(\theta, \alpha)$:

$$\%Sky = \sum_{SR=1}^{96} A(\theta, \alpha) \quad (C.3)$$

C-4 Estimation of L_e Using a Standard and Modified LI-COR Inc. Solution

The standard LI-COR Inc. L_e algorithm depends on a fixed path-length geometry (Welles and Norman 1991). On inclined surfaces, path lengths are not fixed but variable, and change with the apparent slope of the ground and canopy surfaces. LI-COR Inc. (1992) has suggested that light measurements should be taken parallel to the slope to maintain a static path-length configuration. This solution was unreasonable for our study because of the following: a) solar irradiance models require input from hemispherical images that have been projected normal to the local zenith, and b) the forest overstory was composed of conifers that are known to have foliage orientations that are not random, but clumped and highly organized. It would be possible to expose two canopy photographs per location; i.e., one photograph for solar irradiance applications and a second reoriented for L_e measurement. There is some potential danger, however, that tilting the camera for L_e measurements might introduce an angular bias into the results that is directly related to site slope and aspect.

As an alternative to tilting the camera, we chose to modify the LI-COR Inc. L_e equation and adjust the path-length geometry according to the apparent slope of the tilted canopy and ground surfaces. The apparent slope (A_s) of an inclined surface can be calculated in any angular direction between the maximum slope and strike of the plane using the following equation:

$$\tan(A_s) = \tan(\alpha) \times \cos(\beta) \quad (C.4)$$

where A_s is the apparent slope measured in degrees, α is the maximum slope of the surface measured in degrees, and β is the angle between the direction of maximum slope (true slope) and apparent slope. The value of apparent slope will vary from 0° along the strike of the plane to a maximum in the direction of true slope (Figure C-2). Apparent slope (A_s) along any bearing relative to true north can be calculated using the equation:

$$\tan(A_s) = \tan(\alpha) \times \cos(\sigma - \varepsilon) \quad (C.5)$$

where α is the maximum or true slope in degrees, σ is the aspect in degrees, and ε is the azimuth angle of a vector for which the apparent slope will be calculated. All computed slope values downslope from the strike of the plane will take on a positive sign, and upslope measures will be negative.

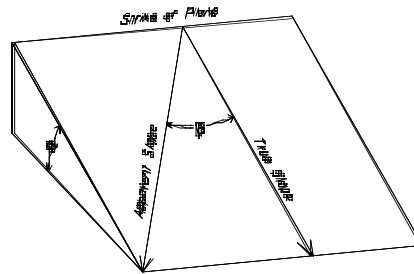


FIGURE C-2. Difference between apparent and maximum slope (true slope) of an inclined surface.

Li-Cor Inc. has proposed the following numerical formula to estimate effective leaf area index (L_e):

$$L_e = -2 \sum_{i=1}^5 \ln(T(\theta_i)) \cos \theta_i w(\theta_i) \quad (C.6)$$

where $T(\theta)$ is the gap fraction measured as the diffuse light intensity below the canopy at view angle θ divided by the diffuse light intensity above the canopy at view angle θ ; $\cos \theta$ is the portion of the extinction coefficient of light transmittance related to path length at view angle θ , and $w(\theta)$ is a constant weighting factor applied to each of the five rings. $T(\theta)$ can be calculated from hemispherical photographs using the methods introduced in section C-2 and Eq. (C.1). On an inclined surface the term $\cos \theta$ varies according to azimuth and apparent view angle. Apparent view (A_v) angles can be derived by subtracting the apparent slope (A_s) from the fixed view angle (θ), (i.e., 7, 23, 38, 53 or 68°):

$$A_v = \theta - A_s \quad (C.7)$$

Finally, by substituting A_v for θ in the term $\cos \theta$ in Eq. (C.6) it is possible to calculate $L_{e(SD)}$ for any defined sky direction on a surface that is inclined according to a known slope and aspect and where the camera has been aligned perpendicular to the local zenith:

$$L_{e(SD)} = -2 \sum_{i=1}^5 \ln(T(\theta_i)) \cos A_{v_i} w(\theta_i) \quad (C.8)$$

$L_{e(SD)}$ is the effective leaf area index calculated for any one of the 16, 22.5° divisions of azimuth. To measure $L_{e(SD)}$ for the complete hemispherical object region, all 16 contributing $L_{e(SD)}$ values must be averaged throughout 360° of azimuth:

$$L_e = \frac{\sum_{SD=1}^n L_{e(SD)}}{n} \quad (C.9)$$

Figure C-3 shows an example of the distribution of $L_{e(SD)}$ calculated for site KLA82-1 located on the southwest side of Vancouver Island. The standard LI-COR Inc. L_e equation ignores the heterogeneous distribution of canopy gaps and therefore L_e by averaging gap fraction and path length over 360° of azimuth. The modified LI-COR Inc. L_e model is capable of recalculating $L_{e(SD)}$ and L_e for any angle of slope and aspect. Sites that have slopes greater than 15° but less 30° will require omission of the last ring (60-75°) from the L_e calculations, since the camera would have been looking directly into the hillslope at this interval of zenith. The number of additional rings that should be excluded from the analysis is a function of slope severity. Figure C-4 summarizes the distributions of $L_{e(SD)}$, corrected and uncorrected, for ground and canopy surface inclination at site KLA82-1. The slope and aspect for this location is 19° and 135°, respectively. These distribution data suggest that $L_{e(SD)}$ will be over and underestimated in the down and upslope directions, respectively, if changing path-length geometry is not factored into the L_e calculations. The magnitude of these differences depends directly on the severity of the slope and the distribution of canopy gaps.

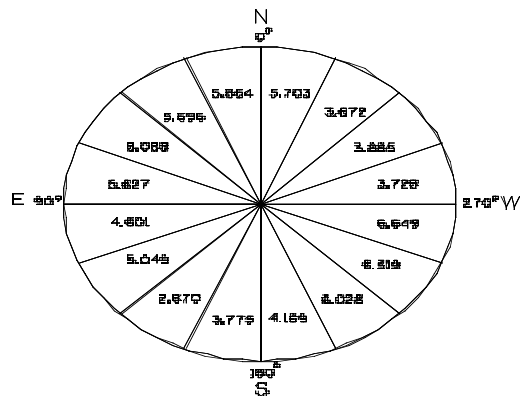


FIGURE C-3. The modified LI-COR Inc. L_e equation is used on inclined sites where the path-length geometry varies according to apparent slope of the ground and canopy surfaces. By adjusting path length for defined segments of azimuth, $L_{e(SD)}$ can be calculated for 16 unique sky directions.

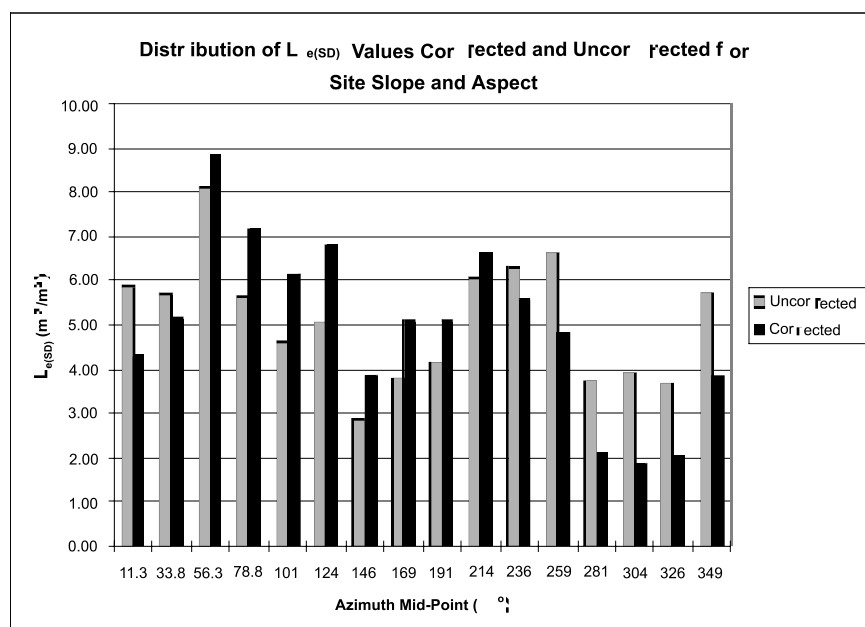


FIGURE C-4. The distribution of $L_{e(SD)}$ corrected and uncorrected for ground and canopy surface inclination. $L_{e(SD)}$ will be over and underestimated in the down and upslope directions, respectively, if path lengths are not adjusted according to the appropriate apparent view angle.

APPENDIX D.

Sample Design of Photo Archive Database for Southern Vancouver Island
Chronosequence Study

<u>Roll #</u>	<u>Site_id</u>	<u>Subplot_id</u>	<u>Negative_id</u>	<u>Roll_id</u>	<u>Aperture</u>	<u>Speed</u>	<u>Time</u>	<u>Date</u>	<u>Scanned</u>	<u>Image Filename</u>
1	vws06	4	7	1238	f8	250	11:51	8-Aug-95	FALSE	
1	vws06	4	8	1238	f8	500	11:52	8-Aug-95	FALSE	
1	vws06	4	9	1238	f8	250	11:53	8-Aug-95	FALSE	
1	vws06	4	10	1238	f8	1000	11:53	8-Aug-95	TRUE	vws06-4.bmp
1	vws06	4	11	1238	f8	125	11:55	8-Aug-95	FALSE	
1	vws06	3	12	1238	f8	1000	12:17	8-Aug-95	FALSE	
1	vws06	3	13	1238	f8	500	12:18	8-Aug-95	FALSE	
1	vws06	3	14	1238	f8	250	12:19	8-Aug-95	FALSE	
1	vws06	3	15	1238	f8	125	12:21	8-Aug-95	TRUE	vws06-3.bmp
1	vws06	3	16	1238	f8	60	12:21	8-Aug-95	FALSE	
1	vws06	7	17	1238	f8	1000	12:33	8-Aug-95	FALSE	
1	vws06	7	18	1238	f8	500	12:34	8-Aug-95	FALSE	
1	vws06	7	19	1238	f8	250	12:34	8-Aug-95	FALSE	
1	vws06	7	20	1238	f8	125	12:35	8-Aug-95	TRUE	vws06-7.bmp
1	vws06	7	21	1238	f8	60	12:35	8-Aug-95	FALSE	
1	vws06	2	22	1238	f8	1000	12:48	8-Aug-95	FALSE	
1	vws06	2	23	1238	f8	500	12:49	8-Aug-95	FALSE	
1	vws06	2	24	1238	f8	250	12:49	8-Aug-95	FALSE	
1	vws06	2	25	1238	f8	125	12:50	8-Aug-95	TRUE	vws06-2.bmp
1	vws06	2	26	1238	f8	60	12:51	8-Aug-95	FALSE	
1	vws06	5	27	1238	f8	1000	13:00	8-Aug-95	FALSE	
1	vws06	5	28	1238	f8	500	13:00	8-Aug-95	FALSE	
1	vws06	5	29	1238	f8	250	13:00	8-Aug-95	TRUE	vws06-5.bmp
1	vws06	5	30	1238	f8	125	13:01	8-Aug-95	FALSE	
1	vws06	5	31	1238	f8	60	13:02	8-Aug-95	FALSE	
1	vws06	1	32	1238	f8	1000	13:11	8-Aug-95	FALSE	
1	vws06	1	33	1238	f8	500	13:12	8-Aug-95	FALSE	
1	vws06	1	34	1238	f8	250	13:12	8-Aug-95	TRUE	vws06-1.bmp
1	vws06	1	35	1238	f8	125	13:13	8-Aug-95	FALSE	
1	vws06	1	36	1238	f8	60	13:14	8-Aug-95	FALSE	
2	vws06	6	0	1239	f8	1000	13:36	8-Aug-95	FALSE	
2	vws06	6	1	1239	f8	500	13:37	8-Aug-95	FALSE	
2	vws06	6	2	1239	f8	250	13:38	8-Aug-95	FALSE	
2	vws06	6	3	1239	f8	125	13:38	8-Aug-95	TRUE	vws06-6.bmp
2	vws06	6	4	1239	f8	60	13:39	8-Aug-95	FALSE	
2	vws02	4	5	1239	f8	1000	10:23	9-Aug-95	FALSE	
2	vws02	4	6	1239	f8	1000	10:29	9-Aug-95	FALSE	
2	vws02	4	7	1239	f8	500	10:29	9-Aug-95	FALSE	
2	vws02	4	8	1239	f8	250	10:30	9-Aug-95	FALSE	
2	vws02	4	9	1239	f8	125	10:30	9-Aug-95	TRUE	vws02-4.bmp
2	vws02	4	10	1239	f8	60	10:30	9-Aug-95	FALSE	
2	vws02	5	11	1239	f8	1000	10:39	9-Aug-95	FALSE	
2	vws02	5	12	1239	f8	500	10:40	9-Aug-95	FALSE	
2	vws02	5	13	1239	f8	250	10:41	9-Aug-95	FALSE	
2	vws02	5	14	1239	f8	125	10:41	9-Aug-95	TRUE	vws02-5.bmp
2	vws02	5	15	1239	f8	60	10:42	9-Aug-95	FALSE	
2	vws02	5	16	1239	f8	1000	10:57	9-Aug-95	FALSE	
2	vws02	1	17	1239	f8	500	10:58	9-Aug-95	FALSE	
2	vws02	1	18	1239	f8	250	10:59	9-Aug-95	FALSE	
2	vws06	1	19	1239	f8	125	10:59	9-Aug-95	FALSE	
2	vws02	1	20	1239	f8	60	11:00	9-Aug-95	TRUE	vws02-1.bmp
2	vws02	2	21	1239	f8	1000	11:11	9-Aug-95	FALSE	
2	vws02	2	22	1239	f8	500	11:12	9-Aug-95	FALSE	
2	vws02	2	23	1239	f8	250	11:12	9-Aug-95	FALSE	
2	vws02	2	24	1239	f8	125	11:13	9-Aug-95	TRUE	vws02-2.bmp
2	vws02	2	25	1239	f8	60	11:13	9-Aug-95	FALSE	
2	vws02	7	26	1239	f8	1000	11:25	9-Aug-95	FALSE	
2	vws02	7	27	1239	f8	500	11:25	9-Aug-95	FALSE	
2	vws02	7	28	1239	f8	250	11:25	9-Aug-95	TRUE	vws02-7.bmp
2	vws02	7	29	1239	f8	125	11:26	9-Aug-95	FALSE	

APPENDIX E.

Site Characteristics Database for Southern Vancouver Island
Chronosequence Study

Chronosequence Site		Chr. No.	Plot Est. No.	Plot No.	Zone	East	North	Longitude	Latitude	Elevation (Metres)	Slope (Degrees)	Aspect (Degrees)	Sere	Age
Victoria Watershed South (VWS)		1	2	2	10	452340	53788	122.32.55				30	I	
			3a	5	10	451100	53796	122.32.45				15	M	
			4	6	10	452560	53782	122.32.53	45.35.44.5	555	22	30	O	245
Victoria Watershed North (VWN)		2	2	12	10	447259	53870	122.42.40				60	I	
			3	13	10	446402	53872	122.44.09				55	M	
			4	15	10	446920	53846	122.43.17	45.35.35.5	455	22	20	O	316
Koksilah (KOK)		3	2	22	10	443951	53897	122.46.10				170	I	
			3	23	10	444927	53892	122.44.50				10	M	
			4	24	10	444684	53894	122.45.50	45.35.35.5	555	22	180	O	288
Nanaimo River (NAN)		4	3	33	10	414703	54330	124.00.45				190	M	
			4	34	10	414277	54333	124.10.40				10	O	330
			-	35	10	415957	54340	124.10.20	45.35.35.5	115		138	I	
Renfrew (REN)		6	2	52	10	399387	53793	124.22.22		45		50	I	
			3	53	10	397570	53787	124.22.22		45		40	M	
			4	54	10	397642	53770	124.22.21	45.35.35.5	525		270	O	255
Red/Granite Creek (RGC)		7	2	62	10	404265	53805	124.17.43		15		60	I	
			3	63	10	404804	53833	124.17.20		15		85	M	176
			5	64	10	409891	53811	124.13.07	45.35.35.5	525	45	360	O	
Nitnat (NIT)		8	2	72	10	379914	54111	124.38.10		15		35	I	
			3	73	10	379268	54105	124.38.39				10	M	
			4	74	10	379740	54097	124.38.22	45.35.35.5	525		245	O	270
Klanawa (KLA)		9	2	82	10	364574	54134	124.50.09		15		135	I	
			3	83	10	363984	54093	124.50.27		15		30	M	
			4	84	10	364181	54090	124.50.27	45.35.35.5	115		340	O	435

APPENDIX F.

HEMIPHOT and PAMAP GIS Derived Percent Open Sky, L_e , and PPFD Data for
Southern Vancouver Island Chronosequence Study

Site ID	HEMIPHOT	PAMAF	Above Canopy (mol/m ² /day)			Below Canopy (mol/m ² /day)			% Direct	% Diffuse	% Total	HEMIPHOT	PAMAF
	% Sky	% Sky	Direct	Diffuse	Total	Direct	Diffuse	Total				L _e	L _e
KLA82-1	2.1	2.4	25.59	12.79	38.38	0.92	0.35	1.27	3.60	2.74	3.31	4.13	3.94
KLA82-2	2.0	2.6	25.59	12.79	38.38	1.44	0.37	1.81	5.63	2.89	4.72	4.46	4.01
KLA82-3	1.9	1.9	25.59	12.79	38.38	1.17	0.37	1.54	4.57	2.89	4.01	4.52	4.32
KLA82-4	1.3	1.7	25.59	12.79	38.38	1.50	0.27	1.77	5.86	2.11	4.61	5.33	4.77
KLA82-5	3.1	3.1	25.59	12.79	38.38	1.24	0.55	1.79	4.85	4.30	4.66	3.71	3.65
KLA82-6	1.3	1.7	25.59	12.79	38.38	0.62	0.21	0.83	2.42	1.64	2.16	4.98	4.55
KLA82-7	<u>2.2</u>	<u>2.1</u>	<u>25.59</u>	<u>12.79</u>	<u>38.38</u>	<u>0.50</u>	<u>0.45</u>	<u>0.95</u>	<u>1.95</u>	<u>3.52</u>	<u>2.48</u>	<u>4.61</u>	<u>4.54</u>
Min.	1.3	1.7	25.59	12.79	38.38	0.50	0.21	0.83	1.95	1.64	2.16	3.71	3.65
Max.	3.1	3.1	25.59	12.79	38.38	1.50	0.55	1.81	5.86	4.30	4.72	5.33	4.77
Mean	2.0	2.2	25.59	12.79	38.38	1.06	0.37	1.42	4.13	2.87	3.71	4.53	4.25
Median	2.0	2.1	25.59	12.79	38.38	1.17	0.37	1.54	4.57	2.89	4.01	4.52	4.32
Stdev.	0.6	0.5	0.00	0.00	0.00	0.39	0.11	0.41	1.52	0.87	1.07	0.53	0.40
KLA83-1	2.0	2.1	25.36	12.68	38.04	0.65	0.36	1.01	2.56	2.84	2.66	4.29	4.16
KLA83-2	2.2	2.8	25.36	12.68	38.04	0.67	0.39	1.06	2.64	3.08	2.79	4.21	3.88
KLA83-3	1.6	1.6	25.36	12.68	38.04	0.81	0.31	1.12	3.19	2.44	2.94	4.64	4.62
KLA83-4	1.7	2.2	25.36	12.68	38.04	0.92	0.31	1.23	3.63	2.44	3.23	4.64	4.21
KLA83-5	2.9	2.9	25.36	12.68	38.04	0.59	0.58	1.17	2.33	4.57	3.08	4.05	3.95
KLA83-6	3.9	3.7	25.36	12.68	38.04	1.67	0.86	2.53	6.59	6.78	6.65	4.59	4.24
KLA83-7	<u>3.8</u>	<u>4.0</u>	<u>25.36</u>	<u>12.68</u>	<u>38.04</u>	<u>0.46</u>	<u>0.81</u>	<u>1.27</u>	<u>1.81</u>	<u>6.39</u>	<u>3.34</u>	<u>4.09</u>	<u>3.80</u>
Min.	1.6	1.6	25.36	12.68	38.04	0.46	0.31	1.01	1.81	2.44	2.66	4.05	3.80
Max.	3.9	4.0	25.36	12.68	38.04	1.67	0.86	2.53	6.59	6.78	6.65	4.64	4.62
Mean	2.6	2.8	25.36	12.68	38.04	0.82	0.52	1.34	3.25	4.08	3.53	4.36	4.12
Median	2.2	2.8	25.36	12.68	38.04	0.67	0.39	1.17	2.64	3.08	3.08	4.29	4.16
Stdev.	1.0	0.9	0.00	0.00	0.00	0.40	0.24	0.53	1.58	1.86	1.40	0.26	0.28
KLA84-1	6.3	5.8	25.43	12.72	38.15	0.71	1.09	1.80	2.79	8.57	4.72	2.98	3.05
KLA84-2	9.1	9.1	25.43	12.72	38.15	3.24	1.96	5.20	12.74	15.41	13.63	3.40	3.23
KLA84-3	8.0	8.5	25.43	12.72	38.15	1.25	1.49	2.74	4.92	11.71	7.18	2.76	2.64
KLA84-4	4.9	5.1	25.43	12.72	38.15	1.95	0.87	2.82	7.67	6.84	7.39	3.35	3.22
KLA84-5	4.0	4.3	25.43	12.72	38.15	2.19	0.79	2.98	8.61	6.21	7.81	3.86	3.83
KLA84-6	4.9	5.5	25.43	12.72	38.15	0.95	0.97	1.92	3.74	7.63	5.03	3.54	3.27
KLA84-7	<u>4.6</u>	<u>5.1</u>	<u>25.43</u>	<u>12.72</u>	<u>38.15</u>	<u>1.67</u>	<u>0.95</u>	<u>2.62</u>	<u>6.57</u>	<u>7.47</u>	<u>6.87</u>	<u>3.80</u>	<u>3.50</u>
Min.	4.0	4.3	25.43	12.72	38.15	0.71	0.79	1.80	2.79	6.21	4.72	2.76	2.64
Max.	9.1	9.1	25.43	12.72	38.15	3.24	1.96	5.20	12.74	15.41	13.63	3.86	3.83
Mean	6.0	6.2	25.43	12.72	38.15	1.71	1.16	2.87	6.72	9.12	7.52	3.38	3.25
Median	4.9	5.5	25.43	12.72	38.15	1.67	0.97	2.74	6.57	7.63	7.18	3.40	3.23
Stdev.	1.9	1.8	0.00	0.00	0.00	0.86	0.42	1.12	3.37	3.30	2.94	0.40	0.37

Site ID	HEMIPHOT	PAMAF	Above Canopy (mol/m ² /day)			Below Canopy (mol/m ² /day)						HEMIPHOT	PAMAF
	% Sky	% Sky	Direct	Diffuse	Total	Direct	Diffuse	Total	% Direct	% Diffuse	% Total	L _e	L _e
KOK22-1	8.1	8.7	26.81	13.40	40.21	2.82	1.54	4.36	10.52	11.49	10.84	2.75	2.62
KOK22-2	8.4	8.6	26.81	13.40	40.21	4.85	1.83	6.68	18.09	13.66	16.61	3.41	2.85
KOK22-3	6.7	6.5	26.81	13.40	40.21	4.09	1.40	5.49	15.26	10.45	13.65	3.33	3.15
KOK22-4	4.4	5.1	26.81	13.40	40.21	2.91	0.90	3.81	10.85	6.72	9.48	3.81	3.47
KOK22-5	12.5	12.7	26.81	13.40	40.21	3.48	2.76	6.24	12.98	20.60	15.52	3.00	2.76
KOK22-6	5.1	5.0	26.81	13.40	40.21	2.66	1.17	3.83	9.92	8.73	9.52	4.12	4.08
KOK22-7	<u>7.7</u>	<u>8.0</u>	<u>26.81</u>	<u>13.40</u>	<u>40.21</u>	<u>3.35</u>	<u>1.78</u>	<u>5.13</u>	<u>12.50</u>	<u>13.28</u>	<u>12.76</u>	<u>3.99</u>	<u>3.58</u>
Min.	4.4	5.0	26.81	13.40	40.21	2.66	0.90	3.81	9.92	6.72	9.48	2.75	2.62
Max.	12.5	12.7	26.81	13.40	40.21	4.85	2.76	6.68	18.09	20.60	16.61	4.12	4.08
Mean	7.6	7.8	26.81	13.40	40.21	3.45	1.63	5.08	12.87	12.13	12.63	3.49	3.22
Median	7.7	8.0	26.81	13.40	40.21	3.35	1.54	5.13	12.50	11.49	12.76	3.41	3.15
Stdev.	2.7	2.7	0.00	0.00	0.00	0.78	0.60	1.14	2.93	4.46	2.83	0.51	0.53
KOK23-1	9.5	10.0	26.54	13.27	39.81	4.18	1.92	6.10	15.75	14.47	15.32	2.83	2.65
KOK23-2	5.6	6.4	26.54	13.27	39.81	3.38	1.14	4.52	12.74	8.59	11.35	3.34	3.02
KOK23-3	7.3	7.2	26.54	13.27	39.81	2.84	1.51	4.35	10.70	11.38	10.93	3.19	3.10
KOK23-4	6.7	7.5	26.54	13.27	39.81	4.17	1.30	5.47	15.71	9.80	13.74	2.98	2.78
KOK23-5	5.4	6.2	26.54	13.27	39.81	3.31	1.02	4.33	12.47	7.69	10.88	3.26	3.00
KOK23-6	11.5	10.5	26.54	13.27	39.81	5.57	2.37	7.94	20.99	17.86	19.94	2.55	2.57
KOK23-7	<u>8.8</u>	<u>9.1</u>	<u>26.54</u>	<u>13.27</u>	<u>39.81</u>	<u>4.88</u>	<u>1.86</u>	<u>6.74</u>	<u>18.39</u>	<u>14.02</u>	<u>16.93</u>	<u>3.21</u>	<u>2.76</u>
Min.	5.4	6.2	26.54	13.27	39.81	2.84	1.02	4.33	10.70	7.69	10.88	2.55	2.57
Max.	11.5	10.5	26.54	13.27	39.81	5.57	2.37	7.94	20.99	17.86	19.94	3.34	3.10
Mean	7.8	8.1	26.54	13.27	39.81	4.05	1.59	5.64	15.25	11.97	14.16	3.05	2.84
Median	7.3	7.5	26.54	13.27	39.81	4.17	1.51	5.47	15.71	11.38	13.74	3.19	2.78
Stdev.	2.2	1.8	0.00	0.00	0.00	0.96	0.48	1.38	3.60	3.65	3.46	0.28	0.20
KOK24-1	14.3	15.0	26.63	13.31	39.94	7.12	2.55	9.67	26.74	19.16	24.21	2.04	1.94
KOK24-2	11.8	11.4	26.63	13.31	39.94	5.50	2.25	7.75	20.65	16.90	19.40	2.29	2.27
KOK24-3	15.4	16.8	26.63	13.31	39.94	8.54	2.78	11.32	32.07	20.89	28.34	1.94	1.80
KOK24-4	10.1	11.6	26.63	13.31	39.94	5.49	1.89	7.38	20.62	14.20	18.48	2.52	2.29
KOK24-5	16.1	17.4	26.63	13.31	39.94	5.38	2.68	8.06	20.20	20.14	20.18	1.91	1.77
KOK24-6	13.4	14.2	26.63	13.31	39.94	5.86	2.53	8.39	22.01	19.01	21.01	2.19	2.03
KOK24-7	<u>11.9</u>	<u>12.1</u>	<u>26.63</u>	<u>13.31</u>	<u>39.94</u>	<u>6.90</u>	<u>1.94</u>	<u>8.84</u>	<u>25.91</u>	<u>14.58</u>	<u>22.13</u>	<u>2.17</u>	<u>2.15</u>
Min.	10.1	11.4	26.63	13.31	39.94	5.38	1.89	7.38	20.20	14.20	18.48	1.91	1.77
Max.	16.1	17.4	26.63	13.31	39.94	8.54	2.78	11.32	32.07	20.89	28.34	2.52	2.29
Mean	13.3	14.1	26.63	13.31	39.94	6.40	2.37	8.77	24.03	17.84	21.97	2.15	2.04
Median	13.4	14.2	26.63	13.31	39.94	5.86	2.53	8.39	22.01	19.01	21.01	2.17	2.03
Stdev.	2.1	2.5	0.00	0.00	0.00	1.18	0.35	1.35	4.42	2.66	3.38	0.21	0.21

Site ID	HEMIPHOT	PAMAF	Above Canopy (mol/m ² /day)			Below Canopy (mol/m ² /day)			% Direct	% Diffuse	% Total	HEMIPHOT	PAMAF
	% Sky	% Sky	Direct	Diffuse	Total	Direct	Diffuse	Total				L _e	L _e
NAN33-1	5.7	5.8	25.90	12.95	38.85	3.26	1.15	4.41	12.59	8.88	11.35	3.26	3.15
NAN33-2	9.5	9.3	25.90	12.95	38.85	5.12	1.91	7.03	19.77	14.75	18.10	2.77	2.73
NAN33-3	7.6	8.6	25.90	12.95	38.85	3.34	1.31	4.65	12.90	10.12	11.97	2.84	2.59
NAN33-4	18.1	18.3	25.90	12.95	38.85	8.09	3.73	11.82	31.24	28.80	30.42	1.97	1.86
NAN33-5	6.3	7.0	25.90	12.95	38.85	1.46	1.15	2.61	5.64	8.88	6.72	3.23	2.98
NAN33-6	8.3	8.7	25.90	12.95	38.85	3.09	1.76	4.85	11.93	13.59	12.48	3.20	2.86
NAN33-7	11.7	12.3	25.90	12.95	38.85	3.40	2.53	5.93	13.13	19.54	15.26	2.80	2.61
Min.	5.7	5.8	25.90	12.95	38.85	1.46	1.15	2.61	5.64	8.88	6.72	1.97	1.86
Max.	18.1	18.3	25.90	12.95	38.85	8.09	3.73	11.82	31.24	28.80	30.42	3.26	3.15
Mean	9.6	10.0	25.90	12.95	38.85	3.97	1.93	5.90	15.31	14.94	15.19	2.87	2.68
Median	8.3	8.7	25.90	12.95	38.85	3.34	1.76	4.85	12.90	13.59	12.48	2.84	2.73
Stdev.	4.3	4.2	0.00	0.00	0.00	2.11	0.93	2.94	8.13	7.21	7.58	0.45	0.41
NAN34-1	22.4	22.1	25.91	12.95	38.86	7.52	4.15	11.67	29.02	32.05	30.03	1.55	1.53
NAN34-2	2.2	2.9	25.91	12.95	38.86	1.19	0.40	1.59	4.59	3.09	4.09	4.44	3.97
NAN34-3	17.0	16.7	25.91	12.95	38.86	7.66	3.09	10.75	29.56	23.86	27.66	1.81	1.80
NAN34-4	8.2	8.4	25.91	12.95	38.86	1.96	1.85	3.81	7.56	14.29	9.80	3.44	3.33
NAN34-5	7.7	8.0	25.91	12.95	38.86	0.92	1.58	2.50	3.55	12.20	6.43	3.22	3.00
NAN34-6	10.9	10.4	25.91	12.95	38.86	4.45	2.29	6.74	17.17	17.68	17.34	2.70	2.64
NAN34-7	7.9	8.0	25.91	12.95	38.86	3.61	1.75	5.36	13.93	13.51	13.79	3.49	3.24
Min.	2.2	2.9	25.91	12.95	38.86	0.92	0.40	1.59	3.55	3.09	4.09	1.55	1.53
Max.	22.4	22.1	25.91	12.95	38.86	7.66	4.15	11.67	29.56	32.05	30.03	4.44	3.97
Mean	10.9	10.9	25.91	12.95	38.86	3.90	2.16	6.06	15.06	16.67	15.59	2.95	2.79
Median	8.2	8.4	25.91	12.95	38.86	3.61	1.85	5.36	13.93	14.29	13.79	3.22	3.00
Stdev.	6.7	6.4	0.00	0.00	0.00	2.82	1.19	3.92	10.87	9.21	10.08	1.01	0.87
NAN35-1	3.8	4.2	25.93	12.97	38.90	1.43	0.76	2.19	5.51	5.86	5.63	3.80	3.58
NAN35-2	6.5	7.1	25.93	12.97	38.90	2.92	1.40	4.32	11.26	10.79	11.11	3.55	3.23
NAN35-3	6.2	6.7	25.93	12.97	38.90	3.22	1.35	4.57	12.42	10.41	11.75	3.89	3.50
NAN35-4	2.8	3.5	25.93	12.97	38.90	1.47	0.50	1.97	5.67	3.86	5.06	3.96	3.60
NAN35-5	4.2	4.1	25.93	12.97	38.90	1.66	0.77	2.43	6.40	5.94	6.25	3.43	3.40
NAN35-6	4.5	5.3	25.93	12.97	38.90	3.56	0.77	4.33	13.73	5.94	11.13	3.46	3.17
NAN35-7	8.2	8.7	25.93	12.97	38.90	2.96	1.78	4.74	11.42	13.72	12.19	3.12	2.91
Min.	2.8	3.5	25.93	12.97	38.90	1.43	0.50	1.97	5.51	3.86	5.06	3.12	2.91
Max.	8.2	8.7	25.93	12.97	38.90	3.56	1.78	4.74	13.73	13.72	12.19	3.96	3.60
Mean	5.2	5.7	25.93	12.97	38.90	2.46	1.05	3.51	9.49	8.07	9.02	3.60	3.34
Median	4.5	5.3	25.93	12.97	38.90	2.92	0.77	4.32	11.26	5.94	11.11	3.55	3.40
Stdev.	1.9	1.9	0.00	0.00	0.00	0.91	0.46	1.24	3.50	3.57	3.19	0.30	0.25

Site ID	HEMIPHOT	PAMAF	Above Canopy (mol/m ² /day)			Below Canopy (mol/m ² /day)			% Direct	% Diffuse	% Total	HEMIPHOT	PAMAF
	% Sky	% Sky	Direct	Diffuse	Total	Direct	Diffuse	Total				L _e	L _e
NIT72-1	4.7	5.4	25.50	12.75	38.25	2.15	0.90	3.05	8.43	7.06	7.97	3.38	3.15
NIT72-2	4.7	5.1	25.50	12.75	38.25	2.23	0.83	3.06	8.75	6.51	8.00	3.50	3.28
NIT72-3	3.2	3.8	25.50	12.75	38.25	1.78	0.52	2.30	6.98	4.08	6.01	3.72	3.50
NIT72-4	4.2	3.8	25.50	12.75	38.25	2.35	0.76	3.11	9.22	5.96	8.13	3.74	3.70
NIT72-5	5.5	5.9	25.50	12.75	38.25	2.19	0.92	3.11	8.59	7.22	8.13	3.11	2.96
NIT72-6	7.9	7.5	25.50	12.75	38.25	4.34	1.39	5.73	17.02	10.90	14.98	2.72	2.78
NIT72-7	<u>3.4</u>	<u>3.4</u>	<u>25.50</u>	<u>12.75</u>	<u>38.25</u>	<u>2.25</u>	<u>0.66</u>	<u>2.91</u>	<u>8.82</u>	<u>5.18</u>	<u>7.61</u>	<u>3.81</u>	<u>3.74</u>
Min.	3.2	3.4	25.50	12.75	38.25	1.78	0.52	2.30	6.98	4.08	6.01	2.72	2.78
Max.	7.9	7.5	25.50	12.75	38.25	4.34	1.39	5.73	17.02	10.90	14.98	3.81	3.74
Mean	4.8	5.0	25.50	12.75	38.25	2.47	0.85	3.32	9.69	6.70	8.69	3.43	3.30
Median	4.7	5.1	25.50	12.75	38.25	2.23	0.83	3.06	8.75	6.51	8.00	3.50	3.28
Stdev.	1.6	1.5	0.00	0.00	0.00	0.84	0.27	1.10	3.31	2.15	2.87	0.40	0.37
NIT73-1	4.2	5.2	25.27	12.64	37.91	1.30	0.66	1.96	5.14	5.22	5.17	3.38	3.09
NIT73-2	2.9	3.8	25.27	12.64	37.91	0.86	0.44	1.30	3.40	3.48	3.43	3.81	3.46
NIT73-3	2.5	3.3	25.27	12.64	37.91	0.79	0.39	1.18	3.13	3.09	3.11	4.05	3.69
NIT73-5	3.9	3.8	25.27	12.64	37.91	0.29	0.75	1.04	1.15	5.93	2.74	3.78	3.67
NIT73-6	2.5	3.4	25.27	12.64	37.91	0.80	0.43	1.23	3.17	3.40	3.24	4.06	3.60
NIT73-7	<u>2.3</u>	<u>3.1</u>	<u>25.27</u>	<u>12.64</u>	<u>37.91</u>	<u>0.93</u>	<u>0.39</u>	<u>1.32</u>	<u>3.68</u>	<u>3.09</u>	<u>3.48</u>	<u>4.20</u>	<u>3.85</u>
Min.	2.3	3.1	25.27	12.64	37.91	0.29	0.39	1.04	1.15	3.09	2.74	3.38	3.1
Max.	4.2	5.2	25.27	12.64	37.91	1.30	0.75	1.96	5.14	5.93	5.17	4.20	3.9
Mean	3.1	3.8	25.27	12.64	37.91	0.83	0.51	1.34	3.28	4.03	3.53	3.88	3.6
Median	2.7	3.6	25.27	12.64	37.91	0.83	0.44	1.27	3.28	3.44	3.34	3.93	3.6
Stdev.	0.8	0.8	0.00	0.00	0.00	0.32	0.16	0.32	1.28	1.23	0.85	0.29	0.3
NIT74-1	5.2	5.3	25.81	12.91	38.72	1.22	1.00	2.22	4.73	7.75	5.73	3.32	3.24
NIT74-2	7.9	8.0	25.81	12.91	38.72	0.62	1.63	2.25	2.40	12.63	5.81	3.22	2.95
NIT74-3	6.8	7.1	25.81	12.91	38.72	3.63	1.33	4.96	14.06	10.30	12.81	2.95	2.84
NIT74-4	8.8	8.7	25.81	12.91	38.72	2.27	1.58	3.85	8.80	12.24	9.94	2.60	2.54
NIT74-5	14.5	14.4	25.81	12.91	38.72	2.97	2.91	5.88	11.51	22.54	15.19	2.24	2.16
NIT74-6	11.6	11.6	25.81	12.91	38.72	4.90	2.54	7.44	18.98	19.67	19.21	3.05	2.89
NIT74-7	<u>4.4</u>	<u>5.1</u>	<u>25.81</u>	<u>12.91</u>	<u>38.72</u>	<u>2.30</u>	<u>0.82</u>	<u>3.12</u>	<u>8.91</u>	<u>6.35</u>	<u>8.06</u>	<u>3.51</u>	<u>3.27</u>
Min.	4.4	5.1	25.81	12.91	38.72	0.62	0.82	2.22	2.40	6.35	5.73	2.24	2.16
Max.	14.5	14.4	25.81	12.91	38.72	4.90	2.91	7.44	18.98	22.54	19.21	3.51	3.27
Mean	8.5	8.6	25.81	12.91	38.72	2.56	1.69	4.25	9.91	13.07	10.97	2.98	2.84
Median	7.9	8.0	25.81	12.91	38.72	2.30	1.58	3.85	8.91	12.24	9.94	3.05	2.89
Stdev.	3.6	3.4	0.00	0.00	0.00	1.44	0.77	1.95	5.59	5.99	5.04	0.44	0.39

Site ID	HEMIPHOT	PAMAF	Above Canopy (mol/m ² /day)			Below Canopy (mol/m ² /day)			% Direct	% Diffuse	% Total	HEMIPHOT	PAMAF
	% Sky	% Sky	Direct	Diffuse	Total	Direct	Diffuse	Total				L _e	L _e
REN52-1	7.5	8.3	25.58	12.79	38.37	0.88	1.45	2.33	3.44	11.34	6.07	2.93	2.65
REN52-2	4.7	4.6	25.58	12.79	38.37	0.49	0.90	1.39	1.92	7.04	3.62	3.38	3.32
REN52-3	4.5	5.4	25.58	12.79	38.37	0.46	0.89	1.35	1.80	6.96	3.52	3.74	3.27
REN52-4	6.3	7.2	25.58	12.79	38.37	0.53	1.19	1.72	2.07	9.30	4.48	3.11	2.94
REN52-5	4.7	4.5	25.58	12.79	38.37	0.21	0.94	1.15	0.82	7.35	3.00	3.48	3.40
REN52-6	7.1	8.2	25.58	12.79	38.37	0.60	1.35	1.95	2.35	10.56	5.08	2.90	2.65
REN52-7	<u>2.8</u>	<u>3.5</u>	<u>25.58</u>	<u>12.79</u>	<u>38.37</u>	<u>0.31</u>	<u>0.57</u>	<u>0.88</u>	<u>1.21</u>	<u>4.46</u>	<u>2.29</u>	<u>4.19</u>	<u>3.83</u>
Min.	2.8	3.5	25.58	12.79	38.37	0.21	0.57	0.88	0.82	4.46	2.29	2.90	2.65
Max.	7.5	8.3	25.58	12.79	38.37	0.88	1.45	2.33	3.44	11.34	6.07	4.19	3.83
Mean	5.4	6.0	25.58	12.79	38.37	0.50	1.04	1.54	1.94	8.14	4.01	3.39	3.15
Median	4.7	5.4	25.58	12.79	38.37	0.49	0.94	1.39	1.92	7.35	3.62	3.38	3.27
Stdev.	1.7	1.9	0.00	0.00	0.00	0.21	0.31	0.50	0.84	2.39	1.29	0.47	0.43
REN53-1	6.8	7.8	25.57	12.78	38.35	2.03	1.26	3.29	7.94	9.86	8.58	3.14	2.80
REN53-2	5.4	6.3	25.57	12.78	38.35	2.12	1.05	3.17	8.29	8.22	8.27	3.59	3.20
REN53-3	6.9	6.8	25.57	12.78	38.35	1.65	1.09	2.74	6.45	8.53	7.14	2.99	2.92
REN53-4	7.6	7.4	25.57	12.78	38.35	2.37	1.20	3.57	9.27	9.39	9.31	2.85	2.76
REN53-5	5.3	6.2	25.57	12.78	38.35	0.86	0.96	1.82	3.36	7.51	4.75	3.36	3.01
REN53-6	5.0	5.2	25.57	12.78	38.35	1.06	0.70	1.76	4.15	5.48	4.59	3.35	3.22
REN53-7	<u>6.9</u>	<u>7.8</u>	<u>25.57</u>	<u>12.78</u>	<u>38.35</u>	<u>2.59</u>	<u>1.19</u>	<u>3.78</u>	<u>10.13</u>	<u>9.31</u>	<u>9.86</u>	<u>3.03</u>	<u>2.74</u>
Min.	5.0	5.2	25.57	12.78	38.35	0.86	0.70	1.76	3.36	5.48	4.59	2.85	2.74
Max.	7.6	7.8	25.57	12.78	38.35	2.59	1.26	3.78	10.13	9.86	9.86	3.59	3.22
Mean	6.3	6.8	25.57	12.78	38.35	1.81	1.06	2.88	7.08	8.33	7.50	3.19	2.95
Median	6.8	6.8	25.57	12.78	38.35	2.03	1.09	3.17	7.94	8.53	8.27	3.14	2.92
Stdev.	1.0	1.0	0.00	0.00	0.00	0.65	0.19	0.81	2.55	1.49	2.11	0.26	0.20
REN54-1	9.6	9.2	26.01	13.00	39.01	4.26	1.94	6.20	16.38	14.92	15.89	2.68	2.67
REN54-2	12.0	11.8	26.01	13.00	39.01	3.82	2.10	5.92	14.69	16.15	15.18	2.31	2.29
REN54-3	13.2	13.9	26.01	13.00	39.01	3.08	2.59	5.67	11.84	19.92	14.53	2.22	2.08
REN54-4	11.4	12.6	26.01	13.00	39.01	6.63	2.17	8.80	25.49	16.69	22.56	2.41	2.27
REN54-5	10.6	11.9	26.01	13.00	39.01	4.26	2.02	6.28	16.38	15.54	16.10	2.56	2.35
REN54-6	16.0	16.4	26.01	13.00	39.01	6.35	3.21	9.56	24.41	24.69	24.51	2.13	2.03
REN54-7	<u>7.5</u>	<u>9.2</u>	<u>26.01</u>	<u>13.00</u>	<u>39.01</u>	<u>2.68</u>	<u>1.40</u>	<u>4.08</u>	<u>10.30</u>	<u>10.77</u>	<u>10.46</u>	<u>2.83</u>	<u>2.56</u>
Min.	7.5	9.2	26.01	13.00	39.01	2.68	1.40	4.08	10.30	10.77	10.46	2.13	2.03
Max.	16.0	16.4	26.01	13.00	39.01	6.63	3.21	9.56	25.49	24.69	24.51	2.83	2.67
Mean	11.5	12.1	26.01	13.00	39.01	4.44	2.20	6.64	17.07	16.96	17.03	2.45	2.32
Median	11.4	11.9	26.01	13.00	39.01	4.26	2.10	6.20	16.38	16.15	15.89	2.41	2.29
Stdev.	2.7	2.5	0.00	0.00	0.00	1.52	0.57	1.89	5.84	4.35	4.86	0.25	0.23

Site ID	HEMIPHOT	PAMAF	Above Canopy (mol/m ² /day)			Below Canopy (mol/m ² /day)			% Direct	% Diffuse	% Total	HEMIPHOT	PAMAF
	% Sky	% Sky	Direct	Diffuse	Total	Direct	Diffuse	Total				L _e	L _e
RGC62-1	5.1	6.2	25.56	12.78	38.34	1.33	1.02	2.35	5.20	7.98	6.13	3.37	3.07
RGC62-2	5.5	5.5	25.56	12.78	38.34	0.69	1.14	1.83	2.70	8.92	4.77	3.65	3.35
RGC62-3	5.1	5.9	25.56	12.78	38.34	0.96	1.02	1.98	3.76	7.98	5.16	3.48	3.15
RGC62-4	3.7	4.4	25.56	12.78	38.34	1.20	0.76	1.96	4.69	5.95	5.11	4.18	3.80
RGC62-5	5.3	6.0	25.56	12.78	38.34	0.77	1.06	1.83	3.01	8.29	4.77	3.42	3.08
RGC62-6	5.2	5.2	25.56	12.78	38.34	0.94	1.06	2.00	3.68	8.29	5.22	3.63	3.43
RGC62-7	<u>4.0</u>	<u>4.7</u>	<u>25.56</u>	<u>12.78</u>	<u>38.34</u>	<u>2.15</u>	<u>0.84</u>	<u>2.99</u>	<u>8.41</u>	<u>6.57</u>	<u>7.80</u>	<u>4.30</u>	<u>3.84</u>
Min.	3.7	4.4	25.56	12.78	38.34	0.69	0.76	1.83	2.70	5.95	4.77	3.37	3.07
Max.	5.5	6.2	25.56	12.78	38.34	2.15	1.14	2.99	8.41	8.92	7.80	4.30	3.84
Mean	4.8	5.4	25.56	12.78	38.34	1.15	0.99	2.13	4.49	7.71	5.57	3.72	3.39
Median	5.1	5.5	25.56	12.78	38.34	0.96	1.02	1.98	3.76	7.98	5.16	3.63	3.35
Stdev.	0.7	0.7	0.00	0.00	0.00	0.50	0.14	0.42	1.94	1.06	1.08	0.37	0.33
RGC63-1	7.1	8.0	25.42	12.71	38.13	3.18	1.39	4.57	12.51	10.94	11.99	3.06	2.78
RGC63-2	3.8	4.6	25.42	12.71	38.13	1.87	0.75	2.62	7.36	5.90	6.87	3.79	3.44
RGC63-3	7.6	9.1	25.42	12.71	38.13	2.37	1.38	3.75	9.32	10.86	9.83	2.81	2.52
RGC63-4	6.1	7.3	25.42	12.71	38.13	2.24	1.02	3.26	8.81	8.03	8.55	2.99	2.74
RGC63-5	5.4	6.4	25.42	12.71	38.13	1.44	1.11	2.55	5.66	8.73	6.69	3.69	3.25
RGC63-6	8.2	9.2	25.42	12.71	38.13	2.84	1.57	4.41	11.17	12.35	11.57	2.79	2.56
RGC63-7	<u>5.7</u>	<u>6.3</u>	<u>25.42</u>	<u>12.71</u>	<u>38.13</u>	<u>2.70</u>	<u>1.21</u>	<u>3.91</u>	<u>10.62</u>	<u>9.52</u>	<u>10.25</u>	<u>3.70</u>	<u>3.49</u>
Min.	3.8	4.6	25.42	12.71	38.13	1.44	0.75	2.55	5.66	5.90	6.69	2.79	2.52
Max.	8.2	9.2	25.42	12.71	38.13	3.18	1.57	4.57	12.51	12.35	11.99	3.79	3.49
Mean	6.3	7.3	25.42	12.71	38.13	2.38	1.20	3.58	9.35	9.48	9.39	3.26	2.97
Median	6.1	7.3	25.42	12.71	38.13	2.37	1.21	3.75	9.32	9.52	9.83	3.06	2.78
Stdev.	1.5	1.7	0.00	0.00	0.00	0.59	0.27	0.81	2.34	2.15	2.11	0.45	0.42
RGC64-1	5.6	6.0	25.42	12.71	38.13	1.18	0.99	2.17	4.64	7.79	5.69	3.11	3.02
RGC64-2	10.0	10.2	25.42	12.71	38.13	1.39	2.16	3.55	5.47	16.99	9.31	3.01	2.88
RGC64-3	7.2	7.7	25.42	12.71	38.13	1.18	1.36	2.54	4.64	10.70	6.66	2.96	2.79
RGC64-4	3.5	3.6	25.42	12.71	38.13	1.95	0.65	2.60	7.67	5.11	6.82	3.77	3.80
RGC64-5	3.5	3.8	25.42	12.71	38.13	0.28	0.44	0.72	1.10	3.46	1.89	3.77	3.67
RGC64-6	5.2	5.7	25.42	12.71	38.13	0.55	0.98	1.53	2.16	7.71	4.01	3.43	3.30
RGC64-7	<u>6.1</u>	<u>6.5</u>	<u>25.42</u>	<u>12.71</u>	<u>38.13</u>	<u>0.60</u>	<u>1.29</u>	<u>1.89</u>	<u>2.36</u>	<u>10.15</u>	<u>4.96</u>	<u>3.50</u>	<u>3.23</u>
Min.	3.5	3.6	25.42	12.71	38.13	0.28	0.44	0.72	1.10	3.46	1.89	2.96	2.79
Max.	10.0	10.2	25.42	12.71	38.13	1.95	2.16	3.55	7.67	16.99	9.31	3.77	3.80
Mean	5.9	6.2	25.42	12.71	38.13	1.02	1.12	2.14	4.01	8.85	5.62	3.36	3.24
Median	5.6	6.0	25.42	12.71	38.13	1.18	0.99	2.17	4.64	7.79	5.69	3.43	3.23
Stdev.	2.3	2.3	0.00	0.00	0.00	0.58	0.56	0.90	2.27	4.41	2.35	0.34	0.38

Site ID	HEMIPHOT	PAMAF	Above Canopy (mol/m ² /day)			Below Canopy (mol/m ² /day)						HEMIPHOT	PAMAF
	% Sky	% Sky	Direct	Diffuse	Total	Direct	Diffuse	Total	% Direct	% Diffuse	% Total	L _e	L _e
VWN12-1	9.7	11.1	26.02	13.01	39.03	3.63	1.85	5.48	13.95	14.22	14.04	2.60	2.37
VWN12-2	6.7	7.7	26.02	13.01	39.03	2.27	1.39	3.66	8.72	10.68	9.38	3.28	2.94
VWN12-3	7.0	6.6	26.02	13.01	39.03	3.26	1.48	4.74	12.53	11.38	12.14	3.38	3.29
VWN12-4	11.6	12.8	26.02	13.01	39.03	5.16	2.36	7.52	19.83	18.14	19.27	2.58	2.37
VWN12-5	10.6	10.2	26.02	13.01	39.03	4.27	2.09	6.36	16.41	16.06	16.30	2.59	2.53
VWN12-6	5.4	6.2	26.02	13.01	39.03	3.22	1.13	4.35	12.38	8.69	11.15	3.65	3.32
VWN12-7	<u>8.4</u>	<u>7.7</u>	<u>26.02</u>	<u>13.01</u>	<u>39.03</u>	<u>5.25</u>	<u>1.67</u>	<u>6.92</u>	<u>20.18</u>	<u>12.84</u>	<u>17.73</u>	<u>3.09</u>	<u>3.10</u>
Min.	5.4	6.2	26.02	13.01	39.03	2.27	1.13	3.66	8.72	8.69	9.38	2.58	2.37
Max.	11.6	12.8	26.02	13.01	39.03	5.25	2.36	7.52	20.18	18.14	19.27	3.65	3.32
Mean	8.5	8.9	26.02	13.01	39.03	3.87	1.71	5.58	14.86	13.14	14.29	3.02	2.85
Median	8.4	7.7	26.02	13.01	39.03	3.63	1.67	5.48	13.95	12.84	14.04	3.09	2.94
Stdev.	2.3	2.5	0.00	0.00	0.00	1.09	0.42	1.42	4.19	3.26	3.64	0.44	0.42
VWN13-1	4.9	4.6	25.80	12.90	38.70	1.53	0.93	2.46	5.93	7.21	6.36	3.35	3.33
VWN13-2	6.7	6.3	25.80	12.90	38.70	2.55	1.38	3.93	9.88	10.70	10.16	3.54	3.21
VWN13-3	7.7	8.4	25.80	12.90	38.70	3.66	1.45	5.11	14.19	11.24	13.20	2.74	2.57
VWN13-4	12.0	12.8	25.80	12.90	38.70	4.74	2.27	7.01	18.37	17.60	18.11	2.33	2.15
VWN13-5	6.0	6.5	25.80	12.90	38.70	2.15	1.23	3.38	8.33	9.53	8.73	3.42	3.16
VWN13-6	10.0	11.0	25.80	12.90	38.70	3.73	2.00	5.73	14.46	15.50	14.81	2.71	2.47
VWN13-7	<u>9.4</u>	<u>8.4</u>	<u>25.80</u>	<u>12.90</u>	<u>38.70</u>	<u>4.26</u>	<u>1.83</u>	<u>6.09</u>	<u>16.51</u>	<u>14.19</u>	<u>15.74</u>	<u>2.67</u>	<u>2.73</u>
Min.	4.9	4.6	25.80	12.90	38.70	1.53	0.93	2.46	5.93	7.21	6.36	2.33	2.15
Max.	12.0	12.8	25.80	12.90	38.70	4.74	2.27	7.01	18.37	17.60	18.11	3.54	3.33
Mean	8.1	8.3	25.80	12.90	38.70	3.23	1.58	4.82	12.52	12.28	12.44	2.97	2.80
Median	7.7	8.4	25.80	12.90	38.70	3.66	1.45	5.11	14.19	11.24	13.20	2.74	2.73
Stdev.	2.5	2.8	0.00	0.00	0.00	1.18	0.47	1.62	4.56	3.63	4.19	0.46	0.44
VWN15-1	13.9	14.7	26.29	13.14	39.43	3.23	2.66	5.89	12.29	20.24	14.94	2.11	1.97
VWN15-2	6.0	7.0	26.29	13.14	39.43	1.36	1.09	2.45	5.17	8.30	6.21	3.04	2.82
VWN15-3	11.4	12.9	26.29	13.14	39.43	3.69	2.24	5.93	14.04	17.05	15.04	2.42	2.20
VWN15-4	7.4	8.4	26.29	13.14	39.43	1.47	1.25	2.72	5.59	9.51	6.90	2.78	2.61
VWN15-5	7.4	8.5	26.29	13.14	39.43	3.30	1.44	4.74	12.55	10.96	12.02	2.91	2.67
VWN15-6	12.4	13.2	26.29	13.14	39.43	5.71	2.35	8.06	21.72	17.88	20.44	2.29	2.16
VWN15-7	<u>11.5</u>	<u>12.3</u>	<u>26.29</u>	<u>13.14</u>	<u>39.43</u>	<u>2.96</u>	<u>2.22</u>	<u>5.18</u>	<u>11.26</u>	<u>16.89</u>	<u>13.14</u>	<u>2.31</u>	<u>2.18</u>
Min.	6.0	7.0	26.29	13.14	39.43	1.36	1.09	2.45	5.17	8.30	6.21	2.11	1.97
Max.	13.9	14.7	26.29	13.14	39.43	5.71	2.66	8.06	21.72	20.24	20.44	3.04	2.82
Mean	10.0	11.0	26.29	13.14	39.43	3.10	1.89	5.00	11.80	14.41	12.67	2.55	2.37
Median	11.4	12.3	26.29	13.14	39.43	3.23	2.22	5.18	12.29	16.89	13.14	2.42	2.20
Stdev.	3.0	3.0	0.00	0.00	0.00	1.47	0.62	1.95	5.58	4.70	4.95	0.36	0.32

Site ID	HEMIPHOT	PAMAF	Above Canopy (mol/m ² /day)			Below Canopy (mol/m ² /day)			% Direct	% Diffuse	% Total	HEMIPHOT	PAMAF
	% Sky	% Sky	Direct	Diffuse	Total	Direct	Diffuse	Total				L _e	L _e
VWS02-1	1.3	2.0	25.96	12.98	38.94	0.22	0.25	0.47	0.85	1.93	1.21	4.87	4.31
VWS02-2	6.0	5.6	25.96	12.98	38.94	1.98	1.23	3.21	7.63	9.48	8.24	3.44	3.42
VWS02-3	3.7	4.6	25.96	12.98	38.94	3.39	0.71	4.10	13.06	5.47	10.53	3.78	3.45
VWS02-4	4.9	5.8	25.96	12.98	38.94	0.40	1.01	1.41	1.54	7.78	3.62	3.51	3.17
VWS02-5	5.6	5.4	25.96	12.98	38.94	0.40	1.19	1.59	1.54	9.17	4.08	3.79	3.74
VWS02-6	4.4	5.6	25.96	12.98	38.94	1.38	0.81	2.19	5.32	6.24	5.62	3.40	3.06
VWS02-7	<u>2.7</u>	<u>3.3</u>	<u>25.96</u>	<u>12.98</u>	<u>38.94</u>	<u>1.84</u>	<u>0.45</u>	<u>2.29</u>	<u>7.09</u>	<u>3.47</u>	<u>5.88</u>	<u>5.42</u>	<u>3.98</u>
Min.	1.3	2.0	25.96	12.98	38.94	0.22	0.25	0.47	0.85	1.93	1.21	3.40	3.06
Max.	6.0	5.8	25.96	12.98	38.94	3.39	1.23	4.10	13.06	9.48	10.53	5.42	4.31
Mean	4.1	4.6	25.96	12.98	38.94	1.37	0.81	2.18	5.29	6.22	5.60	4.03	3.59
Median	4.4	5.4	25.96	12.98	38.94	1.38	0.81	2.19	5.32	6.24	5.62	3.78	3.45
Stdev.	1.7	1.5	0.00	0.00	0.00	1.15	0.37	1.20	4.41	2.84	3.08	0.79	0.45
VWS05-1	7.6	8.6	25.82	12.91	38.73	4.12	1.47	5.59	15.96	11.39	14.43	2.93	2.69
VWS05-2	7.7	8.1	25.82	12.91	38.73	3.31	1.56	4.87	12.82	12.08	12.57	3.40	3.08
VWS05-3	7.7	8.5	25.82	12.91	38.73	2.07	1.47	3.54	8.02	11.39	9.14	2.76	2.58
VWS05-4	11.1	12.0	25.82	12.91	38.73	3.65	2.14	5.79	14.14	16.58	14.95	2.50	2.31
VWS05-5	5.9	6.6	25.82	12.91	38.73	2.97	1.21	4.18	11.50	9.37	10.79	3.39	3.12
VWS05-6	6.5	7.2	25.82	12.91	38.73	3.67	1.24	4.91	14.21	9.60	12.68	3.05	2.83
VWS05-7	<u>10.1</u>	<u>10.5</u>	<u>25.82</u>	<u>12.91</u>	<u>38.73</u>	<u>5.60</u>	<u>2.04</u>	<u>7.64</u>	<u>21.69</u>	<u>15.80</u>	<u>19.73</u>	<u>2.83</u>	<u>2.67</u>
Min.	5.9	6.6	25.82	12.91	38.73	2.07	1.21	3.54	8.02	9.37	9.14	2.50	2.31
Max.	11.1	12.0	25.82	12.91	38.73	5.60	2.14	7.64	21.69	16.58	19.73	3.40	3.12
Mean	8.1	8.8	25.82	12.91	38.73	3.63	1.59	5.22	14.05	12.32	13.47	2.98	2.75
Median	7.7	8.5	25.82	12.91	38.73	3.65	1.47	4.91	14.14	11.39	12.68	2.93	2.69
Stdev.	1.9	1.9	0.00	0.00	0.00	1.09	0.37	1.32	4.21	2.83	3.41	0.33	0.28
VWS06-1	13.5	13.7	26.16	13.08	39.24	3.39	2.85	6.24	12.96	21.79	15.90	2.70	2.49
VWS06-2	14.2	15.0	26.16	13.08	39.24	2.49	2.64	5.13	9.52	20.18	13.07	2.05	1.94
VWS06-3	6.8	7.5	26.16	13.08	39.24	3.03	1.34	4.37	11.58	10.24	11.14	3.08	2.86
VWS06-4	6.7	6.7	26.16	13.08	39.24	0.86	1.28	2.14	3.29	9.79	5.45	2.99	2.92
VWS06-5	11.6	12.2	26.16	13.08	39.24	1.26	2.24	3.50	4.82	17.13	8.92	2.32	2.18
VWS06-6	13.4	14.0	26.16	13.08	39.24	1.62	2.64	4.26	6.19	20.18	10.86	2.36	2.21
VWS06-7	<u>5.6</u>	<u>6.2</u>	<u>26.16</u>	<u>13.08</u>	<u>39.24</u>	<u>1.04</u>	<u>1.00</u>	<u>2.04</u>	<u>3.98</u>	<u>7.65</u>	<u>5.20</u>	<u>3.17</u>	<u>3.04</u>
Min.	5.6	6.2	26.16	13.08	39.24	0.86	1.00	2.04	3.29	7.65	5.20	2.05	1.94
Max.	14.2	15.0	26.16	13.08	39.24	3.39	2.85	6.24	12.96	21.79	15.90	3.17	3.04
Mean	10.3	10.8	26.16	13.08	39.24	1.96	2.00	3.95	7.48	15.28	10.08	2.67	2.52
Median	11.6	12.2	26.16	13.08	39.24	1.62	2.24	4.26	6.19	17.13	10.86	2.70	2.49
Stdev.	3.7	3.8	0.00	0.00	0.00	1.01	0.77	1.53	3.86	5.88	3.90	0.43	0.43